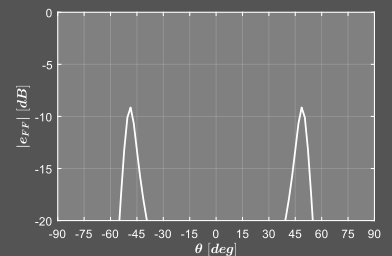
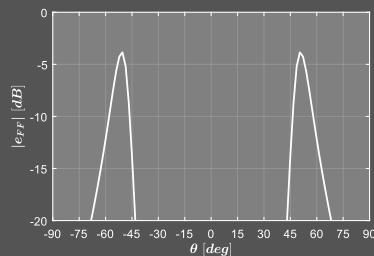
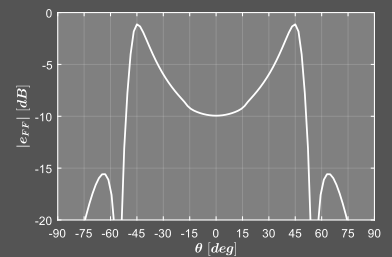
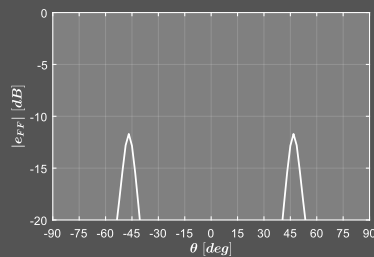
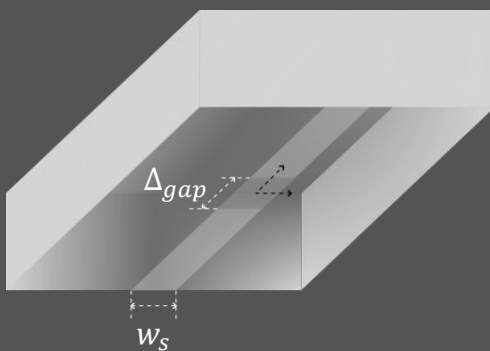
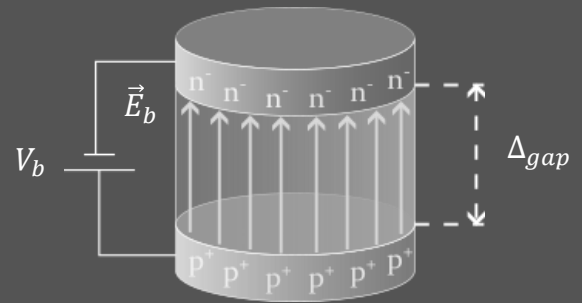
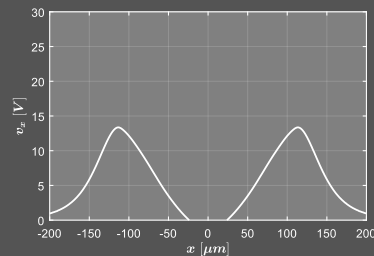
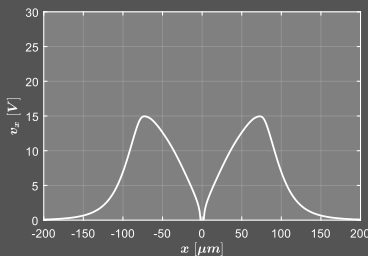
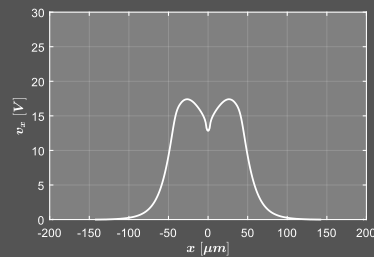
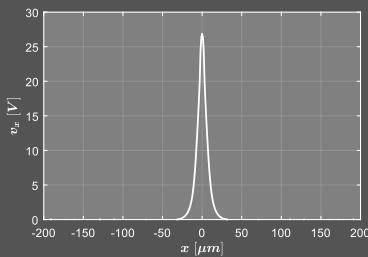


Analysis of the Photo-Conductive Infinite Slot Antenna and Photo-Conductive 1D Connected Array

Petar Peshev



Analysis of the Photo-Conductive Infinite Slot Antenna and Photo-Conductive 1D Connected Array

Petar Peshev

born in Sofia, Bulgaria

MASTER THESIS

for the purpose of obtaining the degree of Master of Science
at Delft University of Technology,
to be defended publicly on February 27-th, 2025 at 13.30 CET.

Project duration: October, 2023 – February, 2025

Thesis committee: Prof.dr. A. Neto, Delft University of Technology, supervisor
Prof.dr. Y. Aslan, Delft University of Technology

Faculty of Electrical Engineering, Mathematics, and Computer Science
Delft University of Technology
Delft, The Netherlands

Analysis of the Photo-Conductive Infinite Slot Antenna and Photo-Conductive iD Connected Array

An electronic version of this thesis is available at <http://repository.tudelft.nl/>.

Copyright © 2025 Petar V. Peshev

All rights reserved.



*To my family and friends,
because why not*

Preface

Terahertz technology has received continuously increasing attention in recent years. A key enabler of this technology is the photo-conductive antenna. A time-domain Norton equivalent circuit representing the antenna and a time-step algorithm provide the tools for analysis and design of such structures. However, the antenna impedance impulse response must be known beforehand. In this thesis, a more comprehensive characterization of the algorithm is provided through a detailed investigation. A numerical error in its output is discovered, the source of which identified, and an error minimization solution proposed. Using the newly acquired knowledge of the algorithm's properties, an infinite photo-conductive slot is analyzed. First, a time-domain energy balance equation is derived using switched capacitor formalism, and verified. Then, a comparison to constant antenna impedance approximation is performed. A study on the frequency and time-domain far-fields, as well as, on the influence of parameters is also performed. Finally, the analysis is extended to a 1D connected array, in which the mutual coupling and performance are investigated.

Acknowledgments

Hola,

It has been a year and 5 months; here I am - at the end of this long and ... painful journey. But, I wouldn't be at this point in my life without some people. So, without further ado ... prepare yourself ... for some unrefined thoughts that I will 100% overthink for the rest of my life ...

First and foremost, I would like to thank my mom and dad - Ralitzza and Valentin. I wouldn't be the person I am now without you. And, I think I turned out fine ... mostly (except the weird low self-esteem and god complex combination), I am what I am because of you (not sure how to say it tbh, but you understand me). Thank you for taking care of me all these years, paying for my education. Thank you for my existence (and I say this unironically, really).

Then, to the person I consider closest - my brother Asen. I am the oldest (maybe the smartest, debatable), but you are the wisest (pun intended). I can always ask you for a advice. Thank you for being there for me, listening to me, and giving advices. I understand why I am the oldest but the dynasty is named after you (ne bulgarite shte budat oburkani tuk, osobeno sled kato vidqt familiata mi).

To someone I've not know for long, but hope to get to know much better. I enjoy spending time with you. I hope we have a lot of adventures (but no pressure).

To all my friends, thank you for being friends with me. I was going to list names, but anonymity (people who read this don't have to find out that I am friendless, ... jokes on me nobody is reading it lol). ... Ah, I go distracted - I know my sense of humor is sometimes a little bit ... excessive. So, thank you for tolerating me, helping me, and spending time with me. I appreciate you.

I would also like to thank my supervisor - prof. dr. Andrea Neto. Thank you for helping me during the thesis, and all explanations. I learned a lot. Laurens your opinions were always interesting, thank you for the ideas.

If somebody mentions photo-conductive antennas after the 27th - I am going to lose it. I know what some of you are thinking - don't. ... I need a break.

Tbh, these are somewhat refined thoughts, ... I lied, but I started overthinking even before I started writing. And I guarantee that I will overthink every ... single ... letter in the next few months. ... My future children when you find this, make me overthink it again.

Now, buckle your seat belts ... people, because, in 79 (...) short pages I will learn you a thing or two about the analysis of the antenna type that I am not ... going ... to ... even ... mention.

Au revoir.

Petar Ralitzza-Valentinov Peshev out.

/mic drop/

Contents

Preface	i
Acknowledgments	iii
1 Introduction	1
1.1 Photo-Conductive Antennas	1
1.2 Time-Domain Norton Equivalent Circuit	2
1.2.1 Time Evolution of the Load Current	3
1.2.2 Fully Dispersive Approximation	5
1.3 Novelty of This Thesis	6
2 Time-Step Algorithm	7
2.1 Discrete-Time Fourier Transforms	7
2.1.1 Inverse Fourier Transform	8
2.2 Antenna Impedance	8
2.2.1 Feed Length	8
2.2.2 Slot Width	9
2.3 Algorithm	10
2.4 Weight Function	11
2.4.1 Feed Length Dependence	12
2.4.2 Slot Width Dependence	14
2.5 Error	14
2.5.1 Active Power Error	17
2.5.2 Radiated Energy Error	18
2.6 Error Analysis	18
2.6.1 Voltage	19
2.6.2 Active Power	19
2.6.3 Energy	19
2.6.4 Voltage and Current Effects	21
2.7 Convergence	21
2.8 Algorithm for Connected Arrays	22
2.8.1 Mutual Impedance	23
2.8.2 Mutual Placeholder Function	23
2.8.3 Energy Error	25
3 Infinite Leaky-Wave Slot	27
3.1 Energy Balance Equation	27
3.2 Comparison to the Fully Dispersive Approximation	29
3.3 Far-Field	30
3.3.1 Electric Vector Potential Approach	30
3.3.2 Spectral Convolution Approach	32

3.3.3	Magnetic Currents	32
3.3.4	Temporal Far-Field	33
3.3.5	Evaluation	33
3.4	Slot Wave	35
3.5	Power Spectral Density	35
3.5.1	Average Power	36
3.6	Energy	37
3.6.1	Saturation Point	37
3.6.2	Absorbed Optical Power	37
3.6.3	Bias Voltage	37
3.6.4	Full Width at Half Maximum	39
3.6.5	Recombination Time	39
3.7	Antenna Efficiency	40
3.7.1	Lower Frequency Limit	42
3.8	Bandwidth	43
4	iD Connected Array	45
4.1	Energy Balance Equation	45
4.1.1	Absorbed Optical Power	46
4.1.2	Bias Voltage	47
4.2	Mutual Coupling	47
4.2.1	Element Spacing	48
4.2.2	Excitation Delay	49
4.2.3	Cut-Off Frequency	49
4.2.4	Embedded Impedance	50
4.3	Magnetic Currents	52
4.3.1	Simultaneous Excitation	52
4.3.2	Progressive Excitation	52
4.4	Far-Field	55
4.4.1	Grating Lobes	55
4.4.2	Simultaneous Excitation	55
4.4.3	Progressive Excitation	55
4.5	Active Impedance	58
4.6	Power Spectral Density	58
5	Conclusion	61
5.1	Future Work	62
A	Discretized FT, IFT, & Convolution	65
A.1	Fourier Transform	65
A.2	Inverse Fourier Transform	66
A.3	Convolution	66
B	Derivations of Time-Step Algorithms	67
B.1	Fully Dispersive Time-Step Algorithm	68
B.2	Impedance Time-Step Algorithm	68
B.3	Admittance Time-Step Algorithm	69

Contents	vii
B.4 Weight Time-Step Algorithm	70
B.5 Weight Algorithm for Connected Array	70
C Study of Weight Functions	73
C.1 Inverse Frequency	73
C.2 Triangular	75
C.3 Inverse Exponential	77
C.4 Butterworth Filter Envelope	79
Bibliography	83

Chapter 1.

Introduction

In recent years, terahertz (THz) technology has received increasing attention. Possible applications include biomedical, spectroscopy, security screening, and next generation communications [1]–[6]. In fact, the global THz technology market size is estimated to be more than 450 million USD in 2022, and is expected to grow above 2.2 billion USD by 2030 [7]–[9]. Huge portion of the market is taken by imaging systems including security screening, followed by spectroscopy, while communication systems capture the smallest portion [7]. The high interest in security arises from the ability of THz waves to penetrate non-metallic materials, in addition to the potential of photo-conductive source to generate signals with wide bandwidth. Although the antenna segment of the market corresponded to only 77 million USD in revenues for 2022 [7], the antennas are integral part in the THz technology development. Specifically, the pulsed wave (PW) mode photo-conductive antenna (PCA) allowed the development of many THz applications. As an example, a PW mode photo-conductive connected array (PCCA) is proposed and evaluated in the design of a security imaging setup in [10].

Previously the main research focus was on increasing the radiated power by improving the photo-conductive materials. Although improving the photo-conductor is undoubtedly important, modeling the dispersion and improving the radiation efficiency was limited by the lack of mathematical tools. Needless to say, the dispersion and efficiency have a huge impact on the radiated field. Moreover, the lack of tools limited PCAs to already established (but inefficient) dipole antenna structures, such as the Auston switch. Fortunately, in recent years, more focus has shifted to the development of tools representing the PCA - equivalent circuits. These tools allow for the design of more dispersive and efficient structures.

1.1. Photo-Conductive Antennas

A photo-conductive source consists of metal terminals printed on the side of a photo-conductive material. The phenomena governing the operation of these structures can be split in two phases - carrier generation and carrier recombination.

First, a temporally Gaussian laser excites the photo-conductive material. Consequently, electrons are freed from the valence to conduction band. Naturally, this effect causes a rise in the material's conductivity. Further, because the terminals are biased by a DC source, an electric field is established across the photo-conductive gap. The conductivity and bias field cause current flow.

Second, after a certain point in time, no new carriers are generated due to the Gaussian nature of the laser. Meanwhile, the already generated electrons recombine to the valence band. This carrier recombination corresponds to decreasing current. Because the recombination time is in the order of sub-pico seconds, the time-domain current response is narrow. Consequently, frequencies up to the THz part of the spectrum are excited.

The concept is applied in antennas by patterning the metalized layer to form a radiating element. During this work, an infinite leaky-wave slot shown in Fig.1.1(a) is analyzed due to its high dispersivity and well known analytical expressions [11]–[13]. The slot is printed on a h_z thick ground plane and has a width w_s . The ground plane is at the interface between two semi-infinite homogeneous dielectrics with $\epsilon_{r,2} > \epsilon_{r,1}$. Optically pumping the photo-conductive feed with length Δ_{gap} as shown in Fig.1.1(b), results in an excitation (current) as shown in Fig.1.1(c). In turn, the excitation launches a wave on the slot, which leaks in the higher permittivity medium. In reality, the ground plane has a thickness. However, because

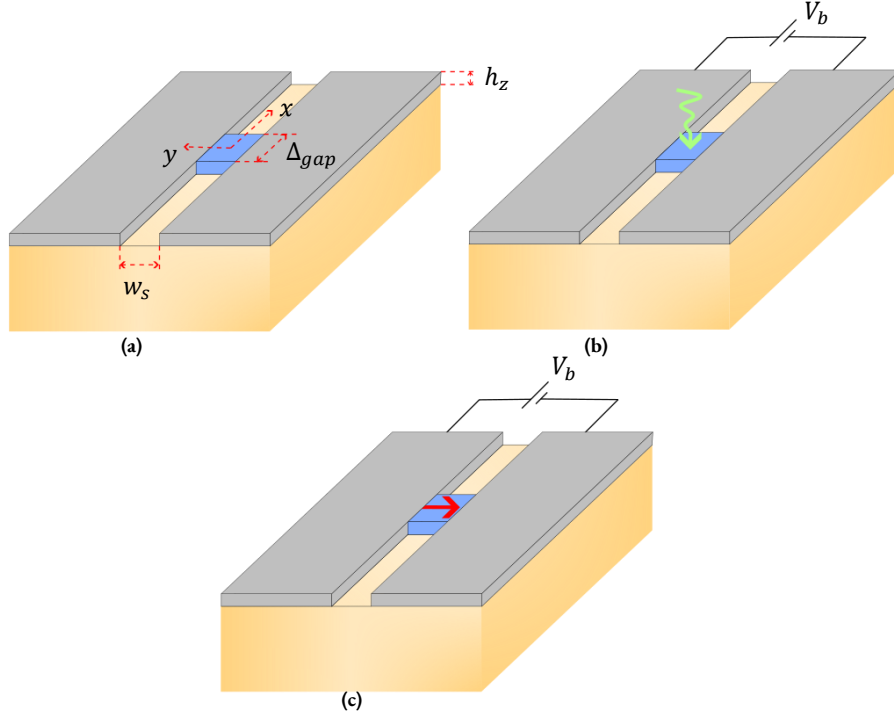


Figure 1.1: Photo-conductive infinite leaky-wave slot; in (a) geometry, in (b) optical pumping by pulsed temporally Gaussian laser, and in (c) electric current due to the optical pumping.

it is much smaller than the minimum wavelength, the ground plane is considered to be infinitesimally small (except in the time evolution of the current). In case the optical power is more than enough to saturate a single feed, multiple feeds in a connected array geometry can be used to improve the overall antenna efficiency.

1.2. Time-Domain Norton Equivalent Circuit

Equivalent time-domain circuits of PW mode PCA were proposed in the past [14][15]. These circuits model the charge screening effect, also known as carrier scattering, as an additional (to the bias source) time-varying voltage generator. Unfortunately, the additional generators often required a posteriori parameter calibration and made the circuits unsuitable to use. To overcome this issue, a frequency-domain Norton equivalent circuit is proposed in [16]–[18]. Unfortunately, the proposed circuit does not model well the physical phenomena over the whole spectrum. The problem stems from the non-linearity of the time-domain differential equations describing the PCA. Obviously, the non-linearity prevents the use of Laplace transform. Additionally, due to the non-linearities of the optical excitation, the use of methods such as harmonic balance is also impossible. Fortunately, a time-domain Norton equivalent circuit was proposed recently in [19], which proved to be an accurate PCA model. A short summary of the derivation procedure is provided for reference.

To derive the circuit, Maxwell's equations must be solved at the photo-conductor's boundary while complying to specific boundary conditions. Applying the equivalence principle separates the problem to an internal (to the feed's volume) and external parts. Thus, by coating the volume's surface with infinitesimally thin perfect electric conductor (PEC), the fields in the internal and external regions are described as radiated by equivalent magnetic currents at the two sides of the PEC. These internal and external magnetic currents equal to the cross product of the electric field at the interface and the respective normal vector (inside and outside the volume)

$$\vec{m}_{eq, \vec{r} \in V} = \vec{e} \times \hat{n}_{\vec{r} \in V}, \quad (1.1a)$$

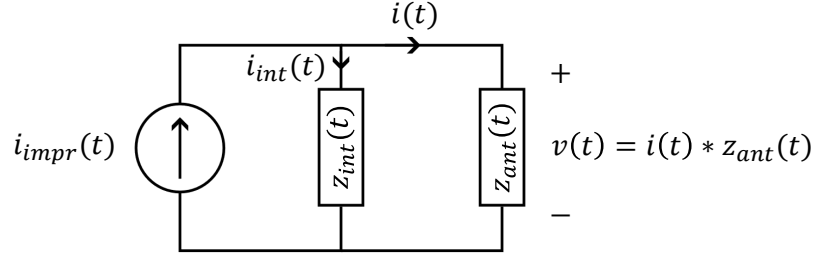


Figure 1.2: Norton equivalent circuit of a photo-conductive antenna.

$$\vec{m}_{eq, \vec{r} \notin V} = \vec{e} \times \hat{n}_{\vec{r} \notin V}. \quad (1.1b)$$

With this in mind, the total internal magnetic field is the superposition of the scattered (by the internal magnetic current) and the one due to the bias source (incident). On the other hand, the field in the external region is only scattered by the external currents. Needless to say, the tangential components of the internal and external magnetic fields must be continuous across the interface.

$$\vec{h}_{\vec{r} \in V, inc}^T(t, V_b) + \vec{h}_{\vec{r} \in V, s}^T(t, \vec{m}_{eq, \vec{r} \in V}) = \vec{h}_{\vec{r} \notin V, s}^T(t, \vec{m}_{eq, \vec{r} \notin V}). \quad (1.2)$$

Moreover, the magnetic currents are equal in magnitude (same electric field), but opposite in direction (the internal surface normal vector is opposite to the external)

$$-\vec{m}_{eq, \vec{r} \in V} = \vec{m}_{eq, \vec{r} \notin V} = \vec{m}_{eq}. \quad (1.3)$$

Consequently, the incident field's tangential component (at the boundary) can be expressed as sum of scattered fields' tangential components

$$\vec{h}_{\vec{r} \in V, inc}^T(t, V_b) = \vec{h}_{\vec{r} \in V, s}^T(t, \vec{m}_{eq}) + \vec{h}_{\vec{r} \notin V, s}^T(t, \vec{m}_{eq}). \quad (1.4)$$

Further, for a small volume in terms of the wavelength, the electric field is uniform (spatially independent) inside the volume. Thus, the electric field and by extension magnetic currents are proportional to the (also spatially independent) voltage. In addition, the tangential magnetic field relation can be expressed as electric current through the circulation integral (Ampere's law)

$$i_{impr}(t, V_b) = i_{int}(t, v) + i(t, v), \quad (1.5)$$

where the impressed current i_{impr} corresponds to the incident field, the internal current i_{int} to the internally scattered field, and load current i to the externally scattered. The derived time-domain Norton equivalent circuit is shown in Fig.1.2. Indeed, the voltage can also be expressed as the convolution of load current and antenna load's impulse response

$$v(t) = \int_{-\infty}^{\infty} i(t') z_{ant}(t - t') dt. \quad (1.6)$$

In essence, the equivalent circuit represents the EM effects at the photo-conductor's surface. By changing the PEC with perfect magnetic conductor (PMC), a Thévenin equivalent circuit can be derived.

1.2.1. Time Evolution of the Load Current

The Drude-Lorentz model is used to derive an integral equation describing the load current's time evolution in [20]. In short, the model relates the current density inside the photo-conductor to the time evolution of generated carriers,

photo-conductor's impulse response (carrier recombination), and carrier drift velocity. The number of generated charges and carrier recombination response provide the charge density due to carriers freed at time t''

$$n(t, t'') = A e^{-\frac{1}{2}(\frac{t''}{\sigma_t})^2} e^{-\frac{t-t''}{\tau_{rec}}}, \quad (1.7)$$

where τ_{rec} is the recombination time, σ_t the standard deviation of the laser's Gaussian temporal envelop, and

$$A = \frac{\tilde{P}_{opt}}{hf_c} \frac{T}{\sqrt{2\pi\sigma_t^2}} \frac{1}{\Delta_{gap} w_s h_z} \quad (1.8)$$

is the number of maximum released carriers per second inside the photo-conductor's volume. The term \tilde{P}_{opt} is the absorbed optical power in the material, while T the repetition rate of the laser. Further, the drift velocity (of charges generated at t'') is a convolution between their acceleration and scattering impulse response (caused by material impurities)

$$\vec{v}_e(t, t'') = \int_{t''}^t e^{-\frac{t-t'}{\tau_s}} \frac{q_e}{m_e} \vec{e}_{gap}(t') dt', \quad (1.9)$$

where τ_s is the scattering time, and $e_{gap}(t) = E_b - e(t)$ the magnitude of the electric field inside the photo-conductive gap. Therefore, the total current density is the sum of the effects of all previously generated charges

$$\vec{j}(t) = A \frac{q_e^2}{m_e'} \int_{-\infty}^t e^{-\frac{1}{2}(\frac{t''}{\sigma_t})^2} e^{-\frac{t-t''}{\tau_{rec}}} \int_{t''}^t e^{-\frac{t-t'}{\tau_s}} \vec{e}_{gap}(t') dt' dt''. \quad (1.10)$$

Needless to say, the current is the total current density through the photo-conductor's cross section, while the gap's voltage is related to the (uniformly distributed) gap electric field through the line integral

$$i(t) = A \frac{q_e^2}{m_e'} \frac{\Delta_{gap} h_z}{w_s} \int_{-\infty}^t e^{-\frac{1}{2}(\frac{t''}{\sigma_t})^2} e^{-\frac{t-t''}{\tau_{rec}}} \int_{t''}^t e^{-\frac{t-t'}{\tau_s}} v_{gap}(t') dt' dt''. \quad (1.11)$$

Essentially, the current's time evolution is defined by highly non-linear integral equation of two nested convolutions. In summary, a PCA is described by a system of two non-linear integral equations - the voltage expressed as the convolution between the current and antenna impedance impulse response, and time evolution of the current.

The non-linearities limit the solution to the time-domain. Therefore, a numerical method has to be used to evaluate the voltage and currents. By representing them as sums of rectangular basis functions with step size Δ_t

$$v(t) \simeq \sum_{n=-\infty}^{\infty} v_n \text{rect}_{\Delta_t}(t - t_n), \quad (1.12a)$$

$$i(t) \simeq \sum_{n=-\infty}^{\infty} i_n \text{rect}_{\Delta_t}(t - t_n), \quad (1.12b)$$

a time-step algorithm is derived. Obviously, the initial evaluation time must be chosen sufficiently early to ensure zero initial conditions.

The photo-conductor, laser, antenna geometry, and numerical method parameters used during the span of this work are as summarized in Table.I.I, unless otherwise specified.

Table 1.1: Photo-conductor, laser, antenna geometry, and numerical method parameters used during this work.

PHOTO-CONDUCTOR		
Bias Voltage	V_b	30 V
Recombination Time	τ_{rec}	300 fs
Scattering Time	τ_s	8.5 fs
Effective Carrier Mass	m'_e	0.067 m_e
LASER		
Absorbed Optical Power	\tilde{P}_{opt}	50 mW
Full Width at Half Maximum (FWHM)	τ_p	100 fs
Repetition Rate	T	12.5 ns
Wavelength	λ_c	780 nm
ANTENNA GEOMETRY		
Slot Width	w_s	10 μm
Feed Length (Delta-Gap)	Δ_{gap}	5 μm
Ground Plane Height	h_z	2 μm
Relative Permittivity of Lower Dielectric	$\epsilon_{r,1}$	1
Relative Permittivity of Upper Dielectric	$\epsilon_{r,2}$	11.7
Element Spacing (in arrays)	Δ_x	100 μm
NUMERICAL		
Time-Step	Δ_t	0.2 τ_s
Frequency-Step	Δ_f	2.5 GHz
Start Time	t_0	-3 σ_t

1.2.2. Fully Dispersive Approximation

Previously, the antenna was considered to be completely dispersive. In other words, the antenna impedance was constant and real over the whole spectrum. Consequently, the antenna impulse response is represented by a Dirac delta function

$$z_{ant}(t) = \mathcal{F}^{-1}\{R_{ant}\} = R_{ant}\delta(t). \quad (1.13)$$

This dispersive approximation greatly simplifies the time-step procedure, and hence the analysis of PCAs, by removing the convolution integral between the current and impedance impulse response

$$v(t) = R_{ant}i(t). \quad (1.14)$$

Consequently, the voltage and current update rules of this dispersive time-step algorithm are

$$v_n = \frac{e^{-\frac{\Delta_t}{\tau_{rec}}} e^{-\frac{\Delta_t}{\tau_s}} i_{n-1} + G_{pcm,(n)} V_b}{1/R_{ant} + G_{pcm,(n)}}, \quad (1.15a)$$

$$i_n = e^{-\frac{\Delta_t}{\tau_{rec}}} e^{-\frac{\Delta_t}{\tau_s}} i_{n-1} + (V_b - v_n) G_{pcm,(n)}, \quad (1.15b)$$

where G_{pcm} is the conductance of the photo-conductive material. However, even the most dispersive antenna structures are not completely dispersive. Therefore, a more general time-step algorithm is required, which captures the antenna's non-dispersive effects.

1.3. Novelty of This Thesis

Although a non-dispersive time-step algorithm is proposed in [21], its performance, advantages, and disadvantages are not investigated. This thesis aims to fill these gaps by performing a comprehensive study and characterization of the algorithm. In fact, during the span of this work, a numerical error in the evaluated voltage and current was identified. A comprehensive study on the cause followed, and an error minimization procedure was derived.

Further, the photo-conductive infinite leaky-wave slot was never analyzed using its actual (non-dispersive) impedance. By applying the optimized time-step algorithm, a complete study on this antenna structure is performed capturing its non-dispersive effects. The analysis spans an investigation on the far-fields, power spectral density, efficiency among others. A comparison to the dispersive approximation is done. Also, a novel time-domain energy balance equation is derived.

Finally, the dispersive time-step algorithm cannot estimate the interactions between feeds in connected arrays. Hence, such study was never performed previously. In this work, an analysis on the mutual coupling, far-fields, and active impedance of 1D PCCAs is carried out.

The scope of this thesis is the following:

- **Chapter 2:** provides a comprehensive study on the time-step algorithm. Starts with the derivation and limitation of an initial time-step algorithm using directly the impedance impulse response. Then, provides the derivation and discussion of an improved time-step algorithm, supplemented by an investigation of the evaluated voltage and current error. Follows with a proposed of error minimization procedure. Ends with expanding the algorithm to connected arrays and discussing its error.
- **Chapter 3:** provides an analysis on infinite leaky-wave slot. Starts with the derivation of a time-domain energy balance equation. Continues by providing comparison with the dispersive approximation. Follows by analyzing the far-field and power spectral density. Ends with investigation on the radiated energy, bandwidth, and antenna efficiency.
- **Chapter 4:** provides an analysis on the 1D connected array. Starts with expanding the energy balance equation to multiple feeds. Continues by investigating the mutual coupling. Follows by discussing the magnetic currents and far-fields. Ends with a discussion on the active admittance.

Chapter 2.

Time-Step Algorithm

To solve for the time-varying transient voltage and current across the photo-conductive gap, a time-step algorithm has to be derived. Although such procedure is proposed in [21], comprehensive study and characterization of the algorithm are not performed. Consequently, conducting the aforementioned study is highly relevant and useful in improving the reliability of non-dispersive PCA analysis techniques.

In time-domain, the voltage across the antenna element is the convolution between current and the antenna's impedance impulse response

$$v(t) = \int_{-\infty}^t i(t')z_{ant}(t-t')dt'. \quad (2.1)$$

By using this relation and the time evolution of the current from [20], the time-step algorithm is derived. Naturally, the antenna impedance impulse response z_{ant} must be known beforehand. Although a time-domain analysis of the leaky-wave (LW) infinite slot is proposed in [22] and [23], analytical derivations for the time response of its impedance are not available. Consequently, to determine z_{ant} , the impedance is evaluated in the frequency-domain using the spectral analysis discussed in [13], and subsequently transformed to time-domain using the inverse Fourier-transform (IFT).

The chapter opens with a discussion on the recovery of the antenna impedance impulse response. This discussion is followed by derivations of the original and an improved weight time-step algorithms. Then, a procedure for minimizing the numerical error in the improved algorithm is proposed and discussed. Finally, the study is extended to a time-step characterization in connected 1D arrays.

2.1. Discrete-Time Fourier Transforms

The frequency-domain response of a general function $x(t)$ discretized by rectangular basis functions is evaluated using the discrete-time Fourier-transform (DTFT)

$$X(f) = \Delta_t \sum_{n=-\infty}^{\infty} x_n e^{-j2\pi f t_n}, \quad (2.2)$$

where the frequency-domain response $X(f)$ is a continuous function and Δ_t is the time-step. Additionally, as a consequence of the Poisson summation, $X(f)$ is a periodic function with periodicity defined by the sampling rate $f_s = 1/\Delta_t$. However, due to the discrete computation environment, the frequency-domain response is also discretized by rectangular basis functions with a frequency-step Δ_f

$$X(f) \simeq \sum_{k=-\infty}^{\infty} X_k \text{rect}_{\Delta_f}(f - f_k). \quad (2.3)$$

For a signal of N samples, the valid frequency components are those containing integer number of cycles

$$f_k = \Delta_f k = \frac{f_s k}{N} = \frac{k}{N\Delta_t}, \quad (2.4)$$

where Δ_f is related to the simulation time-length $\Delta_f = 1/N\Delta_t$. Therefore, the DTFT with a discrete frequency-domain response is defined as

$$X_k = \Delta_t \sum_{n=0}^{N-1} x_n e^{-j2\pi f_k t_n}. \quad (2.5)$$

It must be noted that the requirement of integer number of cycles is a consequence of the periodicity enforced by the discrete computational environments and Poisson summation.

Although the derived DTFT is sufficient to evaluate the frequency-domain response, using the fast Fourier-transform (FFT) provides a significant computational advantage in terms of evaluation time. Therefore, it is useful to derive the DTFT in terms of the discrete Fourier-transform (DFT). To that end, the frequency-component definition in Eq.2.4 and property $t_n = t_0 + n\Delta_t$ (with t_0 being the simulation start time) are substituted in Eq.2.5

$$X_k = e^{-j2\pi f_k t_0} \Delta_t \text{DFT}\{x\}, \quad (2.6)$$

where the term $e^{j2\pi f_k t_0}$ accounts for the phase shift at non-zero start time $t_0 \neq 0$ s. Usually, in discrete systems, the output of the DFT must be divided by the number of samples to recover the signal's amplitude spectrum. However, in this case, the amplitude spectrum is directly recovered as a consequence of the time discretization of the continuous FT, and by extension the multiplication with the time-step Δ_t . More detailed derivations are included in Appendix.A.

2.1.1. Inverse Fourier Transform

The derivation of the discrete-frequency inverse Fourier-transform (DFIFT) is trivial and similar to the DTFT

$$x_n = \Delta_f \sum_{k=0}^{N-1} X_k e^{j2\pi f_k t_n}, \quad (2.7)$$

where the time-domain response is a discrete periodic function with periodicity $T = 1/\Delta_f$. The number of samples in both domains is equal. Furthermore, the DFIFT is represented in terms of the inverse DFT (IDFT) by substituting Eq.2.4 and property $t_n = t_0 + n\Delta_t$ in Eq.2.7

$$x_n = \frac{1}{\Delta_t} \text{IDFT}\{X_k e^{j2\pi f_k t_0}\}. \quad (2.8)$$

2.2. Antenna Impedance

The antenna impedance is evaluated using the spectral analysis established in [11] and [13]. This analysis depends on a narrow-slot approximation at which the minimum wavelength is much larger than the slot's width. In this case, an edge singular (quasi-TEM) mode is dominant represented by a zero-order Bessel function in the spectral domain [11]. However, as the wavelength shrinks, the contributions of other modes increase. Unfortunately, no models exist incorporating these modes. Modeling these higher modes requires the investigation of the transverse spatial currents and describing the total contribution as a sum of additional new basis functions in the spectral domain. Yet, performing such study is out of the scope of this work. Therefore, the current analysis is limited to the narrow-slot approximation.

2.2.1. Feed Length

The impedance is plotted in Fig.2.1(a-b) for different feed lengths Δ_{gap} and slot width $w_s = 10 \mu m$. The narrow-slot limit is considered at $\lambda_2 = w_s/0.35$, where λ_2 is the wavelength in the denser medium. In general, for the edge singular

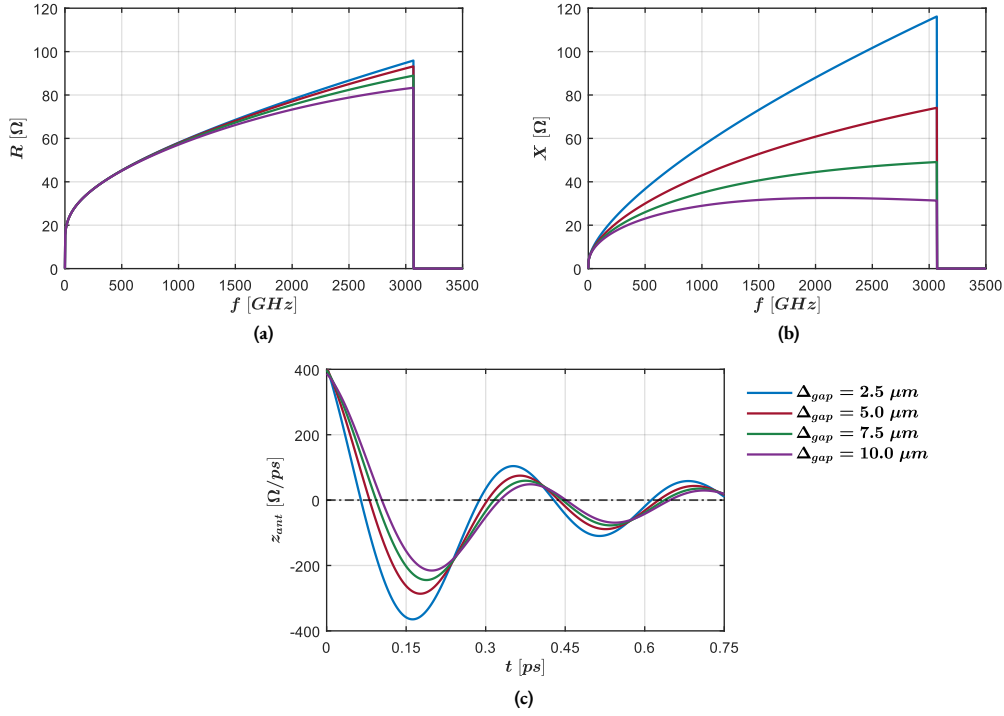


Figure 2.1: Antenna impedance of an infinite leaky-wave slot for different feed lengths Δ_{gap} and slot width $w_s = 10 \mu m$; in (a) the resistance R , (b) reactance X , and in (c) evaluated impulse response.

mode, the resistance and reactance increase faster with frequency for lower feed lengths. However, this effect is more evident in the reactance, while the increase in the resistance is negligible. Nevertheless, the growth in both components constitutes a growth in the impedance magnitude for decreasing feed lengths. Consequently, the discontinuity at the narrow-slot limit increases as the feed length decreases.

Using Eq.2.8, the impedance impulse response of the antenna is recovered and plotted in Fig.2.1(c). It must be noted that the impulse response is a real signal, i.e. the impedance is conjugate symmetric. The oscillations are due to the Gibbs phenomenon occurring at the narrow-slot limit discontinuity. For smaller feed lengths, the oscillation amplitude is larger corresponding to the larger discontinuity. Unfortunately, these oscillations are inherent consequences of the used numerical evaluation.

2.2.2. Slot Width

The impedance is plotted in Fig.2.2(a-b) for different slot widths w_s and feed length $\Delta_{gap} = 5 \mu m$. The narrow-slot limit is the same as before at $\lambda_2 = w_s/0.35$. Naturally, the narrow-slot limit frequency (referred to as maximum frequency f_{max}) is higher for smaller slot widths. It is evident that the discontinuity increases with the width. The corresponding impedance impulse response is plotted in Fig.2.2(c). Obviously, the oscillations are slower for higher f_{max} . Moreover, the careful observer notes that the discontinuity decreases for narrower slots, but the initial oscillation amplitude increases. Essentially, the Gibbs phenomenon is non-linear - dependent on the maximum frequency and discontinuity magnitude.

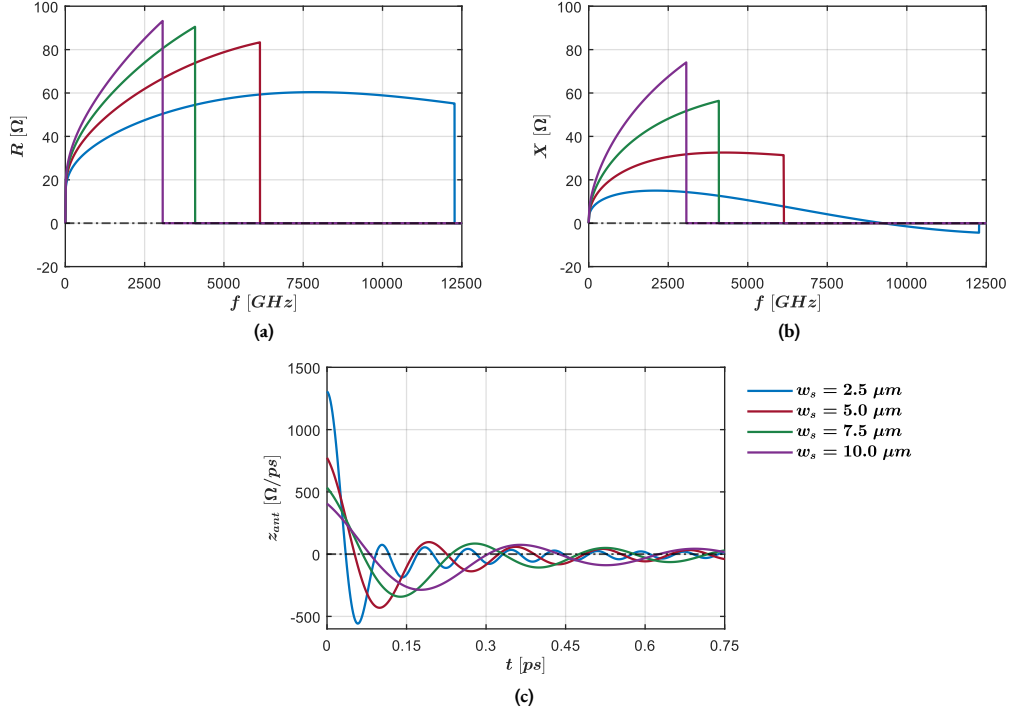


Figure 2.2: Antenna impedance of an infinite leaky-wave slot for different slot widths w_s and feed length $\Delta_{gap} = 5 \mu m$; in (a) the resistance R , (b) reactance X , and in (c) evaluated impulse response.

2.3. Algorithm

Mathematically, a PCA is described by a set of two integral equations - one describing the time-domain relation of voltage and current, and the other being the current's time evolution derived from the Drude-Lorentz model

$$v(t) = \int_{-\infty}^t i(t') z_{ant}(t-t') dt', \quad (2.9a)$$

$$i(t) = A \frac{q_e^2}{m_e} \frac{\Delta_{gap} w_z}{w_s} \int_{-\infty}^t e^{-\frac{1}{2} \left(\frac{t-t''-\tau_d}{\sigma_t} \right)^2} e^{-\frac{t-t''}{\tau_{rec}}} \int_{t''}^t (V_b - v(t')) e^{-\frac{t-t'}{\tau_s}} dt' dt''. \quad (2.9b)$$

Given the system's initial conditions (zero at sufficiently early time), the voltage and current can be evaluated using a time-step (also known as a marching-on) algorithm derived by time-discretizing these integral equations. This algorithm has update rules for the voltage and current defined as

$$v_n = \frac{e^{-\frac{\Delta_t}{\tau_{rec}}} e^{-\frac{\Delta_t}{\tau_s}} \Delta_t z_{ant,(0)} i_{n-1} + V_b \Delta_t^2 z_{ant,(0)} G_{pcm,(n)} + \Delta_t C_n}{1 + \Delta_t^2 z_{ant,(0)} G_{pcm,(n)}}, \quad (2.10a)$$

$$i_n = e^{-\frac{\Delta_t}{\tau_{rec}}} e^{-\frac{\Delta_t}{\tau_s}} i_{n-1} + (V_b - v_n) \Delta_t G_{pcm,(n)}, \quad (2.10b)$$

where G_{pcm} is the conductance of the photo-conductive material, and C_n describes the memory effects of the non-dispersive system at sample n . For a detailed derivation refer to Appendix.B.2.

Overall, the analysis of photo-conductive antennas consists of evaluating the antenna impedance and retrieving the impulse response. Then, by using the time-step algorithm and impulse response, the feed's time-domain excitation is

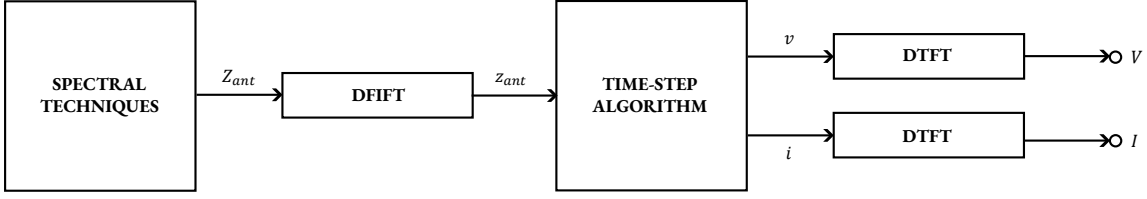


Figure 2.3: Block diagram of the photo-conductive antenna analysis.

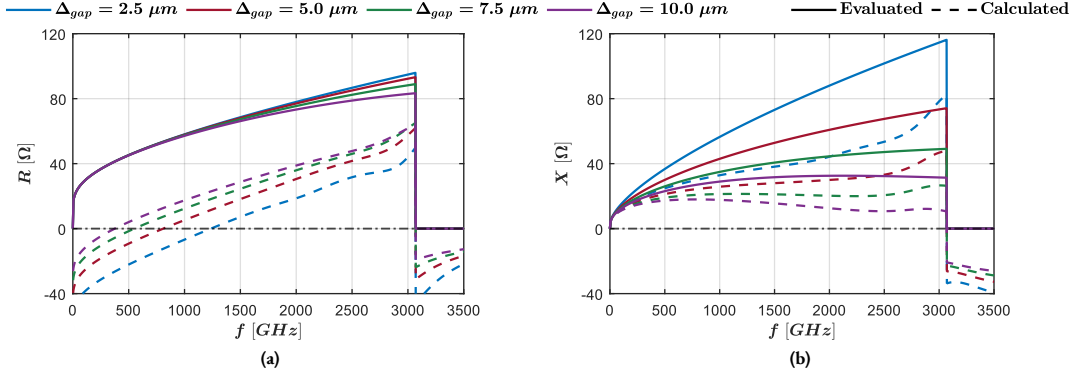


Figure 2.4: Comparison between the evaluated impedance using spectral techniques (solid lines) and calculated using the frequency-domain voltage and current (dashed lines) outputs of the time-step algorithm for different feed lengths Δ_{gap} and slot width $w_s = 10 \mu m$; in (a) the resistance R , and in (b) reactance X .

evaluated. Finally, the frequency-domain of the excitation is recovered for further analysis. A block diagram of the analysis procedure is shown in Fig.2.3.

To evaluate the performance of the time-step algorithm proposed in Eq.2.10, the calculated antenna impedance using the frequency-domain voltage and current is compared to the one evaluated using spectral techniques. The impedance is compared for different feed lengths and plotted in Fig.2.4. There is a large offset in the resistance between the calculated impedance from V/I and the actual evaluated using spectral techniques. This offset is around $R = 60 \Omega$ at $\Delta_{gap} = 2.5 \mu m$. Additionally, there is a mismatch in the reactance. The reactance deviation generally grows with frequency.

Furthermore, the impedance is compared for different slot widths in Fig.2.5. Again, a large offset is observed in the resistance and a mismatch in the reactance. This discrepancy between the evaluated and calculated impedance is related to the oscillations in the impulse response observed earlier. The results of this time-step algorithm are unreliable for further analysis. Therefore, an improved time-step algorithm is required, accounting for the large impedance discontinuity due to the narrow-slot approximation.

2.4. Weight Function

To reduce the discontinuity, the use of a weight function is proposed in [21]. The non-discretized time-domain voltage-current relation becomes

$$\int_{-\infty}^t v(t')w(t-t')dt' = \int_{-\infty}^t i(t')h(t-t')dt', \quad (2.11)$$

where w is the weight function, and $h = \mathcal{F}^{-1}\{H\} = \mathcal{F}^{-1}\{WZ_{ant}\}$ is a placeholder response resulting from the frequency-domain multiplication of the weight and antenna impedance. This weight time-step algorithm has updated

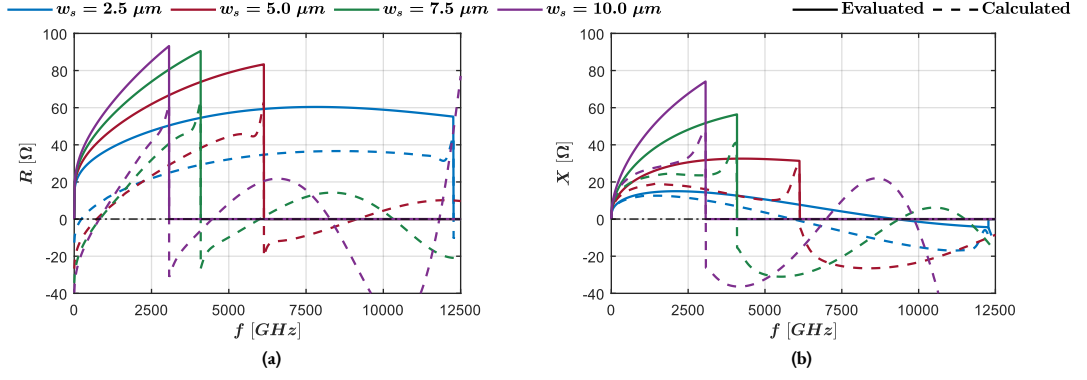


Figure 2.5: Comparison between the evaluated impedance using spectral techniques (solid lines) and calculated using the frequency-domain voltage and current (dashed lines) outputs of the time-step algorithm for different slot widths w_s and feed length $\Delta_{gap} = 5 \mu\text{m}$; in (a) the resistance R , and in (b) reactance X .

rules defined as

$$v_n = \frac{e^{-\frac{\Delta_t}{\tau_{rec}}} e^{-\frac{\Delta_t}{\tau_s}} h_0 i_{n-1} + V_b \Delta_t h_0 G_{pcm,(n)} + C_n}{w_0 + \Delta_t h_0 G_{pcm,(n)}}, \quad (2.12a)$$

$$i_n = e^{-\frac{\Delta_t}{\tau_{rec}}} e^{-\frac{\Delta_t}{\tau_s}} i_{n-1} + (V_b - v_n) \Delta_t G_{pcm,(n)}. \quad (2.12b)$$

The careful reader notes that the current's update rule does not change, as it is directly derived from the Drude-Lorentz model. A detailed derivation is provided in Appendix.B.4.

Undoubtedly, the weight function must be chosen such that it decreases with frequency in order to minimize the discontinuity. The choice of weight should be based on the performance of the overall voltage and current evaluation results. With this in mind, a brief examination of different weight options is described in Appendix.C, yet, the best choice is found to be the weight function used in [21] - the squared antenna admittance $W = Y_{ant}^2$. As a result, the placeholder function becomes the antenna admittance $H = Y_{ant}^2 Z_{ant} = Y_{ant}$, and it is referred as such for the rest of this work.

2.4.1. Feed Length Dependence

The weight function is plotted in Fig.2.6(a-b) for different feed lengths. The magnitude of the weight exhibits the desired behavior - decreasing with frequency. Additionally, as the impedance increases for smaller feeds, naturally the weight decreases. Contrary to the no-weight algorithm, it is expected that smaller Δ_{gap} results in better impedance match between the spectral techniques evaluation and V/I calculation - lower discontinuity. Moreover, the weight approaches infinity at DC corresponding to the zero impedance. In essence, this effect means there is no voltage drop across the feed at DC, constituting no expected change in the DC bias field. However, the effect also poses a difficulty in the evaluation of the IFT - improper integration over an infinite interval. Consequently, to solve this problem, the weight is truncated at DC in order to allow the numerical evaluation of the weight impulse response, i.e. the weight is set to zero $W(f = DC) = 0 \text{ S}^2$. This solution does not impact the overall analysis as the DC component is of no interest. The weight impulse response is plotted in Fig.2.6(c). The peak and oscillation amplitude are larger for bigger feeds, due to the larger weight magnitudes and discontinuities respectively. Nevertheless, the oscillation amplitude is decreased compared to the impedance impulse response in Fig.2.1(c).

The antenna admittance (placeholder function) is plotted in Fig.2.7(a-b). The magnitude decreases with the frequency and feed length. This decrease translates to smaller discontinuities. Moreover, the DC component is once again truncated to allow the numerical evaluation of the IFT. The recovered admittance impulse response is plotted in Fig.2.7(c). As seen, the oscillation amplitude is reduced due to the smaller discontinuity.

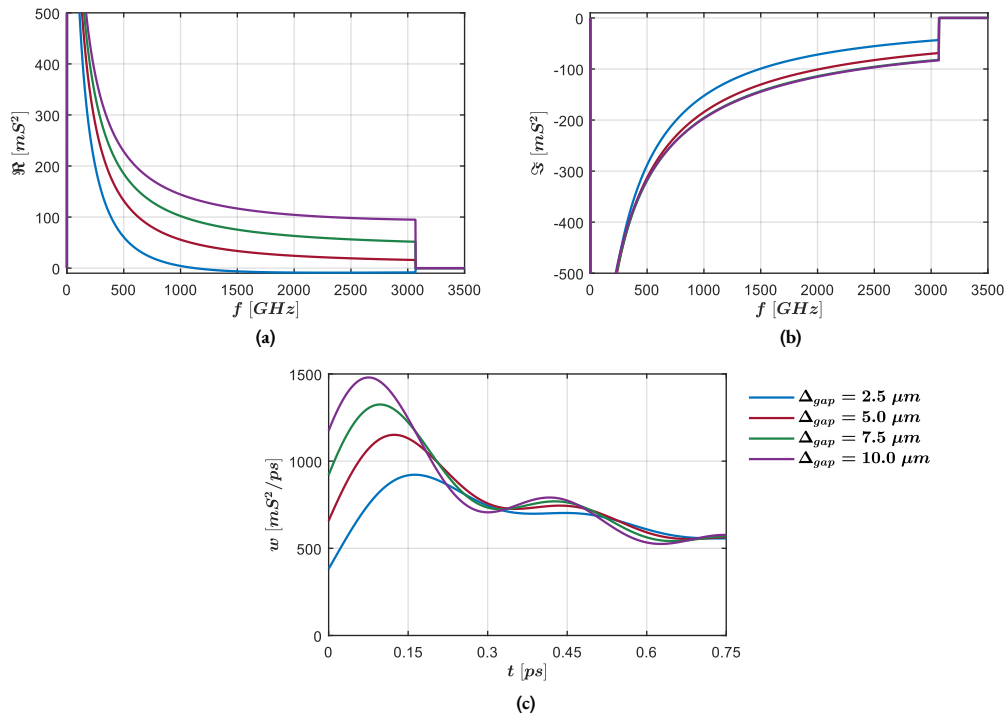


Figure 2.6: Weight function (squared antenna admittance) for different feed lengths Δ_{gap} and slot width $w_s = 10 \mu m$; in (a) the real part, (b) imaginary part, and in (c) impulse response.

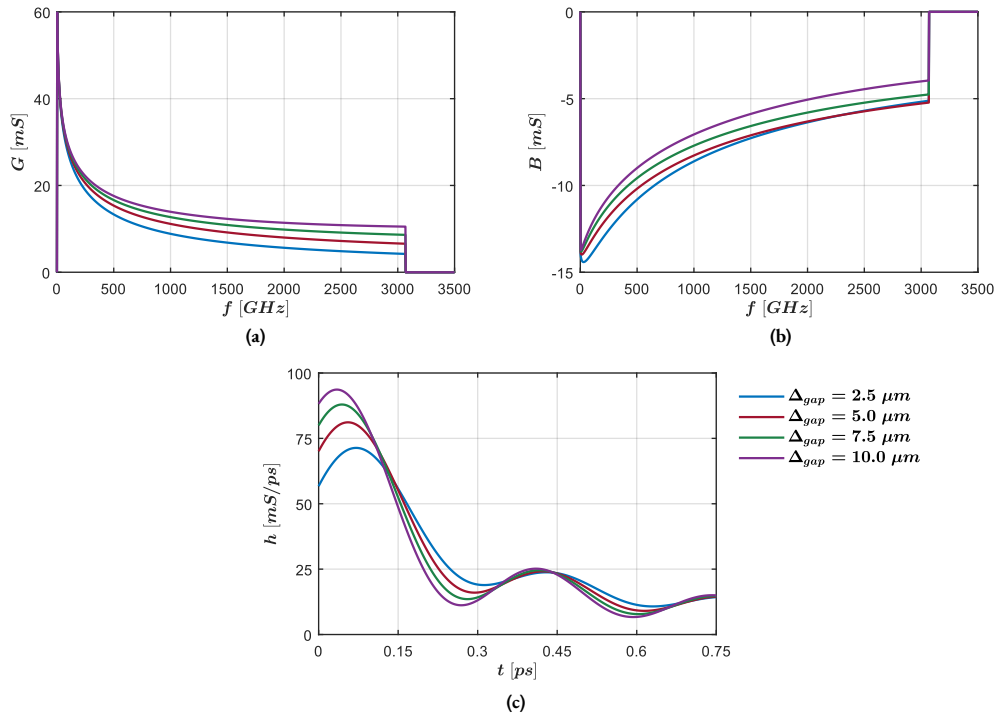


Figure 2.7: Antenna admittance (placeholder function) for different feed lengths Δ_{gap} and slot width $w_s = 10 \mu m$; in (a) the conductance G , (b) susceptance B , and in (c) impulse response.

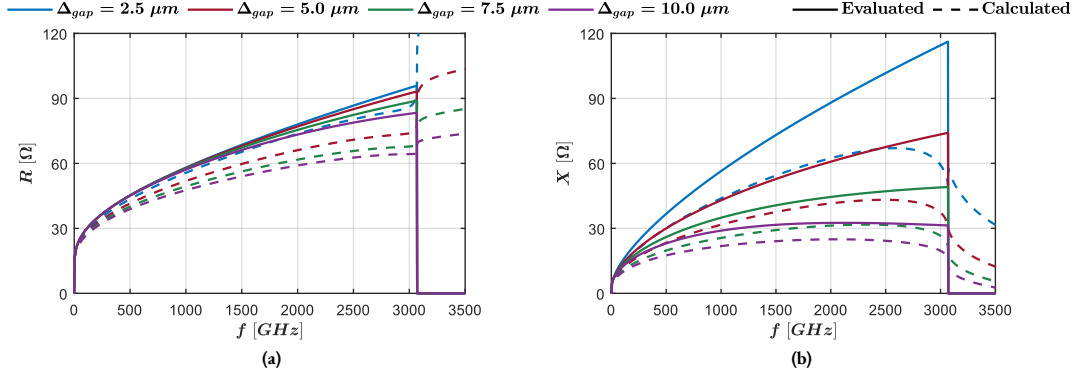


Figure 2.8: Comparison between the evaluated impedance using spectral techniques (solid lines) and calculated from V/I (dashed lines) for different feed lengths Δ_{gap} and slot width $w_s = 10 \mu m$; in (a) the resistance R , and in (b) reactance X .

To evaluate the performance of the weight algorithm in Eq.2.12, the impedance calculated from V/I is compared to the evaluation using spectral techniques. The comparison is plotted in Fig.2.8. The weight time-step algorithm offers a significant improvement. Although the match is not ideal, the resistance does not exhibit the large offset observed in the no-weight algorithm. Furthermore, the match improves for smaller feeds - lower discontinuities. Nonetheless, the mismatch increases with frequency. On the other hand, the reactance shows an improvement, but not as significant as the resistance. These improvements confirm the oscillations as the root cause of the algorithm's numerical error.

2.4.2. Slot Width Dependence

The weight is plotted in Fig.2.9(a-b) for different slot widths. In contrast to the smaller impedance at f_{max} for narrower slots, the weight function increases resulting in larger discontinuity. This effect is especially noticeable for small widths. Consequently, the weight function does not satisfy the desired behavior. The weight impulse response is plotted in Fig.2.9(c). Referring to the larger discontinuities for narrower slots, the oscillation amplitude increases. Additionally, the oscillation period decreases due to the higher maximum frequency. The antenna admittance is plotted in Fig.2.10(a-b). Naturally, the admittance grows similarly to the weight. The impulse response is plotted in Fig.2.10(c). Faster and larger oscillations are observed due to larger discontinuity and maximum frequency.

A comparison between the evaluated and calculated impedance is plotted in Fig.2.11. Compared to the no-weight algorithm results, there is a significant improvement. At this point, it must be noted that typically PCAs are manufactured with slot width $w_s = 10 \mu m$ and feed length $\Delta_{gap} = 5 \mu m$ [24][25]. For these parameters, the weight algorithm performs well for a coarse analysis. However, the remaining error must be minimized when a more accurate analysis is required.

2.5. Error

As seen, the error is a discrepancy between the evaluated impedance using spectral techniques and the one calculated from the algorithm's outputs. Thus, it is logical to investigate the error in terms of the difference between the two. However, in connected 1D arrays, the active impedance is not known beforehand. Consequently, the error is investigated in terms of the difference between the directly evaluated frequency-domain voltage $V_1 = \mathcal{F}\{v\}$, and the one estimated using the evaluated current spectral techniques impedance $V_2 = \mathcal{F}\{i\}Z_{ant}$. To quantify the voltage error, the magnitude and phase difference of V_2 and V_1 are normalized to the respective maximums of V_1

$$E_{|V|} = \frac{|V_2| - |V_1|}{\max\{|V_1|\}}, \quad (2.13a)$$

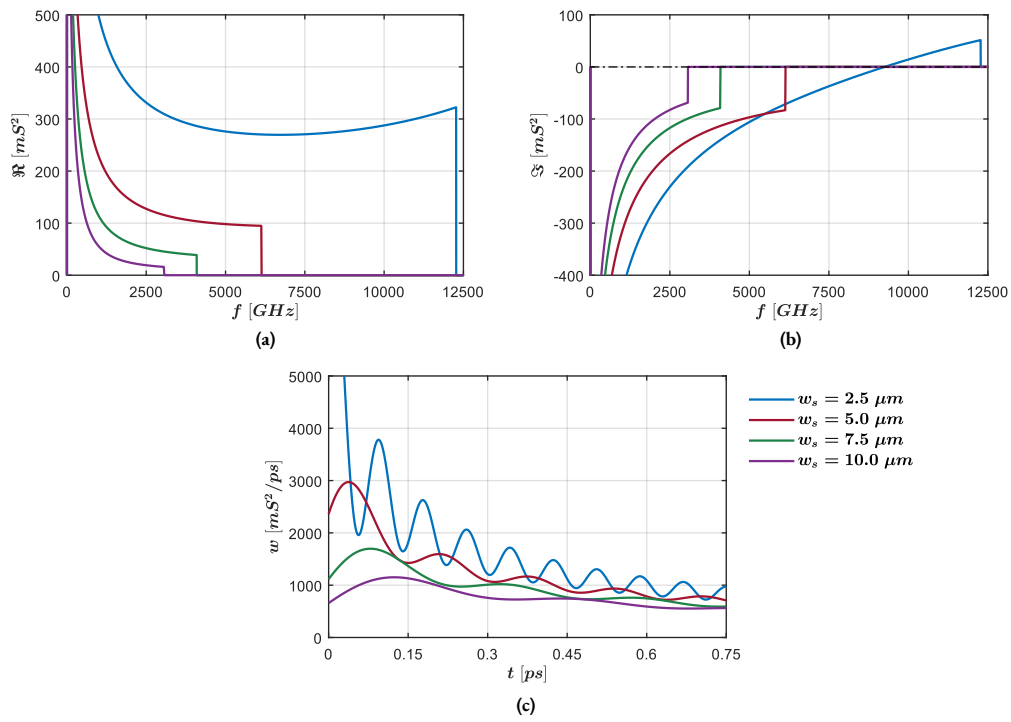


Figure 2.9: Weight function for different slot widths w_s and feed length $\Delta_{gap} = 5 \mu m$; in (a) the real part, (b) imaginary part, and in (c) impulse response.

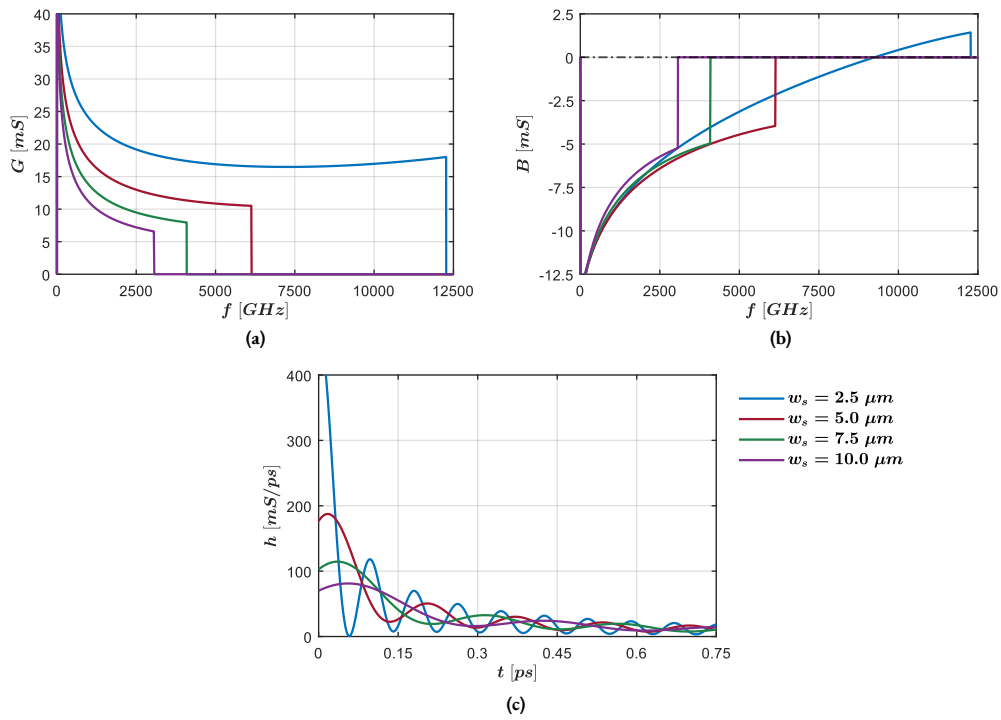


Figure 2.10: Antenna admittance for different slot widths w_s and feed length $\Delta_{gap} = 5 \mu m$; in (a) the conductance G , (b) susceptance B , and in (c) impulse response.

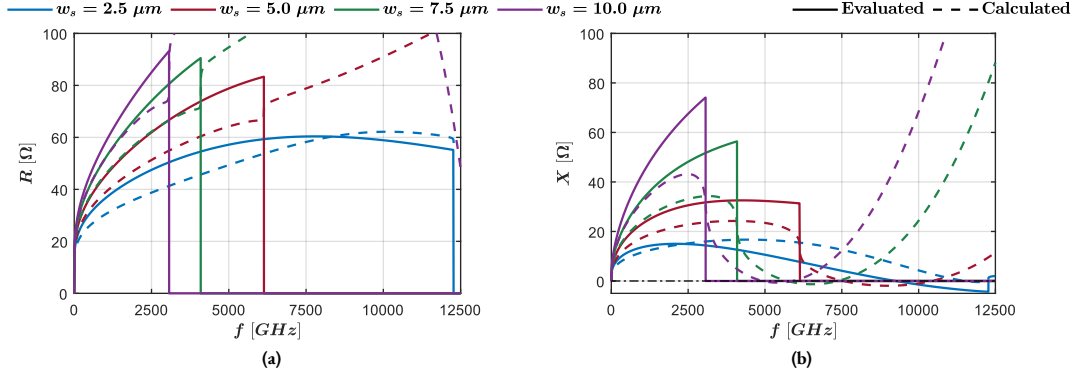


Figure 2.11: Comparison between the evaluated impedance using spectral techniques (solid lines) and calculated from V/I (dashed lines) for different slot widths w_s and feed length $\Delta_{gap} = 5 \mu m$; in (a) the resistance R , and in (b) reactance X .

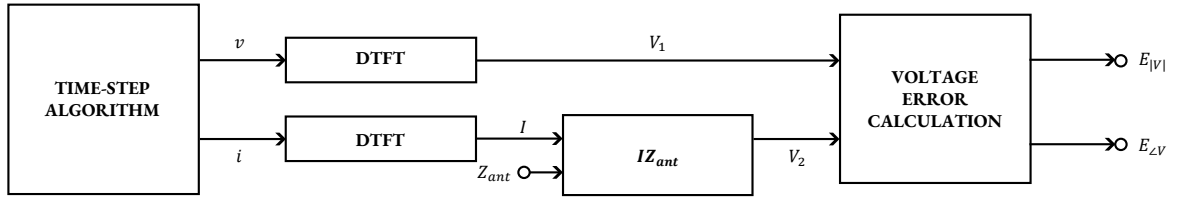


Figure 2.12: Block diagram of the algorithm's voltage error analysis.

$$E_{\angle V} = \frac{\angle V_2 - \angle V_1}{\max\{|\angle V_1|\}}. \quad (2.13b)$$

A block diagram of the error analysis is shown in Fig.2.12.

The V_1 and V_2 voltages are compared in Fig.2.13 for slot width $w_s = 10 \mu m$ and feed length $\Delta_{gap} = 5 \mu m$. The magnitude difference is large. Additionally, it increases with the frequency power, at the component with highest power $|V_2| - |V_1| \simeq 1.5 \text{ mV/GHz}$. On the other hand, the phase difference starts at $\angle V_2 - \angle V_1 \simeq 2 \text{ deg}$ and increases, in general, linearly with frequency (reaching $\simeq 12 \text{ deg}$ at the narrow-slot limit). It must be noted that the truncation at the narrow-slot limit (maximum frequency) in V_2 appears due to the impedance's truncation. While V_1 , as $\mathcal{F}^{-1}\{v\}$, is not truncated because these frequencies are *present* in the time-domain signal.

The absolute voltage error is plotted in Fig.2.14. The plot confirms the previous observations - magnitude error is largest at frequencies with higher power, and phase error increases linearly with frequency. The magnitude error reaches a

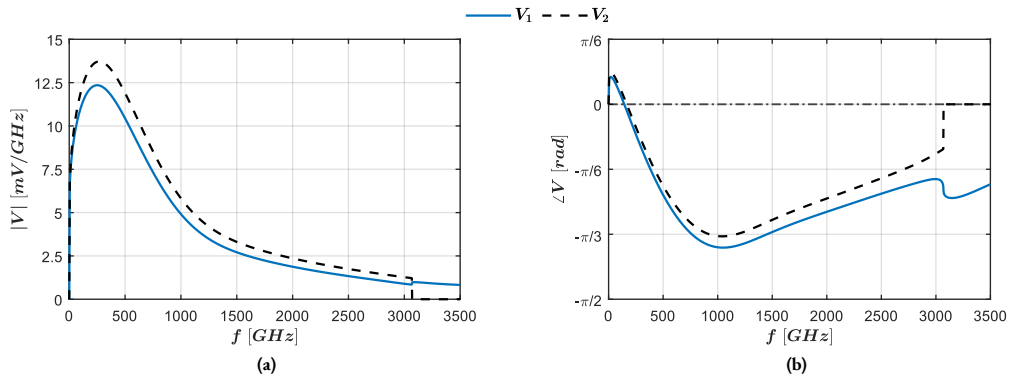


Figure 2.13: Frequency-domain voltage comparison between $V_1 = \mathcal{F}\{v\}$ and $V_2 = \mathcal{F}\{i\}Z_{ant}$, for slot width $w_s = 10 \mu m$ and feed length $\Delta_{gap} = 5 \mu m$; in (a) the magnitude $|V|$, and in (b) phase $\angle V$.

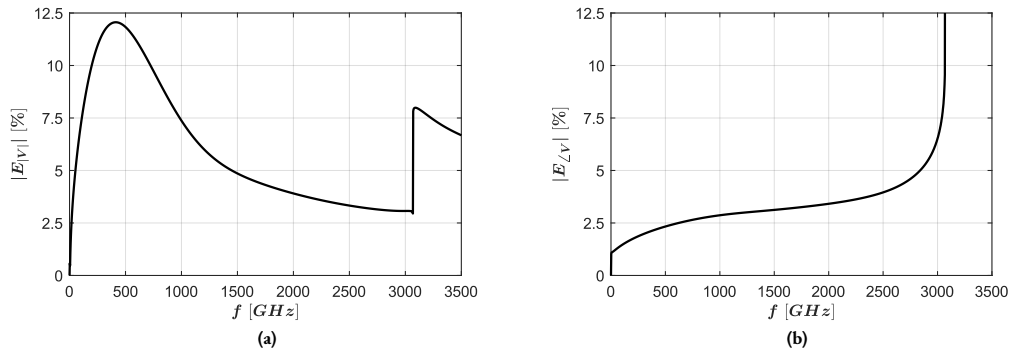


Figure 2.14: Voltage error for slot width $w_s = 10 \mu m$ and feed length $\Delta_{gap} = 5 \mu m$; in (a) the magnitude error $E_{|V|}$, and in (b) phase error $E_{\angle V}$.

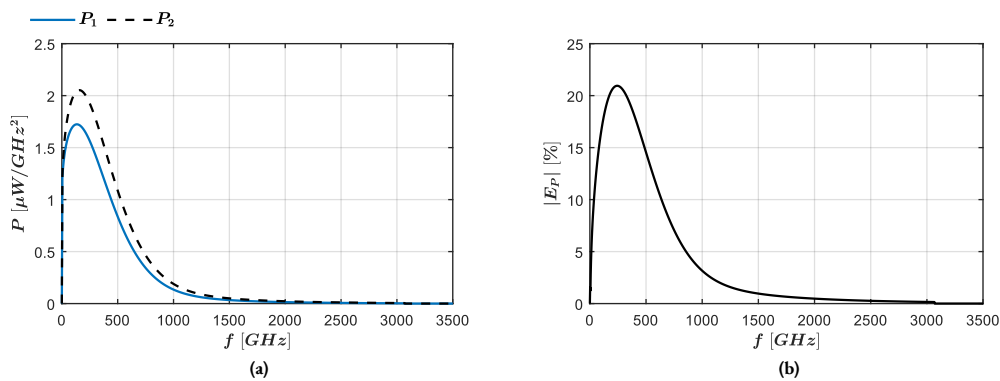


Figure 2.15: In (a) active power spectral density comparison between voltage and current estimations, and in (b) active power error, for slot width $w_s = 10 \mu m$ and feed length $\Delta_{gap} = 5 \mu m$.

maximum of $|E_{|V|}| = 12\%$, and becomes $|E_{|V|}| = 3\%$ at f_{max} . This deviation is significant for an accurate analysis.

2.5.1. Active Power Error

The discrepancy between the v and i time-step algorithm outputs is more noticeable in the power spectral density (PSD), due to the square law. Thus, it is useful to investigate the error in terms of active power. The power is evaluated using the two outputs separately - the voltage with admittance, and current with impedance

$$P_1 = \frac{1}{2} |V_1|^2 \Re\{Y_{ant}\}, \quad (2.14a)$$

$$P_2 = \frac{1}{2} |I|^2 \Re\{Z_{ant}\}. \quad (2.14b)$$

To quantify the PSD error, the difference between P_2 and P_1 is normalized to the maximum of P_1

$$E_P = \frac{P_2 - P_1}{\max\{P_1\}}. \quad (2.15)$$

A block diagram of the power error analysis is shown in Fig.2.16.

The P_1 and P_2 evaluations are compared in Fig.2.15(a), and absolute power error is plotted in Fig.2.15(b). Obviously, identically to the voltage error, the difference between P_1 and P_2 is higher at the frequencies with more power. The error reaches a maximum of $P_2 - P_1 \simeq 0.3 \mu W/GHz^2$; in terms of the defined power error, it corresponds to $E_P \simeq 20\%$ -

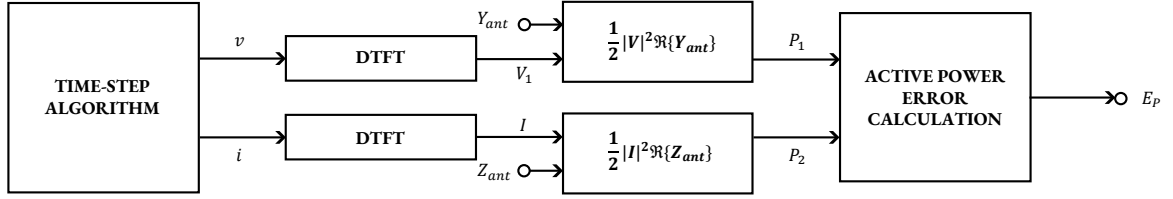


Figure 2.16: Block diagram of the active power error analysis.

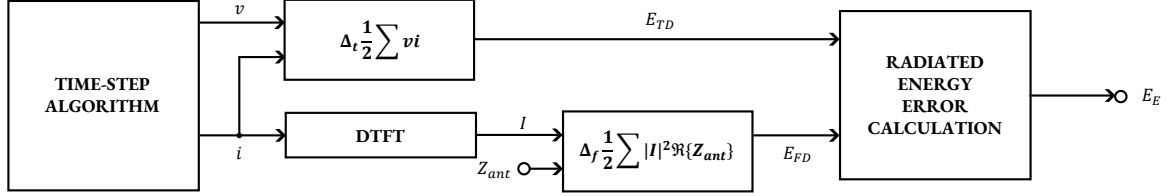


Figure 2.17: Block diagram of the energy error analysis.

a significant deviation for an accurate analysis. Although not plotted, it must be noted that the error increases for larger feed lengths, due to larger discontinuity.

2.5.2. Radiated Energy Error

From Parseval's theorem, the energy is equal in the time and frequency domains. Estimating the radiated energy directly in the time-domain provides a quick evaluation method without frequency-domain conversions. Consequently, investigating the deviation between the time-domain and frequency-domain energy is useful for providing error optimization guidelines. The time-domain energy is calculated by integrating the instantaneous power¹, and in the frequency-domain by integrating

$$E_{TD} = \Delta_t \frac{1}{2} \sum_n v_n i_n, \quad (2.16a)$$

$$E_{FD} = \Delta_f \frac{1}{2} \sum_k |I|^2 \Re\{Z_{ant}\}. \quad (2.16b)$$

To quantify the energy error, the difference between E_{TD} and E_{FD} is normalized to E_{FD}

$$E_E = \frac{E_{TD} - E_{FD}}{E_{FD}}. \quad (2.17)$$

A block diagram of the energy error analysis is shown in Fig.2.17.

2.6. Error Analysis

As mentioned in Section.2.4.1, the weight and admittance contain singularities at DC, i.e. $W(f = DC) \rightarrow \infty$ and $Y_{ant}(f = DC) \rightarrow \infty$. These singularities are associated with the cause of the observed error. In fact, decreasing the frequency step (hence the first non-DC component moves closer to DC) reflects as an increase in the impulse responses. This increase is especially noticeable in the time-domain weight. It is a consequence of including components with larger magnitudes, and increases the IFT's numerical evaluation error.

To solve this issue, the weight and admittance are additionally truncated between DC and a minimum frequency f_{min} .

¹A detailed derivation of the time-domain energy is provided in Chapter 3

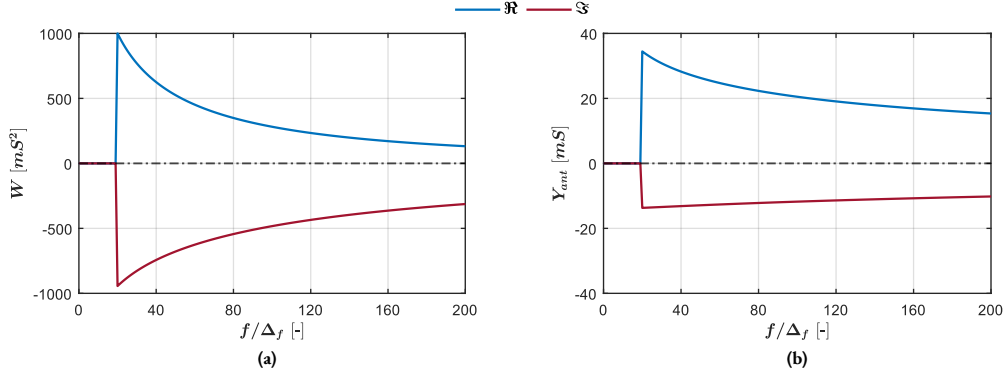


Figure 2.18: In (a) additionally truncated weight function, and in (b) additionally truncated antenna admittance, for slot width $w_s = 10 \mu m$, feed length $\Delta_{gap} = 5 \mu m$, minimum frequency $f_{min} = 20\Delta_f$, and frequency-step $\Delta_f = 2.5 GHz$.

This additional truncation adds a second slower oscillation to the impulse responses. However, the new oscillation has no significant influence on the overall algorithm performance due to two factors. First, the period of oscillation is much larger than the recombination time - low f_{min} . Second, the new Gibbs oscillation has small amplitude, again as a consequence of the low f_{min} . Although this solution does not improve or even causes a slight error increase in $DC \leq f < f_{min}$, these frequencies are relatively small and of no-interest in the analysis of PCAs. To visualize the additional truncation, the weight and admittance are plotted in Fig.2.18 for minimum frequency $f_{min} = 20\Delta_f$ with frequency step $\Delta_f = 2.5 GHz$.

2.6.1. Voltage

The voltage error is plotted in Fig.2.19(a-b) for different minimum frequencies. The magnitude error in the non-truncated spectrum decreases as the minimum frequency increases. Although, an increase is observed in the truncated spectrum. Consequently, f_{min} must be chosen with care to not affect frequencies of interest. On the other hand, the phase error is not dependent on the minimum frequency. To confirm the solution's effectiveness, the error's mean in the non-truncated spectrum is plotted in Fig.2.19(c). Clearly, the error decreases with f_{min} validating the proposed solution.

2.6.2. Active Power

The absolute power error is plotted in Fig.2.20(a) for different minimum frequencies. At small f_{min} , the error is especially noticeable. However, it significantly decreases for higher minimum frequencies. While, similarly to the voltage error, it increases in the truncated spectrum. Furthermore, the error's mean in the non-truncated spectrum is plotted in Fig.2.20(b). The results conform to the previous observations - the error decreases with f_{min} .

2.6.3. Energy

The energy error is plotted in Fig.2.21 with respect to the minimum frequency. In contrast to the voltage and power observations, the energy error decreases up to a certain f_{min} . Afterwards, the error starts to increase. In essence, excessively increasing f_{min} removes huge portion of the spectral contents, which overcompensates for the numerical error and introduces a *negative* discrepancy. This discrepancy constitutes a significant change in the impulse responses. Therefore, the minimum frequency must be chosen such as to minimize the error while not significantly altering the time-domain responses.

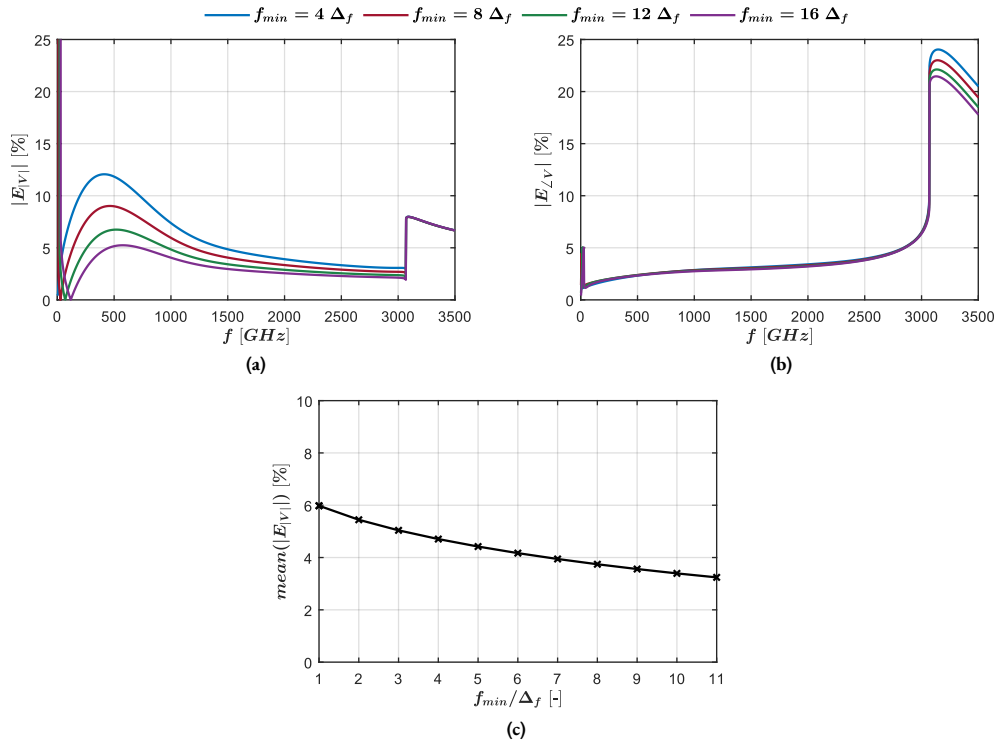


Figure 2.19: Voltage error for different truncations; in (a) the magnitude error $E_{|V|}$, (b) phase error $E_{\angle V}$, and in (c) the mean non-truncated spectrum magnitude error with respect to f_{min} .

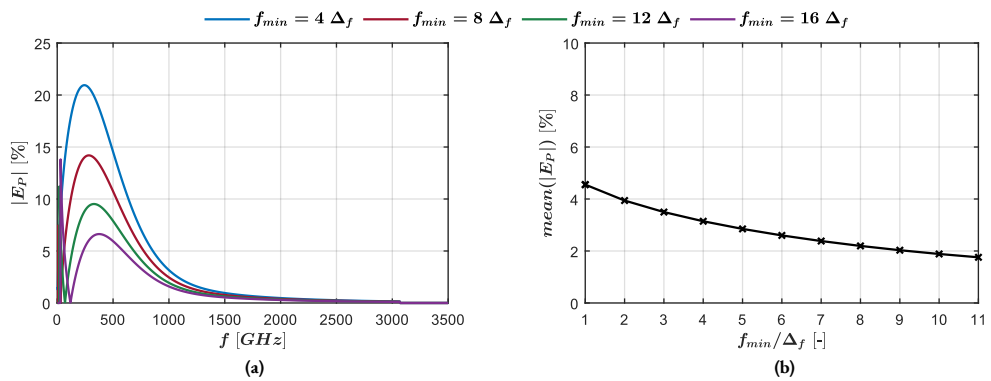


Figure 2.20: In (a) active power error for different truncations, and in (b) mean power error in the non-truncated spectrum.

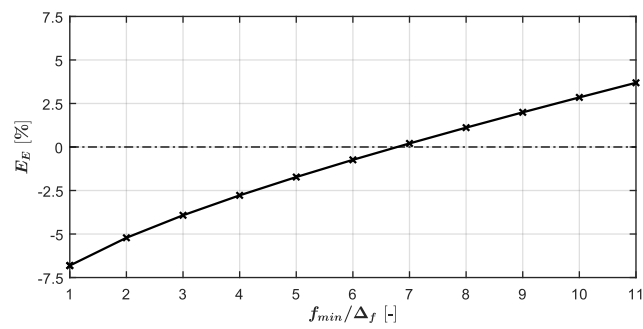


Figure 2.21: Energy error with respect to the truncation.

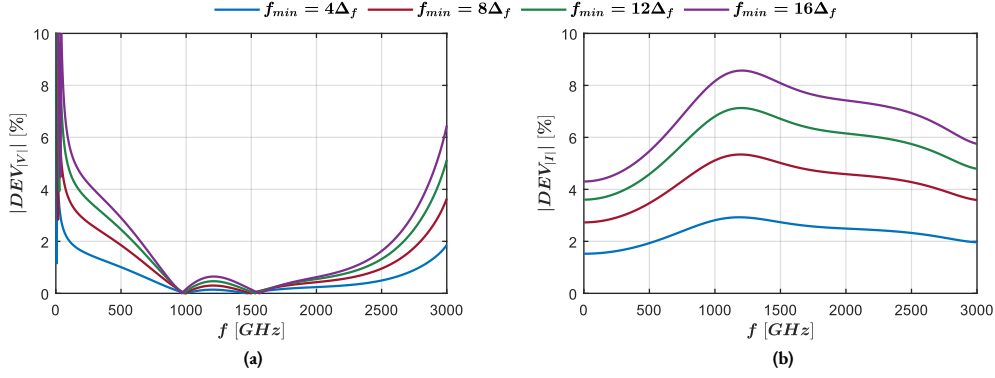


Figure 2.22: Frequency-domain magnitude deviation between the algorithm's outputs with additional weight function truncation and without truncation; in (a) the voltage deviation, and in (b) current deviation.

2.6.4. Voltage and Current Effects

Not unexpectedly, adding the non-physical truncation (between DC and f_{min}) alters the voltage and current. Thus, to provide a complete characterization of the proposed solution, the truncation effects on the algorithm's outputs are investigated with respect to the non-truncated evaluations. The effects on the voltage and current are quantified by normalizing the frequency-domain magnitude difference

$$DEV_{|V|} = \frac{|V| - |V_{ref}|}{|V_{ref}|}, \quad (2.18a)$$

$$DEV_{|I|} = \frac{|I| - |I_{ref}|}{|I_{ref}|}, \quad (2.18b)$$

where $V = \mathcal{F}\{v\}$ and I are the outputs evaluated with the weight truncation, and V_{ref} and I_{ref} are without truncation.

The voltage and current deviations are plotted in Fig.2.22 for different minimum frequencies. Generally, the current changes with a constant ratio across the spectrum; naturally, larger weight truncation increases the deviation. On the other hand, the voltage changes in a non-constant manner - the error in the truncated spectrum increases, while the effects are minor in the middle part of the non-truncated spectrum.

2.7. Convergence

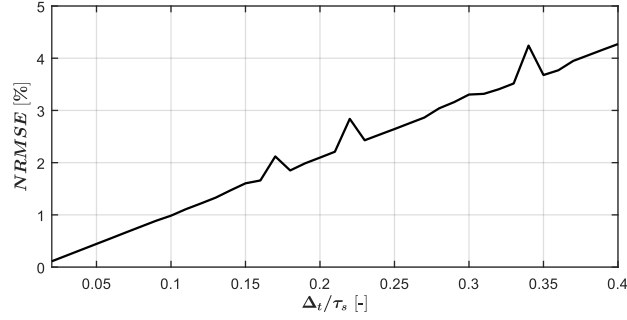
To ensure result convergence, the time-step must be sufficiently smaller than shortest time parameter, i.e. the scattering time. However, reducing the time-step results in increased computational time. Therefore, it is useful to investigate the convergence, deviation in the algorithm's output from the actual signal, with respect to the time-step.

In order to characterize the convergence, a simulation is performed with sufficiently small time-step in terms of the scattering time. The evaluated current is selected as a reference signal. Afterwards, the time-step is increased, and the newly evaluated current is compared to the reference. Because the reference signal has a smaller time-step, it must be down-sampled to the *investigated* signal. Additionally, only the samples in an interval containing mostly the non-zero antenna response are considered. The deviation between the reference and investigated signals is quantified in terms of the normalized root mean square error (NRMSE)

$$\text{NRMSE} = \frac{1}{\max\{i_{ref}\} - \min\{i_{ref}\}} \sqrt{\frac{1}{n_{max}} \sum_{n=0}^{n_{max}-1} (i_n - i_{ref,(n)})^2}, \quad (2.19)$$

Table 2.1: Time samples of several time-steps in terms of the scattering time and with start time at $t = 0$ s.

i_{ref}	Δ_t	Time Samples						
		$t_0 = 0$	$t_1 = 0.01\tau_s$	$t_2 = 0.02\tau_s$	$t_3 = 0.03\tau_s$	$t_4 = 0.04\tau_s$	\dots	$t_{n_{max}}$
	$0.01\tau_s$	$t_0 = 0$	$t_1 = 0.01\tau_s$	$t_2 = 0.02\tau_s$	$t_3 = 0.03\tau_s$	$t_4 = 0.04\tau_s$	\dots	$t_{n_{max}}$
	$0.02\tau_s$	$t_0 = 0$		$t_1 = 0.02\tau_s$		$t_2 = 0.04\tau_s$	\dots	$t_{n_{max}}$
	$0.03\tau_s$	$t_0 = 0$			$t_1 = 0.03\tau_s$		\dots	$t_{n_{max}}$

**Figure 2.23:** Normalized root mean square error (convergence) evaluated in a time interval of $t_{n_{max}} = 3$ ps and for reference signal with $\Delta_t = 0.01\tau_s$.

where n_{max} is the sample index corresponding to the maximum considered time instance, i the investigated signal, and i_{ref} the reference. To demonstrate the need for down-conversion, the time samples for several time-steps are shown in Table.2.1 with start time chosen at zero for simplicity.

The NRMSE is plotted in Fig.2.1 evaluated in a time interval $t_{n_{max}} = 3$ ps and for reference at $\Delta_t = 0.01\tau_s$. Evidently, the error increases linearly with the time-step. Usually, the time-step is chosen as $\Delta_t = 0.2\tau_s$ resulting in 2% error.

2.8. Algorithm for Connected Arrays

In connected arrays, the wave component launched by a feed interacts with the other feeds, i.e. the feeds are coupled. This interaction is described through the mutual impedance. Therefore, the voltage at feed q is dependent on the currents of all Q feeds

$$\begin{bmatrix} V_1 \\ \vdots \\ V_Q \end{bmatrix} = \begin{bmatrix} Z_{11} & \dots & Z_{1Q} \\ \vdots & \ddots & \vdots \\ Z_{Q1} & \dots & Z_{QQ} \end{bmatrix} \begin{bmatrix} I_1 \\ \vdots \\ I_Q \end{bmatrix}, \quad (2.20)$$

where $Z_{qq} = Z_s$ is the self-impedance, and Z_{qp} the mutual impedance of elements q and p . The mutual impedance describes the voltage component at element q due to the current at p . While the self-impedance is equal to the antenna impedance Z_{ant} previously discussed, i.e. it describes the effects at the longitudinal point of the current. Moreover, the impedance matrix \mathbf{Z} is a $Q \times Q$ Toeplitz. Naturally, not multiplying by a weight causes the same abnormal behavior

observed in the single feed algorithm. Consequently, multiplying both sides of the matrix equation with the same weight

$$\begin{bmatrix} W & \dots & 0 \\ \vdots & \ddots & \vdots \\ 0 & \dots & W \end{bmatrix} \begin{bmatrix} V_1 \\ \vdots \\ V_Q \end{bmatrix} = \begin{bmatrix} H_{11} & \dots & H_{1Q} \\ \vdots & \ddots & \vdots \\ H_{Q1} & \dots & H_{QQ} \end{bmatrix} \begin{bmatrix} I_1 \\ \vdots \\ I_Q \end{bmatrix}, \quad (2.21)$$

where the weight matrix is $\mathbf{W} = W\mathbf{I}$, and $H_{qp} = WZ_{qp}$ is the placeholder function of elements q and p . Similarly to the impedance matrix, the placeholder matrix \mathbf{H} is a $Q \times Q$ Toeplitz. Obviously, the time-domain voltage-current relation at feed q is defined by the sum of convolutions

$$\int_{-\infty}^t v_q(t')w(t-t')dt' = \sum_{p=1}^Q \int_{-\infty}^t i_p(t')h_{qp}(t-t')dt', \quad (2.22)$$

where $h_{qp} = \mathcal{F}^{-1}\{H_{qp}\}$. By time discretizing this relation and the current's time-evolution, expanding the algorithm to multiple feeds is vexing but trivial

$$\mathbf{v}_n = (\mathbf{w}_0 + \Delta_t \mathbf{h}_0 \mathbf{G}_{pcm,(n)})^{-1} (e^{-\frac{\Delta_t}{\tau_{rec}}} e^{-\frac{\Delta_t}{\tau_s}} \mathbf{h}_0 \mathbf{i}_{n-1} + \Delta_t \mathbf{h}_0 \mathbf{G}_{pcm,(n)} \mathbf{V}_b + \mathbf{C}_n), \quad (2.23a)$$

$$\mathbf{i}_n = e^{-\frac{\Delta_t}{\tau_{rec}}} e^{-\frac{\Delta_t}{\tau_s}} \mathbf{i}_{n-1} + (\mathbf{V}_b - \mathbf{v}_n) \Delta_t \mathbf{G}_{pcm,(n)}, \quad (2.23b)$$

where \mathbf{v}_n is a $Q \times 1$ vector containing the feed voltages at sample n , \mathbf{i}_n the currents, \mathbf{V}_b the bias voltages, \mathbf{h}_n a $Q \times Q$ matrix with the placeholder functions, $\mathbf{G}_{pcm,(n)}$ a diagonal $Q \times Q$ matrix containing the time-evolution of the material conductance at the feeds, and \mathbf{C}_n is $Q \times 1$ vector containing the *memory effects* at each feed. The weight function is chosen similarly to the single feed case - squared self admittance $W = Y_s^2$.

2.8.1. Mutual Impedance

The frequency-domain mutual impedance is plotted in Fig.2.24(a-b) for elements at two distances. Naturally, feeds with larger spacing are more decoupled - wave component of p has higher attenuation at q . Thus, the mutual impedance decreases with the distance. Additionally, it also decreases with frequency - the wave leaks faster at large f , resulting in lower coupling. Therefore, opposite to the self impedance, the discontinuity at the maximum frequency decreases. For reference, the mutual impedance impulse response is plotted in Fig.2.24(c). Indeed the Gibbs phenomenon is reduced, especially at large distance. However, small oscillatory behavior is still observed.

2.8.2. Mutual Placeholder Function

The mutual and self-impedance are multiplied with the same weight - squared self-admittance. In contrast to the self-placeholder function which is the self-admittance, the mutual placeholder function does not have any physical definition. The frequency-domain mutual placeholder function is plotted in Fig.2.25(a-b). Although no apparent discontinuity is observed, the spectral content is highly reduced - the majority of the content is located at lower frequencies. The impulse response is plotted in Fig.2.25(c). There are no obvious oscillations, however, the impulse response decays much slower due to the decreased spectral content.

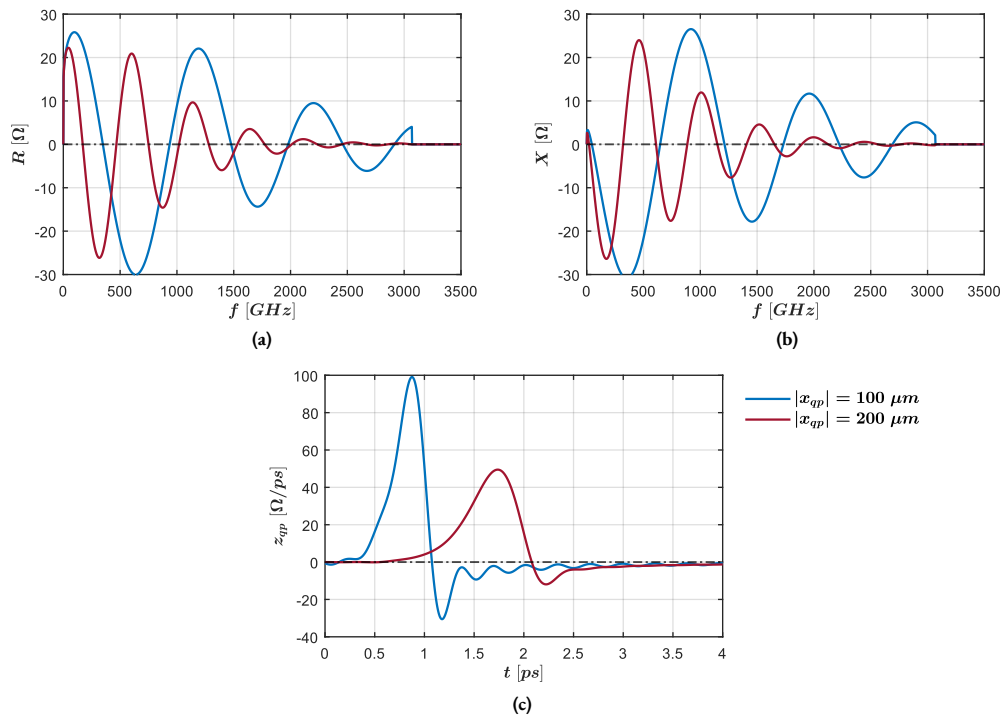


Figure 2.24: Mutual impedance for elements at two distances; in (a) the resistance, in (b) reactance, and in (c) mutual impedance impulse response.

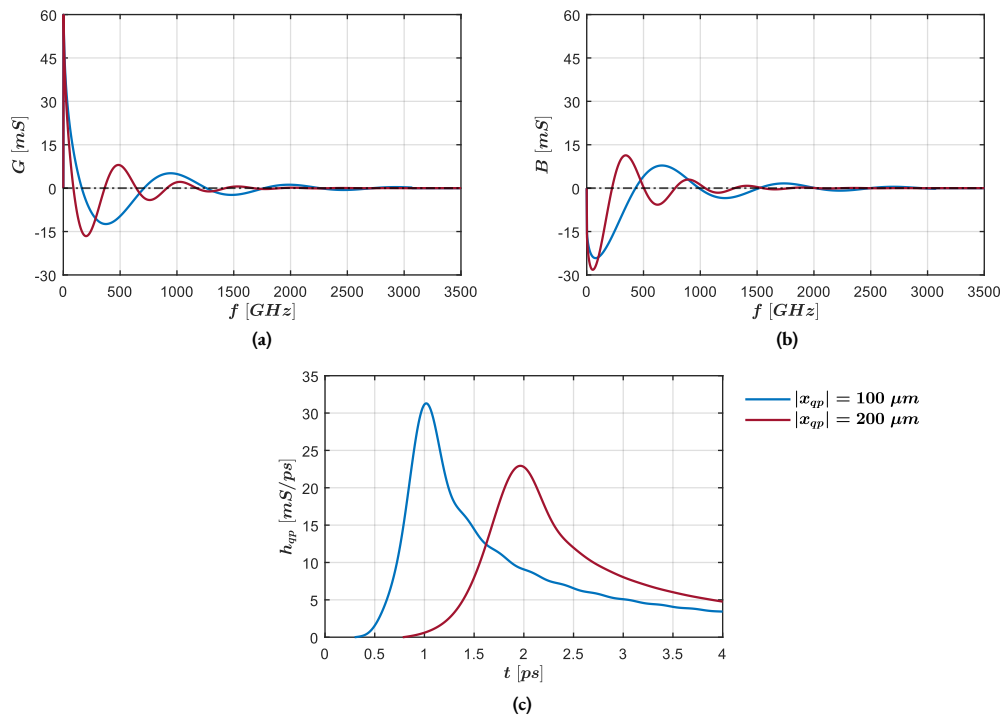


Figure 2.25: Mutual placeholder function for elements at two distances; in (a) the real part, in (b) imaginary part, and in (c) mutual placeholder impulse response.

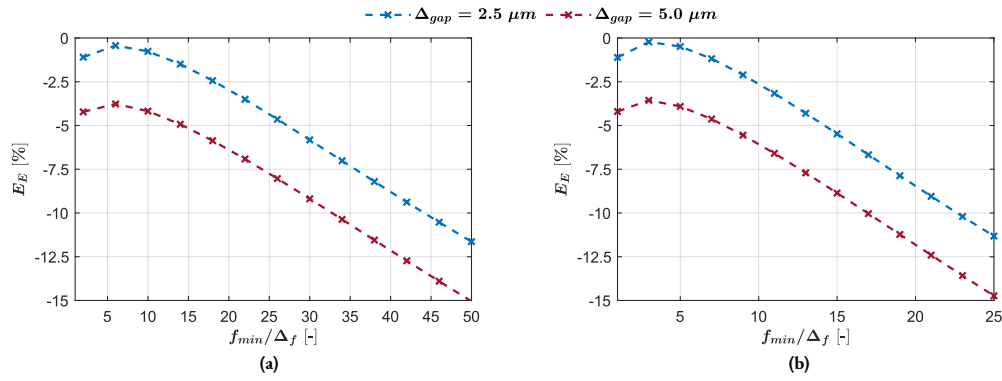


Figure 2.26: Energy error with respect to the truncation; in (a) $\Delta_f = 2.5 GHz$, and in (b) $\Delta_f = 5 GHz$.

2.8.3. Energy Error

Similarly to the single feed algorithm, the error between the time and frequency domain energy is quantified with Eq.2.17. The error, in a two feed 1D connected array, is plotted in Fig.2.26 with respect to the truncation. The feeds are spaced at distance $\Delta_x = 100 \mu m$; both are biased by $V_b = 30 V$ and excited by $\tilde{P}_{opt} = 50 mW$. Unlike the single feed case where zero error can be achieved, it might not be possible to remove the energy error in the multiple feed case. The minimum error is highly dependent on the geometry. The inability to fully optimize the error is attributed to the spectral content of the mutual placeholder function. As the majority of the content is at low frequencies, increasing the truncation negatively impacts the recovery of the impulse response². The error in Fig.2.26(a) is for frequency resolution $\Delta_f = 2.5 GHz$, while in Fig.2.26(b) for $\Delta_f = 5 GHz$. The error is evaluated for the same f_{min} (in terms of non-normalized frequency) in both cases. No evident difference between the error is observed with respect to the frequency resolution.

²The acute reader might wonder why the same weight is applied to the self and mutual impedance. A solution using two different weights was considered, but not implemented / investigated due to time considerations.

Chapter 3.

Infinite Leaky-Wave Slot

One of the most used photo-conductive antenna topologies is the tapered infinite LW slot, also known as bow-tie. Typically, the bow-tie is analyzed as a dispersive antenna with constant impedance. However, despite being broadband, in reality the impedance varies across the spectrum. Consequently, the impulse response is not a delta function, and thus the *memory* effects of the structure must be considered. Although the non-dispersive approximations allows for a good *average* power estimate, it fails to characterize the frequency dependence. With this in mind, the dispersive time-step algorithm allows for a more accurate frequency dependent analysis of these antenna structures. Moreover, as an analytical model of the bow-tie does not exist, analysis of a non-tapered slot is performed in this work. Yet, this analysis is a good starting point for describing the effects in tapered slots.

Before continuing with the analysis of the infinite leaky-wave slot, it is useful to derive an equation for the energy balance in time-domain. The derivation is performed considering a cylindrical photo-conductive gap similar to [19]. Afterwards, the power spectral density (PSD) of the dispersive time-step analysis is compared to the fully dispersive (constant impedance) antenna approximation. Next, the far-field and radiated energy (in a pulse) of the infinite leaky-wave slot are studied, and the derived energy balance equation is validated. Finally, a study on the antenna efficiency and bandwidth with respect to antenna parameters is performed.

3.1. Energy Balance Equation

Consider a cylindrical photo-conductive gap placed symmetrically around the origin and oriented in \hat{z} . The gap has a height Δ_z , and is biased by a source with potential V_b - the positive source terminal is in the lower half-space. Consequently, the bias electric field \vec{E}_b is oriented in \hat{z} from the positive to negative terminal, as shown in Fig.3.1(a). Prior to an optical excitation, \vec{E}_b causes a build up of positive and negative charges, p^+ and n^- , with equal magnitude on the positive and negative terminals respectively. After an optical excitation, an amount of charge $\Delta Q(t)$ flows through the photo-conductor resulting in two effects. Firstly, the charge flow creates a transient current distribution $j(t)\hat{z}$, where $\hat{j}(t)$ is oriented along \hat{z} , as shown in Fig.3.1(b), adhering to the conventional current definition - flow of positive charge. Secondly, a drop of charge by $\Delta Q(t)$ at the terminals leads to an electric potential drop. The electric potential drop is described as a transient terahertz field $\vec{e}(t)$ with opposite direction to \vec{E}_b , as shown in Fig.3.1(c). Therefore, using the notation in [19], the total gap electric field is $\vec{e}_{gap}(t) = E_b\hat{z} - e(t)\hat{z}$.

Fundamentally, the photo-conductive source is a switched capacitor with large capacitance C , and discharge rate controlled by an optical excitation. However, in contrast to a standard capacitor where no charge flows through the dielectric, photo-conductive sources are discharged through the photo-conductor.

Assuming the photo-conductive source is fully charged, with Q_{ini} , at the optical excitation time t_0 and according to [26], the change in potential energy at time instance t is

$$\Delta U(t) = \int_{t_0}^t v_{gap}(t)i(t)dt. \quad (3.1)$$

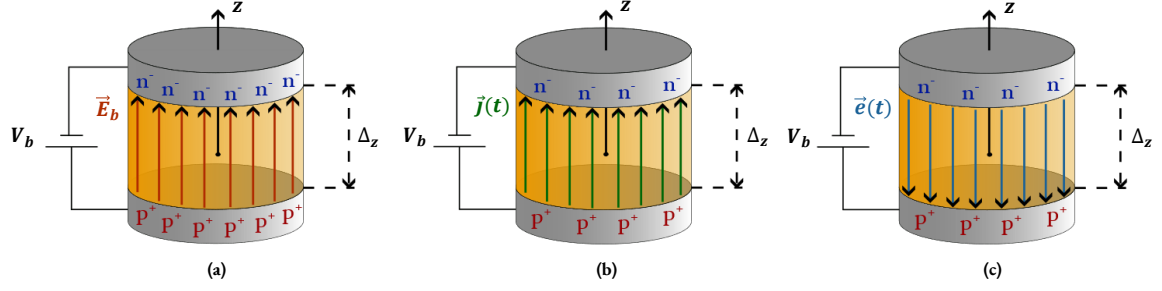


Figure 3.1: Cylindrical photo-conductive feed with delta gap Δ_z , and biased by a source with potential V_b . In (a), the bias electric field $E_b \hat{z}$, shown in red, causes a build up of positive and negative charges, p^+ and n^- , before optical excitation on the positive and negative terminals respectively. In (b), an optical excitation at time instance t causes a flow of charge $\Delta Q(t)$ over the photo-conductive gap; this flow of charge creates a current density $j(t) \hat{z}$, shown in green. In (c), the charge decrease at the terminals creates a potential drop described by a transient terahertz field $-e(t) \hat{z}$, shown in blue, opposing $E_b \hat{z}$.

Since the current is equal to the charge's rate of change, then

$$\Delta U(t) = \int_{t_0}^t v_{gap}(t) \frac{dq(t)}{dt} dt = \int_{Q_{ini}}^{Q(t)} v_{gap}(q) dq. \quad (3.2)$$

Furthermore, using the charge-voltage relation $q(t) = C v_{gap}(t)$, $\Delta U(t)$ becomes

$$\Delta U(t) = \frac{1}{C} \int_{Q_{ini}}^{Q(t)} q(t) dq = \frac{1}{2C} q^2(t) \Big|_{Q_{ini}}^{Q(t)} = \frac{1}{2} v_{gap}(t) q(t) \Big|_{Q_{ini}}^{Q(t)}. \quad (3.3)$$

Considering the charge at t is less or equal to the initial charge at t_0 , $Q(t) \leq Q_{ini}$, and the change of charge between t_0 and t being $\Delta Q(t) = Q_{ini} - Q(t)$, therefore

$$\Delta U(t) = -\frac{1}{2} v_{gap}(t) \Delta Q(t). \quad (3.4)$$

Consequently, from the potential energy to work relation $W = -\Delta U$, the total work performed in the photo-conductive gap (for one laser repetition T) is the total change of potential energy

$$W_{dis} = - \int_{U(t_0)}^{U(t_0+T)} \Delta U = \frac{1}{2} \int_{Q_{ini}}^{Q(t_0+T)} v_{gap}(t) \Delta Q. \quad (3.5)$$

In an infinitesimally small time step dt , the change of charge in dt is equal to the charge flow (current) across the gap $\Delta Q(t)/dt = i(t)$. Then, the total work performed in the gap for a period T is expressed as

$$W_{dis} = \frac{1}{2} \int_{t_0}^{t_0+T} v_{gap}(t) i(t) dt. \quad (3.6)$$

As previously described, the total electric field in the gap is the superposition of the bias and transient terahertz fields, by extension the total gap electric potential difference is $v_{gap}(t) = V_b - v(t)$, where $v(t)$ is the transient terahertz electric potential. As a result, from Eq.3.6 a relation between the transient terahertz, gap, and source energies is derived as

$$\frac{1}{2} V_b \int_{t_0}^{t_0+T} i(t) dt = \frac{1}{2} \int_{t_0}^{t_0+T} v_{gap}(t) i(t) dt + \frac{1}{2} \int_{t_0}^{t_0+T} v(t) i(t) dt. \quad (3.7)$$

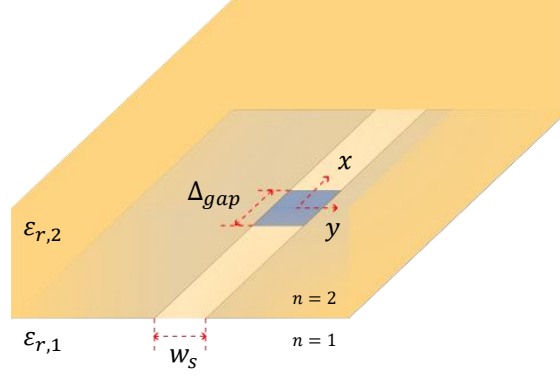


Figure 3.2: Infinite leaky-wave slot printed on a ground plane of perfect electric conductor between two homogeneous dielectrics.

The product between the time-domain voltage and current is known as the instantaneous power

$$p(t) = v(t)i(t) \quad (3.8)$$

supplied to the slot by the feed. Moreover, assuming lossless ground plane, the whole energy entering the slot (from the feed) is radiated. Consequently, the supplied (by the DC source), dissipated in the gap, and radiated energies are respectively

$$E_{SUP} = \frac{1}{2} V_b \int_{t_0}^{t_0+T} i(t) dt, \quad (3.9a)$$

$$E_{DIS} = \frac{1}{2} \int_{t_0}^{t_0+T} v_{gap}(t) i(t) dt, \quad (3.9b)$$

$$E_{RAD} = \frac{1}{2} \int_{t_0}^{t_0+T} v(t) i(t) dt. \quad (3.9c)$$

Before validating this equality, the far-field radiated power spectral density (PSD) must be evaluated.

3.2. Comparison to the Fully Dispersive Approximation

Consider an infinite leaky-wave slot printed on a perfect electric conductor (PEC) ground plane as shown in Fig.3.2. The slot is printed between two homogeneous dielectrics $n = 1$ and $n = 2$ with permittivity $\varepsilon_{r,1} = 1$ and $\varepsilon_{r,2} = 11.7$, and is fed by a photo-conductive feed with length $\Delta_{gap} = 5 \mu m$. The width is $w_s = 10 \mu m$. The higher density dielectric $n = 2$ is located in the upper hemisphere $z > 0$.

To determine whether the non-dispersive (non-constant impedance) time-step algorithm provides an advantage over the constant impedance (fully dispersive) approximation, the two methods are compared[†]. The non-dispersive analysis is performed with the parameters described in Table.1.1. While in the completely dispersive analysis, the antenna impedance is considered to be $R_{ant} = 50 \Omega$ as shown in Fig.3.3.

The frequency-domain voltage and current magnitudes (of the non-dispersive and dispersive evaluations) are compared in Fig.3.4(a-b). Considering the current, at frequencies $f \leq 1000 GHz$, there is good agreement between the two methods with a deviation of around 1 dB. On the other hand, at the spectrum's tail (above 1000 GHz), the dispersive approximation largely overestimates the magnitude. Essentially, the reactance grows which increases the mismatch between the internal and antenna loads. This behavior is not captured by the constant real impedance in the dispersive

[†]The methods used to evaluate and compare the power spectral density and average radiated power are introduced later in this chapter.

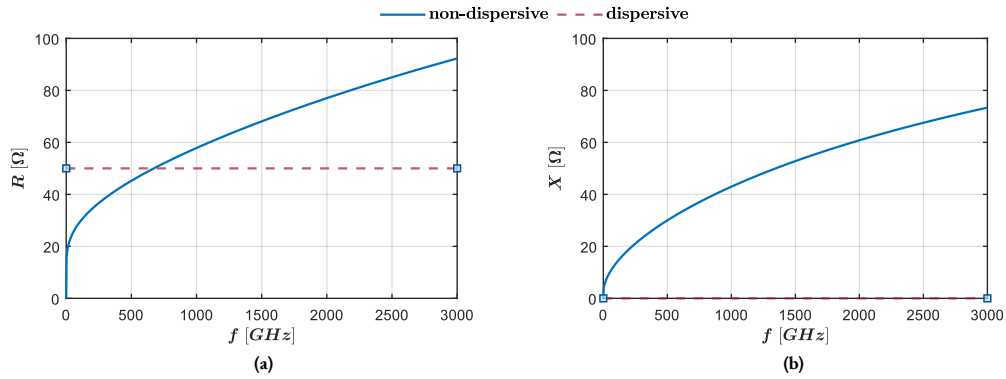


Figure 3.3: Impedance comparison between the non-dispersive and fully dispersive analysis of the infinite leaky-wave slot; in (a) the resistance, and in (b) reactance.

approximation. Furthermore, considering the voltage, the approximation largely overestimates the magnitude at low frequencies below 400 GHz. Referring to the actual antenna impedance in Fig.3.3, it goes to zero at DC corresponding to a voltage drop. Therefore, as seen in Fig.3.4(c), the non-dispersive approximation largely overestimates the power spectral density at low frequencies and in the spectrum's tail.

Comparison between the radiated average power (of the non-dispersive and dispersive evaluations) and their difference is plotted in Fig.3.5. Because the power spectral density is overestimated by the dispersive approximation, the radiated average power is on average 0.75 dB higher than the actual radiated power.

3.3. Far-Field

An infinite leaky-wave slot radiates predominantly in the denser $n = 2$ medium. The space wave contribution in the lower density $n = 1$ medium is considered negligible. Consequently, the far-field is evaluated only in $n = 2$ medium. With this in mind, there are two relevant (to this analysis) approaches in evaluating the far-field - using the electric vector potential, or the spectral convolution of Green's functions and magnetic currents.

3.3.1. Electric Vector Potential Approach

The first method is using the spatial electric vector potential $\vec{F}_n(x, y, z)$ (in medium n) associated with the magnetic currents on the slot $m(x, y)$. Then, the electric field is the curl of this electric vector potential

$$\vec{E}_n(x, y, z) = -\frac{1}{\varepsilon_n} \nabla \times \vec{F}_n(x, y, z), \quad (3.10)$$

where ε_n is the permittivity of medium n . For a narrow slot (dominant edge-singular mode), the vector potential in the denser medium is derived in [12] as

$$\vec{F}_2(x, y, z) = -\varepsilon_2 \int_{-\infty}^{\infty} \frac{e^{-jk_2 R(x-x', y, z)}}{4\pi R(x-x', y, z)} 2v_x(x') dx' \hat{x}, \quad (3.11)$$

where $R(x, y, z)$ is the radial distance, v_x the longitudinal spatial magnetic currents on the slot, and k_2 the propagation constant in medium $n = 2$.

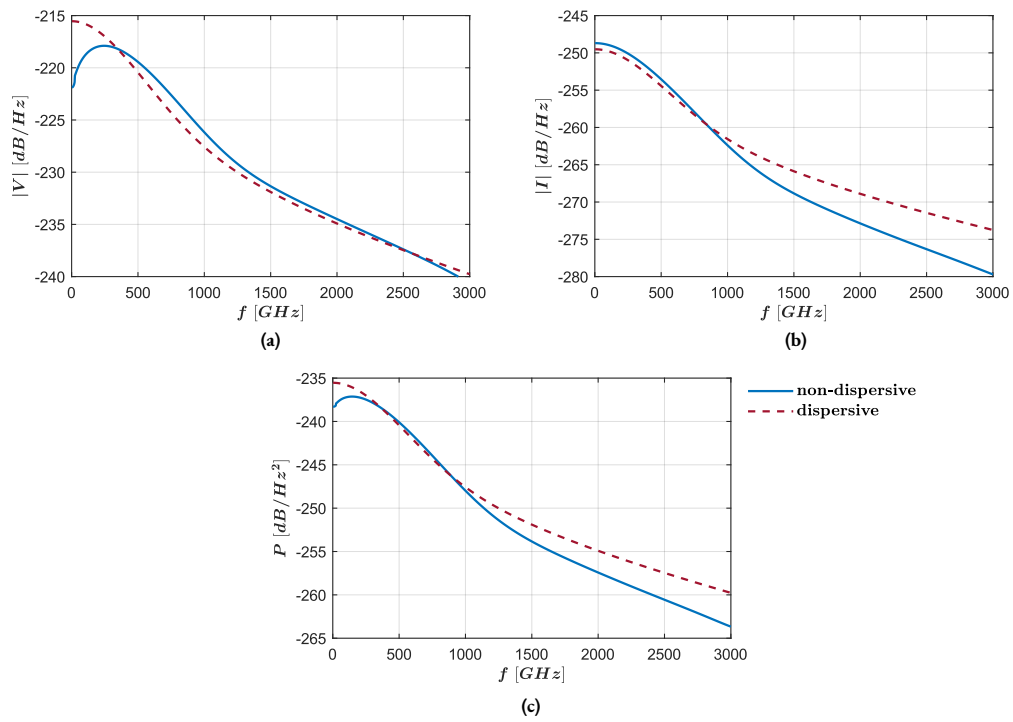


Figure 3.4: Comparison between the non-dispersive and fully dispersive analysis of the infinite leaky-wave slot; in (a) the frequency-domain voltage magnitude, in (b) current magnitude, and in (c) the power spectral density.

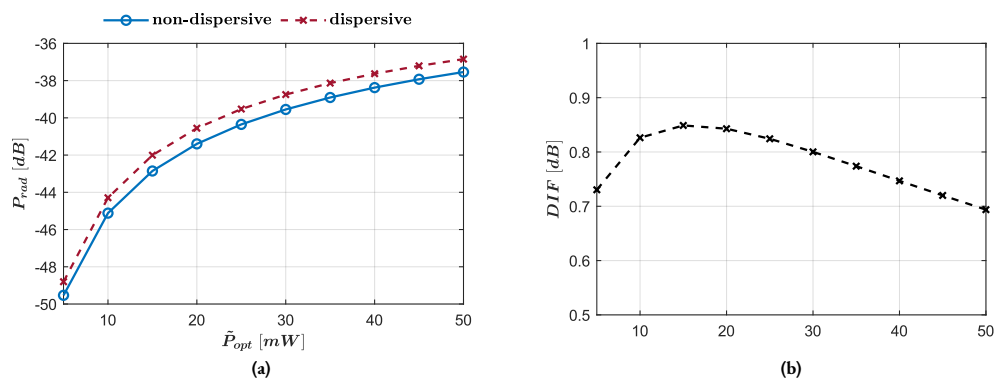


Figure 3.5: In (a) comparison between the radiated average power estimated with the non-dispersive and fully dispersive approximation, and in (b) their difference.

3.3.2. Spectral Convolution Approach

The convolution of the spectral Green's functions $\tilde{\mathbf{G}}^{\text{EM}}(k_x, k_y)$ and spectral magnetic currents $\vec{M}(k_x, k_y)$ is

$$\vec{E}(x, y, z) = \frac{1}{4\pi^2} \int_{-\infty}^{\infty} \int_{-\infty}^{\infty} \tilde{\mathbf{G}}^{\text{EM}}(k_x, k_y) \vec{M}(k_x, k_y) e^{-jk_x x} e^{-jk_y y} dk_x dk_y. \quad (3.12)$$

At the stationary phase point (a single plane wave has a dominant contribution), the integrand can be separated into slow-varying component and a component with known analytical integral solution. The slow-varying component can, in essence, be treated as a constant and taken out of the integration. Therefore, the spectral integration in Eq.3.12 has an analytical solution

$$\vec{E}_{FF}(x, y, z) = jk_{zs} \tilde{\mathbf{G}}^{\text{EM}}(k_{xs}, k_{ys}) \vec{M}(k_{xs}, k_{ys}) e^{-jk_{zs}|z-z'|} \frac{e^{-jk_n r}}{2\pi r}, \quad (3.13)$$

where k_{xs} , k_{ys} , and k_{zs} are the stationary phase point wave-number components, and z' is the observation point ($z' > 0$ m for $n = 2$, and $z' < 0$ m for $n = 1$). Both methods require knowledge of the magnetic currents.

3.3.3. Magnetic Currents

For a narrow infinite slot, the magnetic currents are well known $\vec{M}(k_x, k_y) = V_x(k_x)M_t(k_y)\hat{x}$ with $V_x(k_x)$ and $M_t(k_y)$ the longitudinal and transverse components respectively [11][27]

$$V_x(k_x) = I \frac{\text{sinc}(\frac{\Delta gap}{2} k_x)}{D(k_x)}, \quad (3.14a)$$

$$M_t(k_y) = -J_0 \left(\frac{w_s}{2} k_y \right), \quad (3.14b)$$

where I is the frequency-domain response of the evaluated current $i(t)$ using the time-step algorithm, and $D(k_x)$ is the dispersion equation derived in [11]

$$D(k_x) = \frac{1}{2k_0\zeta_0} \sum_{n=1}^2 (k_n^2 - k_x^2) J_0\left(\frac{w_s}{4} \sqrt{k_n^2 - k_x^2}\right) H_0^{(2)}\left(\frac{w_s}{4} \sqrt{k_n^2 - k_x^2}\right). \quad (3.15)$$

While $m_t(y)$ is known and has a closed form spatial FT, $v_x(x)$ is not and must be evaluated numerically using the spatial IFT on $V_x(k_x)$

$$v_x = \frac{1}{2\pi} \int_{-\infty}^{\infty} I \frac{\text{sinc}(\frac{\Delta gap}{2} k_x)}{D(k_x)} e^{-jk_x x} dk_x. \quad (3.16)$$

Essentially, the analysis of PCAs consists of evaluating the antenna impedance and impulse response, using the time-step algorithm to estimate the time-domain voltage and current, and finally evaluating the longitudinal slot voltage and far-field using the frequency-domain response of the estimated current.

By using the electric vector potential, the field can be evaluated at any point (x, y, z) in space. However, the approach requires the numerical evaluation of the spatial IFT in Eq.3.16, and the numerical integration over the slot's length in Eq.3.11 for each point of interest. On the other hand, the convolution method (at the stationary phase point) can only be used to evaluate the far-field. However, it is a much faster approach, as it does not require evaluation of the spatial IFT and integration over the slot's length. Therefore, because the near-field is of no interest in this analysis, the second method with a stratified media representation of $\tilde{\mathbf{G}}^{\text{EM}}(k_x, k_y)^2$ is used to evaluate the far-field.

²The stratified media representation of the Green's functions for the LW infinite slot are well known and discussed in previous works, as such they are not discussed in this thesis.

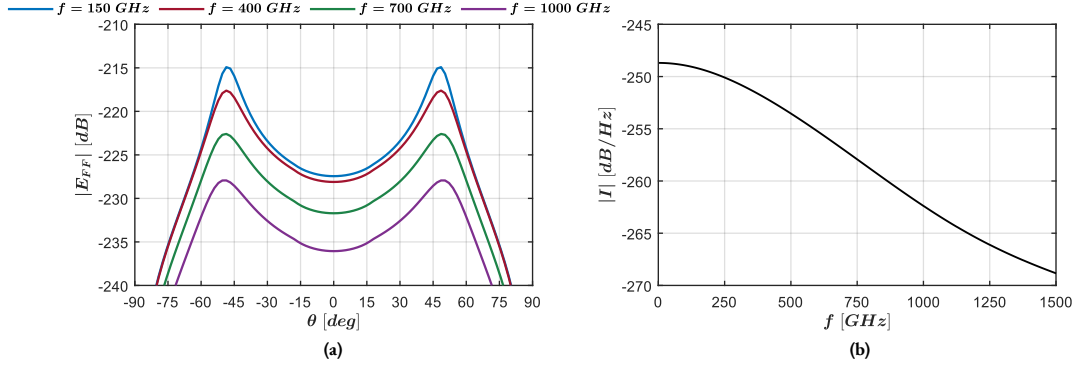


Figure 3.6: For the photo-conductive infinite leaky-wave slot in (a) the electric far-field at $R = 1\text{ m}$ and $\phi = 0\text{ deg}$, and in (b) current spectrum.

3.3.4. Temporal Far-Field

As a time-domain system, it is interesting and beneficial to investigate the far-field in time. To recover the temporal far-field, simply the IFT is used on the evaluated *spectral* far-field $\vec{e}(t) = \mathcal{F}^{-1}\{\vec{E}(f)\}$. Using the linear property of integration, the IFT of each vector component is evaluated separately

$$\vec{e}_{FF}(t) = \mathcal{F}^{-1}\{E_x^{FF}(f)\}\hat{x} + \mathcal{F}^{-1}\{E_y^{FF}(f)\}\hat{y} + \mathcal{F}^{-1}\{E_z^{FF}(f)\}\hat{z}. \quad (3.17)$$

The temporal field is a real signal and as such, the spectral far-field is conjugate symmetric. Moreover, naturally the spectral far-field carries the wave propagation information in terms of the phase. Thus, obviously the wave propagation delay at the observed radial distance is noticeable in the recovered temporal far-field.

3.3.5. Evaluation

During the study, the slot is considered with a width $w_s = 10\ \mu\text{m}$, while the feed length is $\Delta_{gap} = 5\ \mu\text{m}$. The photo-conductor absorbs $\tilde{P}_{opt} = 50\ \text{mW}$ and is biased by $V_b = 30\ \text{V}$. Finally, the denser medium is silicon with relative permittivity $\epsilon_{r,2} = 11.7$, and the lower permittivity medium is vacuum.

The evaluated electric far-field magnitude, using the stratified media Green's functions at a stationary phase-point, is plotted in Fig.3.6(a) at $R = 1\ \text{m}$ and $\phi = 0\ \text{deg}$ inside the denser medium. For reference, the current magnitude is plotted in Fig.3.6(b). Naturally, as the current decreases with frequency, the far-field also decreases.

The temporal field's components are plotted in Fig.3.7 at broadside $\theta = 0\ \text{deg}$ and $\phi = 0\ \text{deg}$. The electric field is purely y -oriented at broadside. Moreover, the wave arrives at the observation point around $t \simeq 11.41\ \text{ns}$ after the feed's excitation. Considering the speed of light in silicon and distance of $R = 1\ \text{m}$, the wave should arrive at $t = 11.4096\ \text{ns}$. Observed and calculated time of arrival have a good match. In reality, the wave might arrive slightly later as a consequence of the leakage time from the slot. At this point, it must be noted that (due to the DIFT) the time-domain is periodic with periodicity of $1/\Delta_f^3$. For a frequency step $\Delta_f = 2.5\ \text{GHz}$, this periodicity is $T = 400\ \text{ps}$; thus, the wave is observed at the 28th periodic segment.

The time-evolution of the temporal field magnitude is plotted in Fig.3.8 at $\phi = 0\ \text{deg}$ for four time steps. The LW beams are clearly visible. Finally, both time plots show the pulsed nature of the PCA.

³The periodicity is a consequence of the Poisson summation discussed in Chapter.2.1.

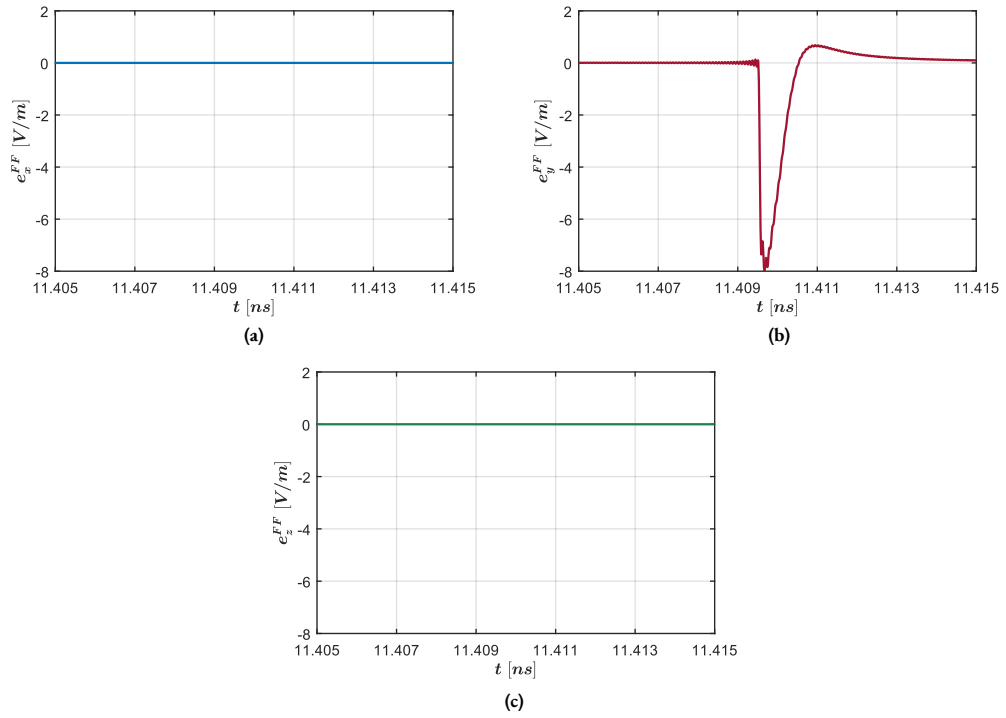


Figure 3.7: Temporal electric far-field's components, at $R = 1$ m broadside ($\theta = 0$ deg and $\phi = 0$ deg), of the photo-conductive infinite leaky-wave slot; in (a) x -component, (b) y -component, (c) z -component.

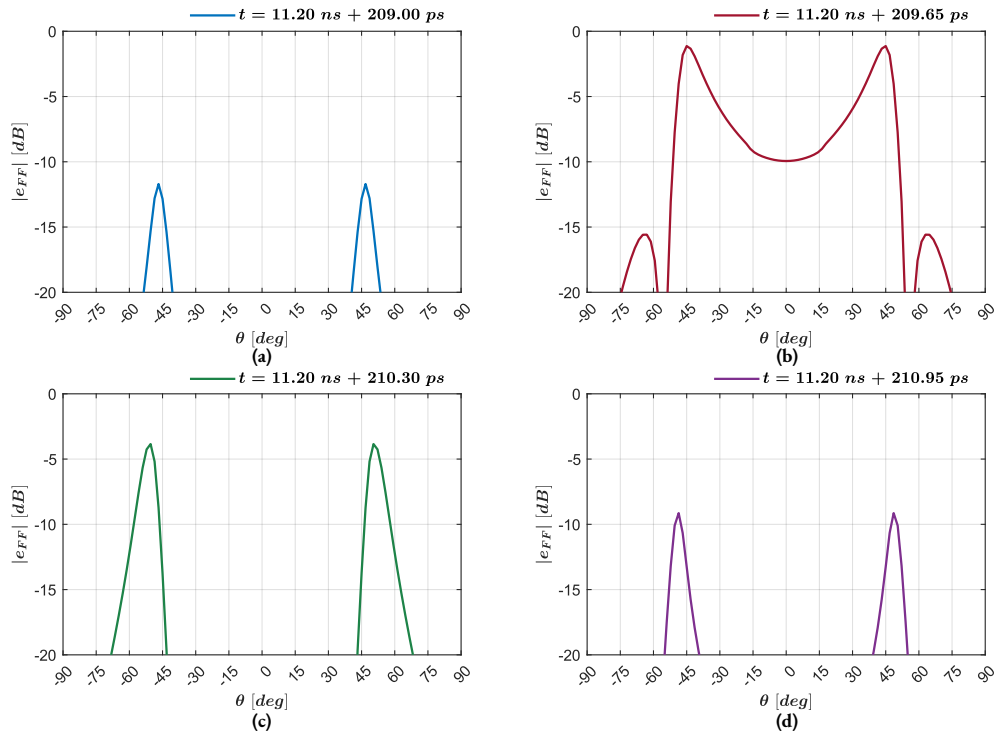


Figure 3.8: Temporal electric far-field, at $R = 1$ m and $\phi = 0$ deg, of the photo-conductive infinite leaky-wave slot; in (a) $t = 11.4090$ ns, (b) $t = 11.4096$ ns, (c) $t = 11.4103$ ns and (d) $t = 11.4109$ ns.

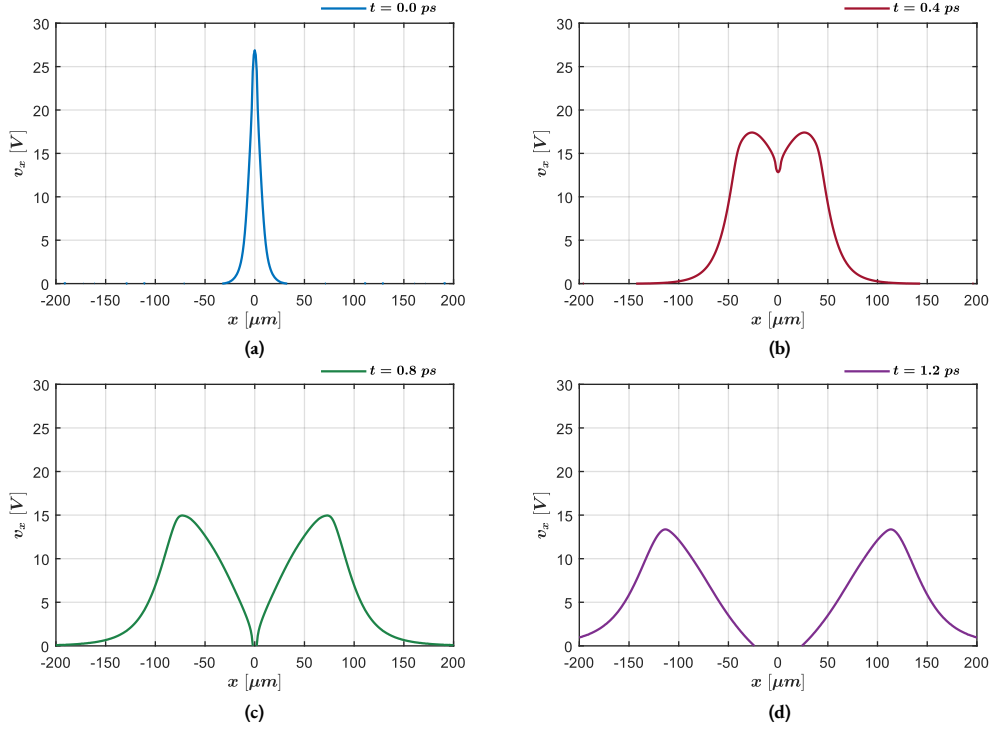


Figure 3.9: Wave propagating in a $400 \mu\text{m}$ section of the infinite leaky-wave slot; in (a) $t = 0 \text{ ps}$, (b) $t = 0.4 \text{ ps}$, (c) $t = 0.8 \text{ ps}$ and (d) $t = 1.2 \text{ ps}$.

3.4. Slot Wave

Similarly to the temporal far-field, it is interesting to investigate the wave propagating on the slot in time. To recover the temporal evolution, the IFT of the longitudinal magnetic current, slot voltage, in Eq.3.16 is evaluated

$$v'_x(x, t) = \mathcal{F}^{-1}\{v_x(x, f)\}. \quad (3.18)$$

Hence, first the spatial IFT of $V_x(k_x)$ must be evaluated, followed by the temporal IFT. This evaluation must be performed for each longitudinal point of interest x .

The propagating wave on the slot is plotted in Fig.3.9 on a $400 \mu\text{m}$ part of the slot centered at the feed. The plot visualizes the time-evolution for four steps.

3.5. Power Spectral Density

There are multiple equivalent approaches to evaluate the power spectral density (PSD) of the radiated wave. One method is to use the frequency-domain voltage and current across the photo-conductive feed. Considering the ground plane (on which the slot is printed) is perfect electric conductor (PEC), there are no losses as the wave propagates on the slot. Consequently, the active power entering the slot leaks into the denser medium. The contribution associated with the space in the less dense medium $n = 1$ is negligible - almost all of the radiated power is radiated in the higher permittivity medium. Therefore, by using the frequency-domain voltage and current, the active power is

$$P = \frac{1}{2} \Re\{VI^*\}. \quad (3.19)$$

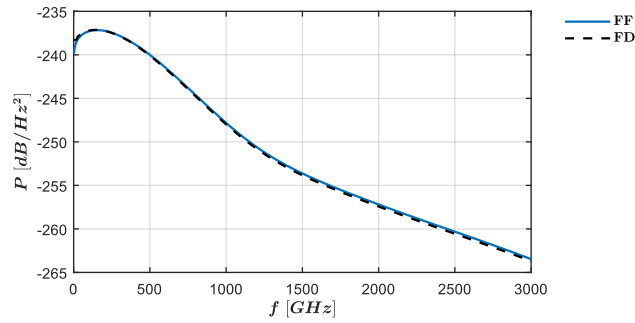


Figure 3.10: Radiated power spectral density of the photo-conductive infinite leaky-wave slot.

Needless to say, the radiated PSD in the far-field (TEM wave) is evaluated using the Poynting vector

$$\vec{S}(\theta, \phi, r) = \vec{E}_{FF} \times \vec{H}_{FF} = \frac{1}{2} \frac{|\vec{E}_{FF}(\theta, \phi, r)|^2}{\zeta_2} \hat{r}, \quad (3.20)$$

where ζ_2 is the wave impedance of the denser medium. The total power is captured in the upper hemisphere (denser medium) associated with the dominant radiation mechanism

$$P = \int_0^{2\pi} \int_0^{\pi/2} |\vec{S}(\theta, \phi, r)| \sin \theta d\theta d\phi. \quad (3.21)$$

When a lossy conductor is used as the ground plane, the power entering the slot does not equal the power in the far-field. In this case, the power losses must be considered when using the former approach or the PSD must be evaluated solely in the far-field.

The PSD is plotted in Fig.3.10 for the parameters used in the previous far-field plots. The frequency-domain and far-field evaluations are equivalent. In general, the power decreases with frequency due to the decreasing current, plotted for reference in Fig.3.6(b). However, at low frequencies (close to DC), the antenna impedance also decreases which results in a radiated power drop.

3.5.1. Average Power

The power level in Fig.3.10 are close to noise. However, the PSD represents the power radiated in one pulse with period T . A photo-conductive antenna radiates *millions* of pulses in a second. Consequently, the average radiated energy per second is

$$P_{rad} = \frac{1}{T} \int_{-\infty}^{\infty} P(f) df. \quad (3.22)$$

A photo-conductive system integrates the received power over multiple pulses. Naturally, higher power in a signal pulse means lower integration time [16]. This fact is one of the reasons to improve the radiated power of PCAs.

3.6. Energy

Referring to Eq.3.7 and following from Parseval's theorem, the energy supplied to the slot in Eq.3.9(c) should be equal to the one radiated in far-field (assuming lossless ground plane)

$$E_{RAD} = \frac{1}{2} \int_{t_0}^{t_0+T} v(t)i(t)dt = 2 \int_0^{\infty} P(f)df, \quad (3.23)$$

where the symmetry of the PSD is used. Therefore, in order to estimate the validity of the derived energy balance in Eq.3.7, the energy in the far-field is compared to the time-domain estimation. Another beneficial validity check is to compare the difference between supplied and dissipated energy to the radiated, i.e. $E_{SUP} - E_{DIS} = E_{RAD}$. However, before investigating the radiated energy, it is useful to provide a discussion on the saturation point.

3.6.1. Saturation Point

The saturation is related to the number of released carriers and drift velocity described by the Drude-Lorentz model. The current density (and by extension the current) are related to the number of released carriers and drift velocity [20]

$$\vec{j}(t) = \int_{-\infty}^t q_e n_{ave}(t, t'') \vec{v}_e(t, t'') dt'' \quad (3.24)$$

Therefore, increasing the optical power increases the number of carriers in the photo-conductor. However, larger number of carriers results in higher decrease of charges at the terminals. This charge reduction corresponds to larger voltage drop in the gap - decrease in the gap electric field. From

$$\vec{v}_e(t, t'') = \frac{q_e}{m_e} \int_{t''}^t e^{-\frac{t-t'}{\tau_s}} \vec{e}_g(t') dt', \quad (3.25)$$

the lower gap electric field reduces the drift velocity. In turn, the lower drift velocity limits the increase in the current density. At the saturation point, this limiting behavior becomes dominant and blocks the current from increasing. Moreover, from Eq.3.25, it is seen that lower carrier's effective mass and higher scattering time correspond to larger drift velocity. Consequently, photo-conductors satisfying these conditions have higher saturation current.

3.6.2. Absorbed Optical Power

The time-domain energy evaluation is compared to the far-field's in Fig.3.11(a) with respect to the absorbed optical power \vec{P}_{opt} . As seen, the match is ideal. Moreover, the rate of energy increase is higher before the saturation point, and lower after the saturation point. The radiated energy is linearly dependent on the absorbed optical power with rate of change decreasing after the saturation point. Additionally, the radiated energy is compared to the difference of supplied and dissipated in Fig.3.11(b) - no apparent deviation is observed between the two.

3.6.3. Bias Voltage

The time-domain energy evaluation is compared to the far-field's in Fig.3.12(a) with respect to the bias voltage V_b . There is no difference between the far-field and time-domain estimations. Additionally, the energy has a square relation to the bias. Moreover, the radiated energy is compared to the difference of supplied and dissipated in Fig.3.12(b). Once again, there is no difference between the two.

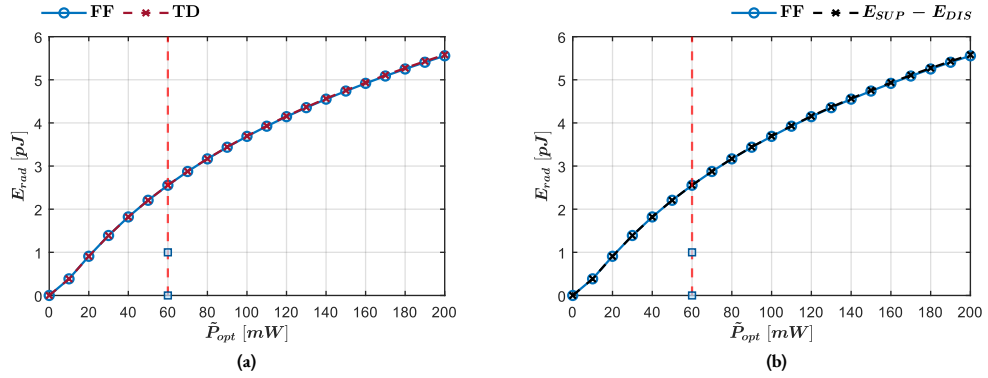


Figure 3.11: Radiated energy with respect to the absorbed optical power, the saturation point is marked with red dashed line; in (a) comparison of time-domain and far-field estimation, and in (b) difference of supplied and dissipated to radiated energy.

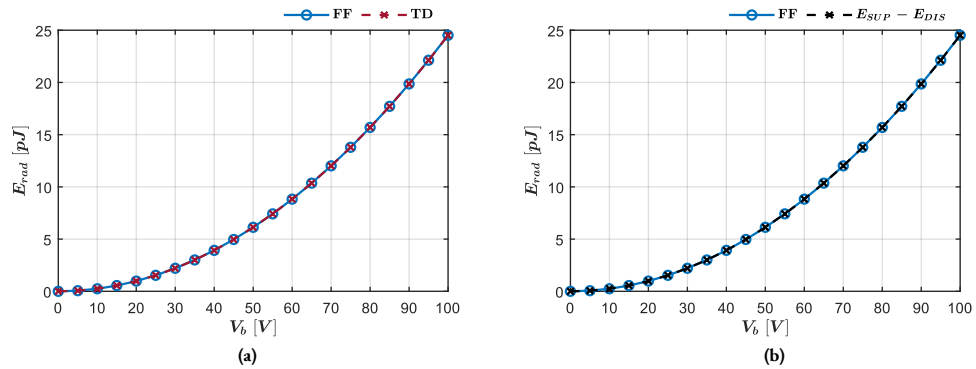


Figure 3.12: Radiated energy with respect to the bias voltage; in (a) comparison of time-domain and far-field estimation, and in (b) difference of supplied and dissipated to radiated energy.

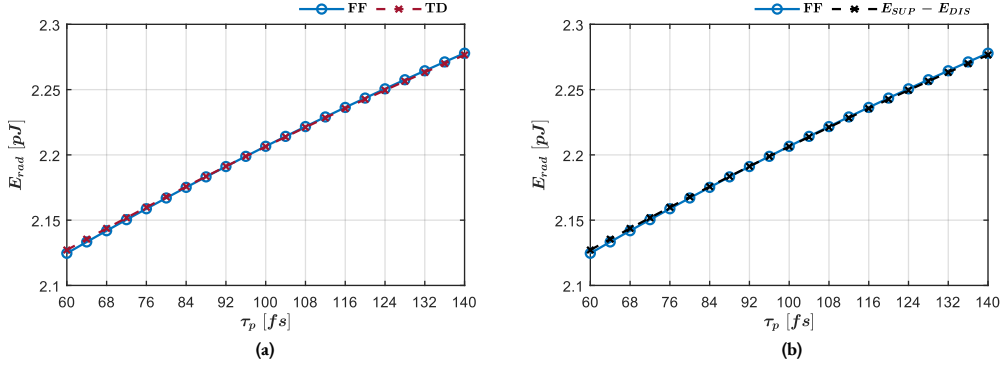


Figure 3.13: Radiated energy with respect to the laser's full width at half maximum; in (a) comparison of time-domain and far-field estimation, and in (b) difference of supplied and dissipated to radiated energy.

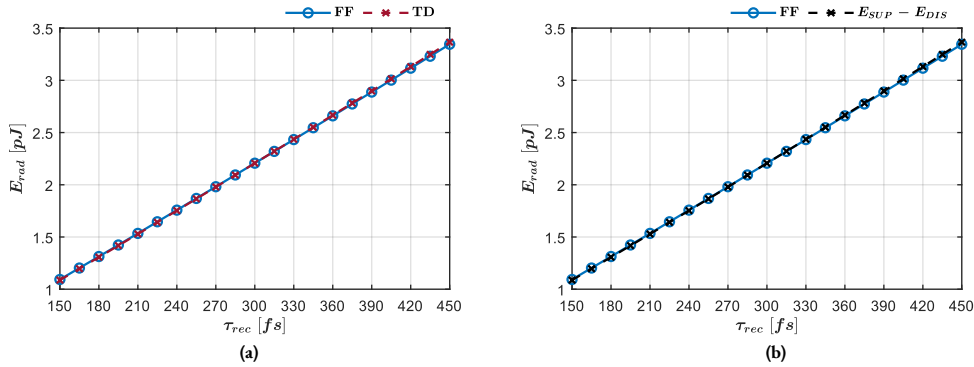


Figure 3.14: Radiated energy with respect to the recombination time; in (a) comparison of time-domain and far-field estimation, and in (b) difference of supplied and dissipated to radiated energy.

3.6.4. Full Width at Half Maximum

Next, the evaluated energy in time-domain is compared to the far-field's in Fig.3.13(a) with respect to the laser's full width at half maximum τ_p (FWHM). Once again, the difference between the energy evaluations is negligible. In addition, the relationship between the energy and FWHM is linear (or at least while τ_p is much smaller than τ_{rec}). However, the rate of change is negligible compared to the optical power. The radiated energy is compared to the difference of supplied and dissipated in Fig.3.13(b). Similar to before, no apparent difference is observed.

3.6.5. Recombination Time

Although the recombination time is dependent on the photo-conductive material and often not a design parameter, it is useful to investigate its influence on the antenna's performance. The time-domain and far-field energy evaluations are compared in Fig.3.14(a) with respect to τ_{rec} . Obviously, there is no difference between the time-domain and far-field estimations. Increasing the recombination time corresponds to linear growth in the radiated energy. The radiated energy is compared to the difference of supplied and dissipated in Fig.3.14(b) - no deviation.

The results confirm the validity of the derived energy balance in Eq.3.7. Two different comparisons are performed - radiated energy in far-field and time-domain, and difference between the radiated energy and supplied minus dissipated. There is no observable difference between these comparisons for parameter sweeps over the absorbed optical power, bias voltage, FWHM, and recombination time. Finally, it must be noted that the highest influence on the radiated energy has the bias voltage with a square relation. While the energy is dependent on the other parameters linearly.

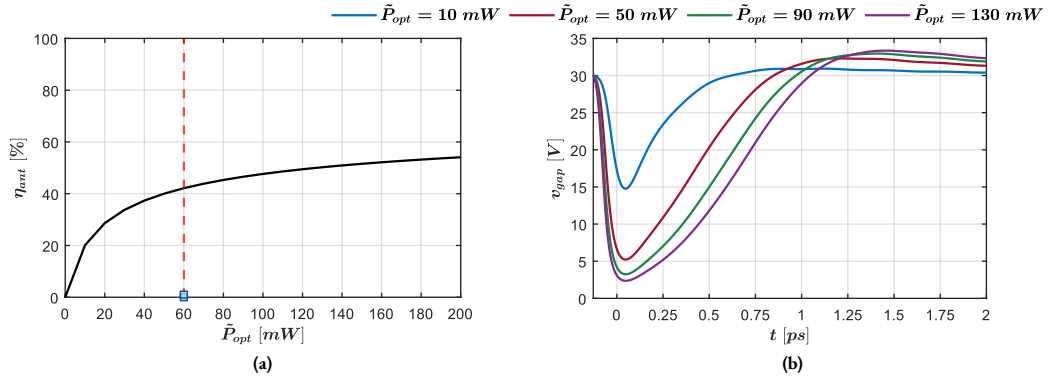


Figure 3.15: With respect to the absorbed optical power; in (a) antenna efficiency (the saturation point is marked with red dashed line), and in (b) gap voltage.

3.7. Antenna Efficiency

In the photo-conductive antenna community, it is common to define the antenna efficiency in terms of the laser's optical power. However, from Eq.3.6 follows that the bias field is responsible for the work performed on the released charges. Ergo, the antenna efficiency is defined as the ratio between the supplied and radiated energy in Eq.3.9

$$\eta_{ant} = \frac{E_{RAD}}{E_{SUP}}. \quad (3.26)$$

From these equations follows that the antenna efficiency is maximized when the transient voltage approaches the bias, i.e. the gap voltage approaches $v_{gap} = 0$ V.

The antenna efficiency is plotted in Fig.3.15(a) with respect to the absorbed optical power. Evidently, the antenna efficiency has a larger rate of increase below the saturation point. Referring to the gap voltage plot in Fig.3.15(b), the drop in the gap electric field decreases at the saturation point - the change is smaller. Consequently, the change in efficiency is also diminished. In fact, due to saturation, the gap voltage never reaches 0 V. Therefore, in terms of efficiency, the optimal absorbed optical power corresponds to the saturation point.

In terms of the bias voltage, the efficiency is plotted in Fig.3.16(a). Evidently, the efficiency is not influenced by the bias voltage. By comparing Fig.3.15(a) to Fig.3.16(a), it is concluded that the saturation point is independent of the bias voltage. Furthermore, the gap voltage is plotted in Fig.3.16(b). Obviously, higher bias corresponds to higher drift velocity, and thus larger voltage drop - more radiated energy as observed in Fig.3.12. Therefore, to maximize the radiated energy while retaining the saturation point efficiency, the bias voltage should be chosen close to the breakdown voltage of the photo-conductive material.

Further, the efficiency is plotted in Fig.3.17(a) with respect to the FWHM. Similarly to the bias voltage, the FWHM has no influence on the efficiency. However, referring to the gap voltage plot in Fig.3.17(b), it does not contribute significantly to the voltage drop. Consequently, the FWHM has a negligible influence on the energy as also observed in Fig.3.13.

Finally, the efficiency is plotted in Fig.3.18 with respect to the recombination time. Similarly to the bias and FWHM, the recombination time does not impact the efficiency. The gap voltage is plotted in Fig.3.18(b). Evidently, the recombination time has a negligible effect on the maximum amplitude of the voltage drop. However, naturally, the longer existence of carriers corresponds to a longer voltage drop. This behavior leads to a slight increase in the energy as seen in Fig.3.14.

Overall, the only parameter observed to influence the efficiency is the absorbed optical power. With this point in mind, the largest efficiency increase is achieved at the saturation point. Additionally, despite that the bias voltage does not

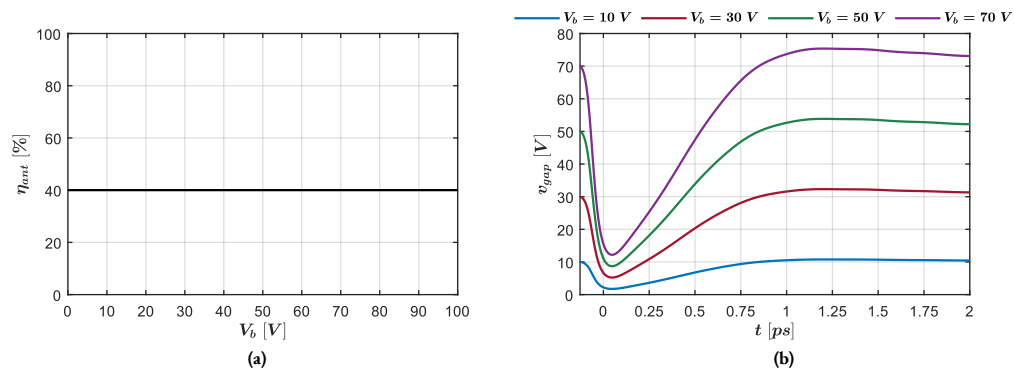


Figure 3.16: With respect to the bias voltage; in (a) antenna efficiency, and in (b) gap voltage.

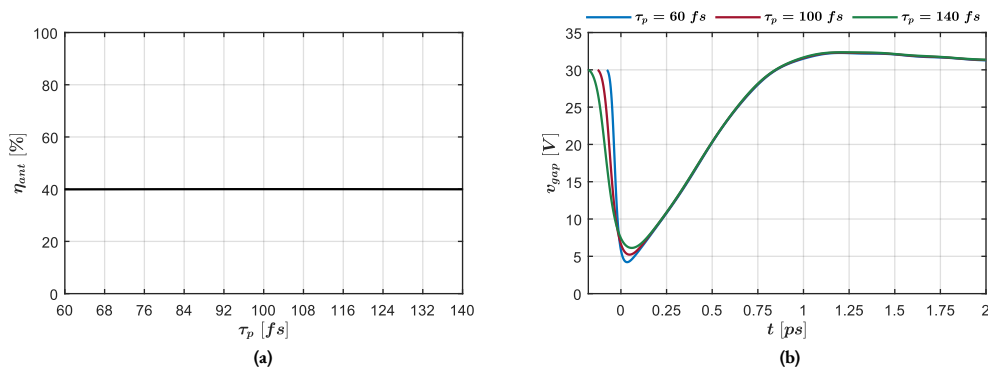


Figure 3.17: With respect to the laser's full width at half maximum; in (a) antenna efficiency, and in (b) gap voltage.

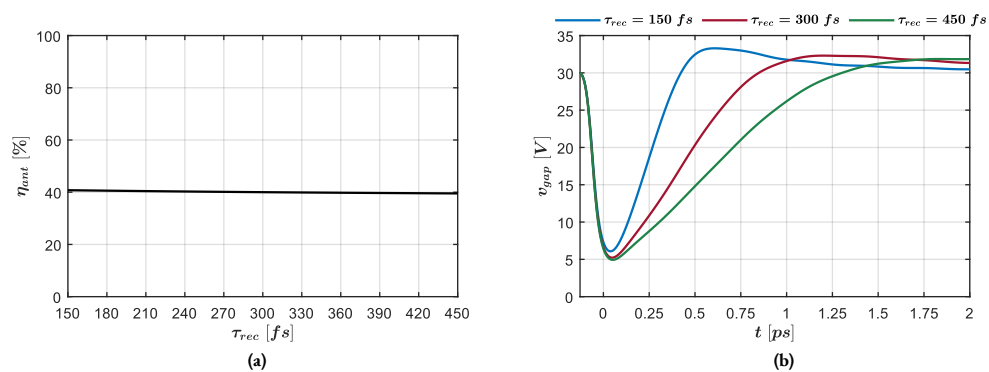


Figure 3.18: With respect to the recombination time; in (a) antenna efficiency, and in (b) gap voltage.

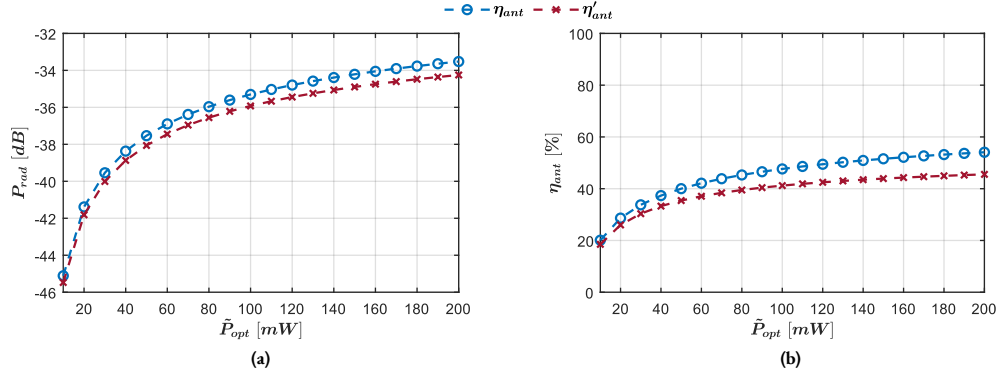


Figure 3.19: In (a) comparison between the radiated power, and in (b) between the overall efficiencies with and without accounting for lower frequency limit.

influence the efficiency, it has the greatest influence on the radiated energy. Therefore, to maximize the radiated energy, the bias voltage should be close to the photo-conductor's breakdown voltage.

3.7.1. Lower Frequency Limit

In reality, the quasi-optical lens is designed to operate above a certain frequency. For frequencies below this nominal point, the lens is electrically small. Thus, the geometrical optics (GO) and physical optics (PO) approximations cannot be applied.

Additionally, although the slot is considered infinite in the models, the physical slot has a certain length. This length is chosen such that, at the frequencies of interest, the wave has already leaked by the time it arrives at the termination. Meaning at the frequencies of interest, the slot is indeed approximated as infinite. However, at lower frequencies, the LW attenuation constant decreases and the wavelength increases. Thus, the wave does not sufficiently leak until it reaches the terminations, and the infinite slot approximation fails. Consequently, considerable portion of the power is dispersed from the slot's boundaries.

As a consequence, a more accurate efficiency is defined by considering the radiated power over a certain frequency

$$\eta'_{ant} = \frac{2 \int_{f'}^{\infty} P(f) df}{E_{SUP}}. \quad (3.27)$$

Essentially, an additional efficiency is defined as

$$\eta' = \begin{cases} 0 & \text{for } f < f', \\ 1 & \text{for } f \geq f'. \end{cases} \quad (3.28)$$

A comparison between the radiated power with and without accounting for this new efficiency is plotted in Fig.3.19(a). Further, a comparison between the overall efficiencies is plotted in Fig.3.19(b). The considered minimum frequency f' in the comparison is $f' = 75 \text{ GHz}$ chosen as the quasi-optical link cut-off frequency in [20].

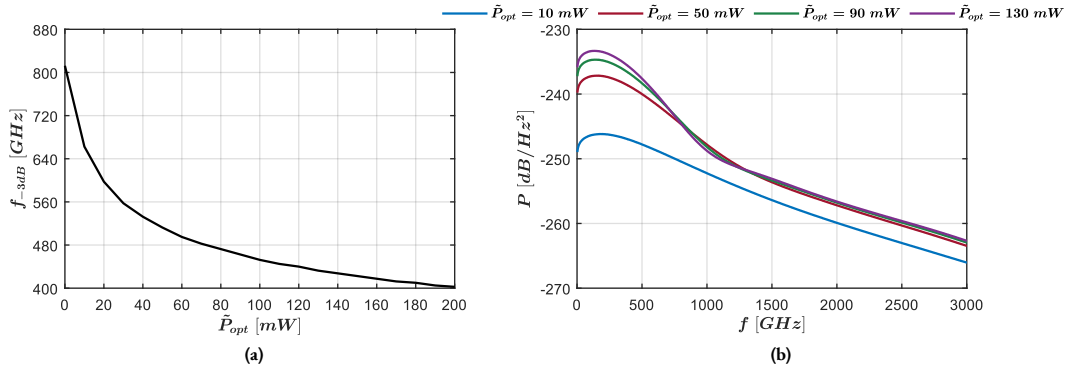


Figure 3.20: With respect to the absorbed optical power; in (a) bandwidth, and in (b) radiated power.

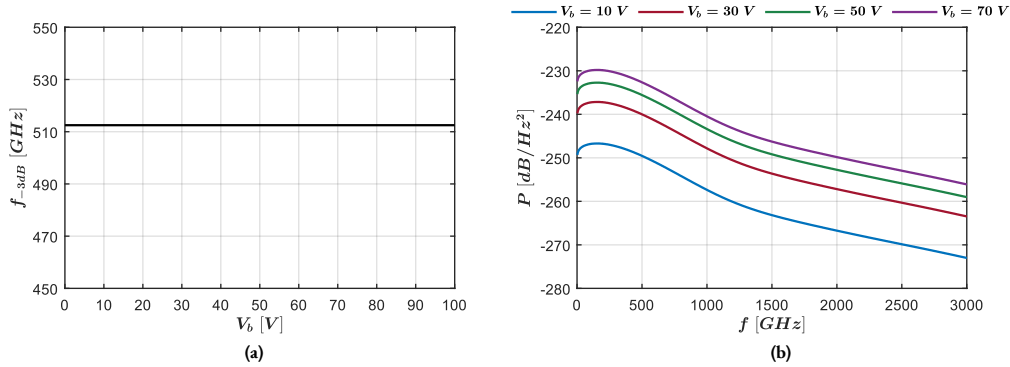


Figure 3.21: With respect to the bias voltage; in (a) bandwidth, and in (b) radiated power.

3.8. Bandwidth

Investigating the change in the half-power point f_{-3dB} (-3 dB point or bandwidth) with respect to the discussed parameters is beneficial in providing complete design guidelines. Naturally, the bandwidth is defined as the frequency point at which the radiated power drops by half from its maximum value.

The bandwidth is plotted in Fig.3.20(a) with respect to the absorbed optical power. Increasing the optical power corresponds to a large drop in the bandwidth - inverse exponential relation. For reference, the PSD is plotted in Fig.3.20(b). In fact, higher optical power leads to a disproportionate increase at lower frequencies. In essence, considering the laser's Gaussian temporal behavior, increasing \tilde{P}_{opt} results in a larger charge density. Further, as the number of carriers is given by the convolution of the photo-conductor's impulse response (related to τ_{rec}) and the charge density [20], there are more available charges at later time instances. Thus, the length of the time-domain response increases and frequency-domain response becomes narrower.

In terms of the bias voltage, the bandwidth is plotted in Fig.3.21(a). As seen, the bias has no effect on the bandwidth. Referencing the PSD plot in Fig.3.21(b), indeed higher bias increases proportionally the power at all frequencies.

Further, the bandwidth is plotted in Fig.3.22(a) with respect to the FWHM. Assuming τ_p is much smaller than τ_{rec} , there is no significant decrease in the $-3dB$ point. Obviously, under the same assumption, the PSD change in Fig.3.22(b) is insignificant.

Finally, the bandwidth is plotted in Fig.3.23 with respect to the recombination time. This parameter also has an inverse exponential relation, and the largest influence on the bandwidth. The PSD is plotted in Fig.3.23(b). Evidently, increasing the recombination time moves power to lower frequencies. Considering the time-domain behavior, obviously the

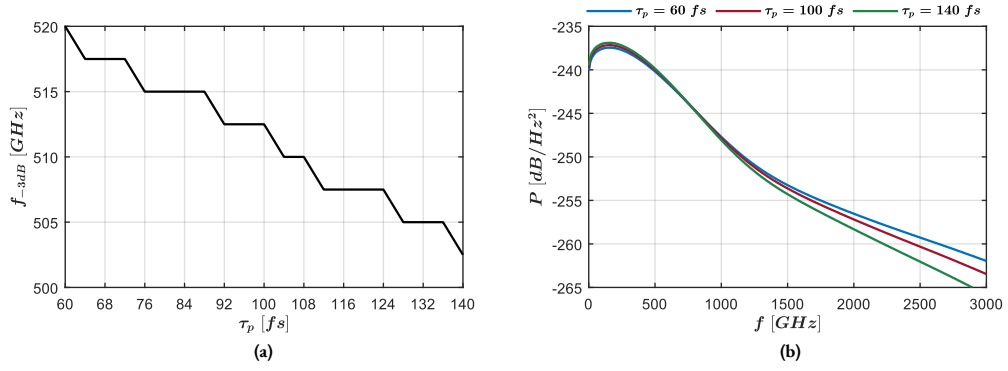


Figure 3.22: With respect to the full width at half maximum; in (a) bandwidth, and in (b) radiated power.

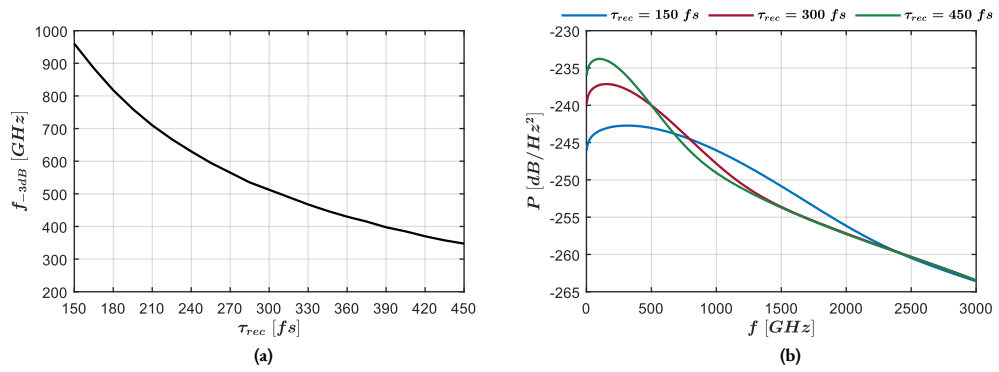


Figure 3.23: With respect to the recombination time; in (a) bandwidth, and in (b) radiated power.

response is longer for larger τ_{rec} . Therefore, it is expected that the frequency response is narrower.

Chapter 4.

1D Connected Array

The major advantage of the non-dispersive time-step algorithm is in the analysis of photo-conductive connected arrays (PCCAs). In former analysis, the photo-conductive feeds are considered completely decoupled. As such, the wave component, excited by a feed, does not interact with any other feeds. Thus, the constant impedance approximation can be applied to each feed individually. By extension the total radiated power is the sum of the power supplied to the slot by each feed. However, the feeds are not completely decoupled in reality. Therefore, a power loss is expected due to coupling. The dispersive time-step algorithm provides the advantage of modeling the mutual interaction between feeds, and intrinsically includes the associated power loss.

The novelty of the provided analysis originates from the new non-dispersive time-step algorithm. With this point in mind, the chapter begins by expanding the energy balance equation to multiple feeds (also referred to elements) and subsequently providing a validation. Then, the mutual coupling is discussed, characterized, and complemented by a discussions on the embedded admittance and efficiency. Third, analysis on the far-field and active admittance of PCCA is provided. A brief study of the far-field of progressively excited feeds is also included. Finally, a radiated power comparison to an array modeled using the constant impedance approximation is made.

In a connected array, the total excitation is the superposition of the excitations $I_q = \mathcal{F}\{i_q\}$ at all photo-conductive sources [28]

$$I_e(k_x) = \sum_{q=1}^Q I_q e^{jk_x(q-Q_{mid})\Delta_x}, \quad (4.1)$$

where Δ_x is the spacing between feeds, q the feed index, and $Q_{mid} = 0.5 + Q/2$ denotes the middle point on the slot in terms of elements.

4.1. Energy Balance Equation

In an array, the total radiated energy is the sum of the energy supplied by each feed, assuming lossless ground plane. Therefore, expanding the energy balance in Eq.3.7 is trivial - the contributions of all feeds must be considered

$$\sum_{q=1}^Q \frac{1}{2} V_{b,q} \int_{t_0}^{t_0+T} i_q(t) dt = \sum_{q=1}^Q \frac{1}{2} \int_{t_0}^{t_0+T} v_{gap,q}(t) i_q(t) dt + \sum_{q=1}^Q \frac{1}{2} \int_{t_0}^{t_0+T} v_q(t) i_q(t) dt. \quad (4.2)$$

Obviously, the total supplied, dissipated, and radiated energies are the sum of all respective contributions

$$E_{SUP} = \sum_{q=1}^Q \frac{1}{2} V_{b,q} \int_{t_0}^{t_0+T} i_q(t) dt = \sum_{q=1}^Q E_{SUP,q}, \quad (4.3a)$$

$$E_{DIS} = \sum_{q=1}^Q \frac{1}{2} \int_{t_0}^{t_0+T} v_{gap,q}(t) i_q(t) dt = \sum_{q=1}^Q E_{DIS,q}, \quad (4.3b)$$

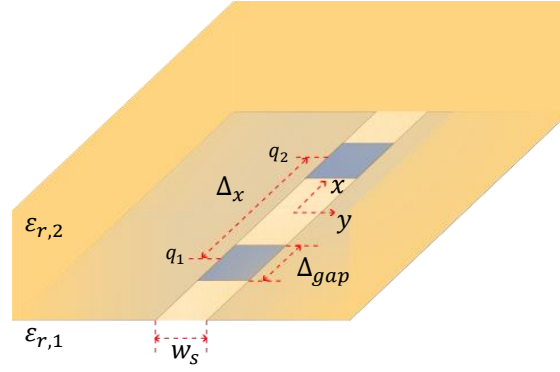


Figure 4.1: 2-element 1D photo-conductive connected array between two homogeneous dielectrics.

$$E_{RAD} = \sum_{q=1}^Q \frac{1}{2} \int_{t_0}^{t_0+T} v_q(t) i_q(t) dt = \sum_{q=1}^Q E_{RAD,q}. \quad (4.3c)$$

The validity of this energy balance relation is confirmed similarly to the single feed relation. First, the radiated energy evaluated in TD is compared to the far-field evaluation. Followed by a comparison between E_{RAD} and the difference of supplied and dissipated energies $E_{SUP} - E_{DIS}$. This validation is performed with respect to the absorbed optical powers and bias voltage. Each element is considered to be excited by the same optical power $\tilde{P}_{opt} = \tilde{P}_{opt,q}$ and bias voltage $V_b = V_{b,q}$ for $\forall q$.

Completely minimizing the energy error using the same weight, for the self and mutual impedance, can be unattainable due to the mutual impedance spectral content distribution as discussed in Chapter.2.8.3. This task becomes more unachievable for arrays with larger element spacing and more elements, i.e. larger edge element distance corresponding to faster mutual impedance attenuation. With this point in mind, the TD to far-field energy comparison is made for a 2-element array of feeds with length $\Delta_{gap} = 2.5 \mu m$, biased and excited by $V_b = 30 V$ and $\tilde{P}_{opt} = 50 mW$, and at distance $\Delta_x = 100 \mu m$. The 2-element PCCA is shown in Fig.4.1. These parameters correspond to the least error $E_E < 1\%$.

4.1.1. Absorbed Optical Power

A comparison between the radiated energy evaluated in TD and far-field is plotted in Fig.4.2(a) with respect to \tilde{P}_{opt} . The difference between supplied and dissipated energy is compared to the radiated in Fig.4.2(b). First, the three energy evaluations have an ideal match - validating the energy balance equation for connected arrays. Moreover, similarly to the single feed PCA, the relation between the radiated energy and optical power is generally linear with rate of change decreasing after the saturation point.

Obviously, the radiated energy by a 2-element 1D PCCA is roughly twice the radiated energy by a single feed PCA. The critical reader might note that these results are for $\Delta_{gap} = 2.5 \mu m$, while the single feed PCA results presented in Chapter.3.6.2 are for $\Delta_{gap} = 5 \mu m$. However, for a laser excitation uniformly distributed across the feed's surface, the delta gap does not influence the current time-evolution [20]

$$A_q = \frac{\tilde{P}_{opt,q}}{hf_c} \frac{T_L}{\sqrt{2\pi\sigma_t^2}} \frac{1}{\Delta_{gap} w_z w_s}, \quad (4.4a)$$

$$i_q(t) = A_q \frac{q_e^2}{m_e} \frac{\Delta_{gap} w_z}{w_s} \int_{-\infty}^t e^{-\frac{1}{2} \left(\frac{t'' - \tau_{d,q}}{\sigma_t} \right)^2} e^{-\frac{t-t''}{\tau_{rec}}} \int_{t''}^t v_{gap,q}(t') e^{-\frac{t-t'}{\tau_s}} dt' dt'', \quad (4.4b)$$

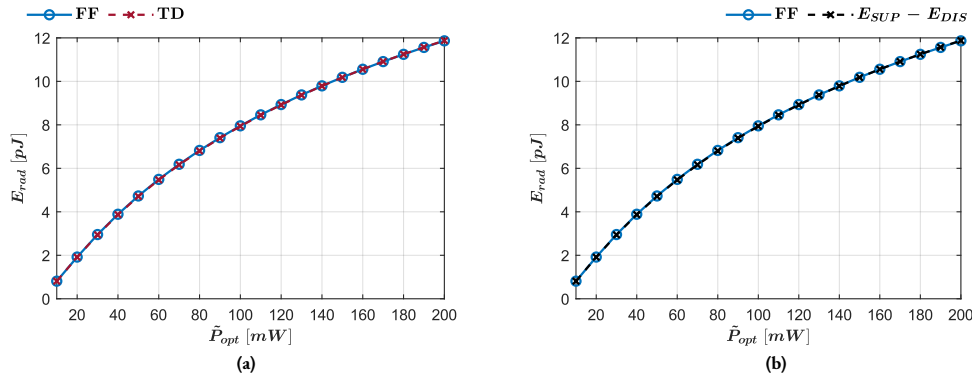


Figure 4.2: Radiated energy with respect to the absorbed optical power of a 2-element photo-conductive 1D connected array; in (a) comparison of time-domain and far-field evaluation, and in (b) difference of supplied and dissipated to radiated energy.

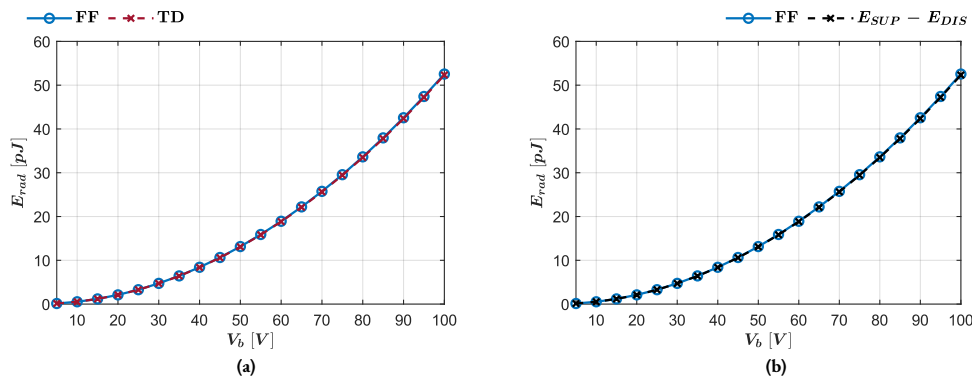


Figure 4.3: Radiated energy with respect to the bias voltage of a 2-element photo-conductive 1D connected array; in (a) comparison of time-domain and far-field evaluation, and in (b) difference of supplied and dissipated to radiated energy.

where the Δ_{gap} and height w_z cancel out. The delta gap changes the impedance though, but the difference in the resistance (influencing the active power) is negligible, while in the reactance (influencing the internal to antenna load matching) is larger at the spectrum's tail above $f \geq 1000$ GHz.

4.1.2. Bias Voltage

The TD and far-field evaluations are compared in Fig. 4.3(a) with respect to V_b . The radiated energy is compared to $E_{SUP} - E_{DIS}$ in Fig. 4.3(b). First, the energy evaluations have an ideal match. Second, the radiated energy has a square relation to the bias voltage, similarly to the single feed PCA. Finally, once again the energy is roughly twice the energy radiated by a single feed antenna.

Nevertheless, the radiated energy does not correspond to the energy of a single feed PCA multiplied by the number of feeds in larger element arrays. In reality, lower radiated power is expected due to the mutual coupling.

4.2. Mutual Coupling

The analysis of the PCCA is incomplete without a study on the mutual coupling between elements. To this end, a photo-conductive feed (referred as $q = 2$) is surrounded by two unbiased photo-conductive elements (referred as $q = 1$ and $q = 3$) acting as photo-conductive loads. The feed is biased by V_b , while all elements absorb equal optical power $\tilde{P}_{opt} = \tilde{P}_{opt,q}$ for $\forall q$. The loads are excited simultaneously at $\tau_{e,1} = \tau_{e,3}$, and the feed at $\tau_{e,2} = 0$ ps. Thus, the loads'

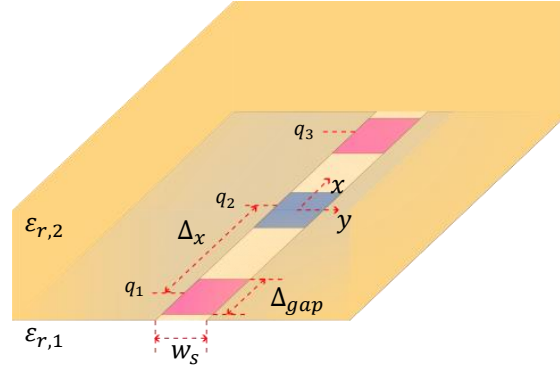


Figure 4.4: Photo-conductive antenna loaded with two photo-conductive loads (in magenta) surrounding the feed (in blue).

excitation delay is defined as

$$\Delta\tau = \tau_{e,1} - \tau_{e,2} = \tau_{e,3} - \tau_{e,2}. \quad (4.5)$$

The 3-element (photo-conductive feed surrounded by two photo-conductive loads) structure used to study the mutual coupling is shown in Fig.4.4.

The total supplied energy to the 3-element system is solely provided by the feed's bias source $E_{SUP} = E_{SUP,2}$. Furthermore, as there are no bias fields, the photo-conductive loads' gap voltages are $v_{gap,1} = -v_1$ and $v_{gap,3} = -v_3$. Consequently, the charges in the loads are accelerated in the opposite direction to the charges in the feed - the currents i_1 and i_3 are opposite to i_2 . Referring to the energy balance in Eq.4.2, the careful reader notices that the $q = 1$ and $q = 3$ contributions to the radiated energy become negative. These terms represent the induced energy in the loads by the wave launched from the feed

$$E_{IND,q} = \frac{1}{2} \int_{t_0}^{t_0+T} v_q(t) i_q(t) dt \text{ for } q = 1, 3. \quad (4.6)$$

In essence, the total radiated energy is the difference between the energy entering the slot from $q = 2$ and exiting from $q = 1$ and $q = 3$. On the other hand, all contributions to the dissipated energy are positive, and these terms still represent the dissipated energy in moving the charges across the elements. In fact, all the dissipated energy at the loads is induced from the slot, i.e. the terms cancel out in Eq.4.2.

Naturally, the mutual coupling is highly dependent on the element spacing Δ_x and excitation delay $\Delta\tau$. Therefore, the energies defined in Eq.4.3 and antenna efficiency (without accounting for the QO link) are studied with respect to these two parameters. In the study, the elements' delta gaps are $\Delta_{gap} = 5 \mu m$, while the absorbed optical power and bias voltage (at the feed) are $\tilde{P}_{opt} = 50 mW$ and $V_b = 30 V$.

4.2.1. Element Spacing

The supplied, radiated, and dissipated energies are plotted in Fig.4.5(a) with respect to the element spacing. The excitation delay is $\Delta\tau = 0 ps$. At closely spaced elements, the reflections from the loads are larger. When these reflections arrive back at the feed, the antenna impedance (seen from the feed) changes significantly. As a result, the feed current response is altered more. This change corresponds to higher current, and hence more energy supplied by the DC source. The current magnitude (at the feed) is plotted in Fig.4.6(b) for $\Delta_x = 25 \mu m$ and $\Delta_x = 100 \mu m$. Indeed, the current increases for smaller element spacing.

However, there is a substantial reduction in the radiated energy and increase in the dissipated energy due to two effects. First, more energy is induced at the loads - the wave launched (by the feed on the slot) arrives while the loads are *more*

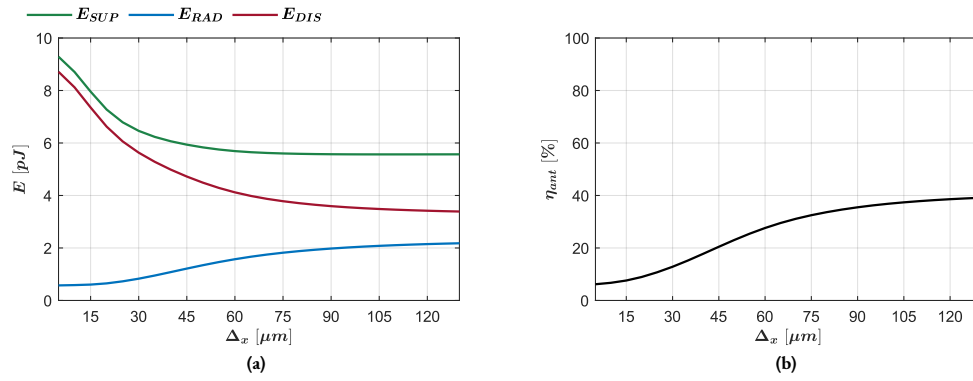


Figure 4.5: In (a) supplied, radiated, and dissipated energy, and in (b) antenna efficiency with respect to the element distance.

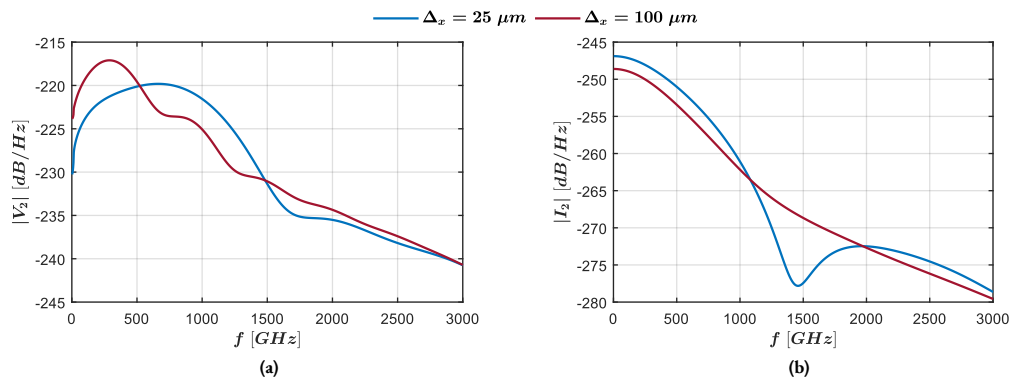


Figure 4.6: Feed response of a photo-conductive antenna loaded with two photo-conductive loads; in (a) the voltage magnitude, and in (b) current magnitude.

active and less energy has leaked by the time of arrival. Second, the impedance mismatch between the antenna and internal loads increases as a result of the antenna impedance change. To verify the latter point, the voltage magnitude (at the feed) is plotted in Fig.4.6(a). The voltage is lower for smaller element spacing indicating worse matching.

The antenna efficiency is plotted in Fig.4.5(b). Naturally, the radiated energy reduction and supplied energy increase result in lower efficiency. On the other hand, the operating frequency of the array is increased (for smaller element distance).

4.2.2. Excitation Delay

The energies are plotted in Fig.4.7(a) with respect to the excitation delay. The element spacing is $\Delta_x = 100 \mu\text{m}$. The load reflections do not arrive at the feed while being active - no change in the supplied energy. Yet, as the excitation delay approaches the time of arrival, more energy is induced at the loads. Therefore, the radiated energy decreases, and total dissipated energy increases. The antenna efficiency is plotted in Fig.4.7(b). The larger dissipated energy in the loads corresponds to lower efficiency.

4.2.3. Cut-Off Frequency

Before investigating impedance seen by the feed (due to the photo-conductive load interactions), it is useful to define the cut-off frequency. In connected arrays, destructive interference occurs at the frequency f_0 (cut-off frequency) at which

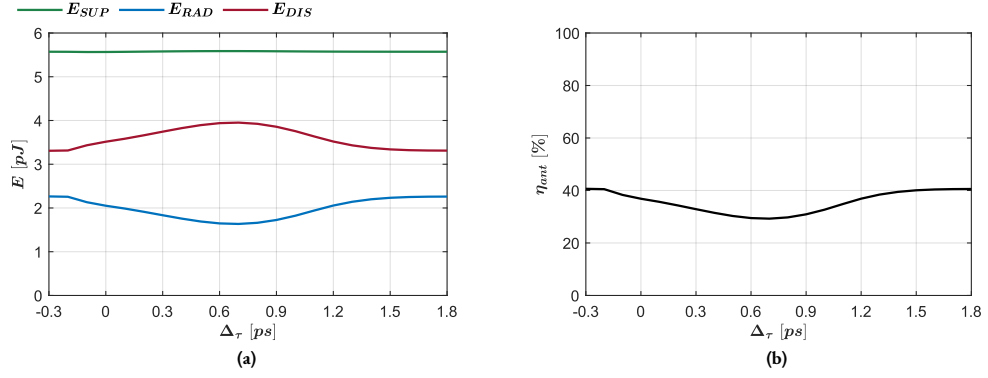


Figure 4.7: In (a) supplied, radiated, and dissipated energy, and in (b) antenna efficiency with respect to the excitation delay.

the element spacing is equal to half of the effective wavelength $\Delta_x = \lambda_0/2$ [28]–[30]

$$f_0 = \frac{c_0}{2\Delta_x \sqrt{\varepsilon_{r,eff}}}, \quad (4.7)$$

where c_0 is the speed of light in vacuum, and $\varepsilon_{r,eff} = (\varepsilon_{r,1} + \varepsilon_{r,2})/2$ the effective wavelength. In essence, when considering the wavelength, the phase difference between the wave components launched by the feeds becomes $\geq 180^\circ$. Consequently, this behavior has also a periodicity of f_0 .

4.2.4. Embedded Impedance

Instead of investigating the mutual coupling effects on the voltage and current separately, the analysis can be performed by studying directly the impedance. With this point in mind, the impedance seen from the feed (element $q = 2$) is defined as embedded

$$Z_{emb} = \frac{V_2}{I_2}. \quad (4.8)$$

It is a useful parameter to characterize the effects in the far-field and power due to the interactions between the elements.

The embedded impedance is plotted in Fig.4.8 for $\Delta_x = 25 \mu m$ and $\Delta_\tau = 0 ps$. The frequency is normalized to f_0 . For reference, the impedance of an unloaded photo-conductive antenna is plotted with dashed black line. Indeed, the impedance is overall lower corresponding to less radiated power[10]. Additionally, the reactance increases up to around $f = 0.5f_0$ (for $\Delta_x = 25 \mu m$, the cut-off frequency is $f_0 \simeq 2400 GHz$), corresponding to the larger internal to antenna load mismatch. On the other hand, there is a peak in the impedance corresponding to larger radiated power, but the feed does not excite this part of the spectrum sufficiently.

The embedded impedance is plotted in Fig.4.9 for $\Delta_x = 25 \mu m$ and $\Delta_\tau = 0 ps$. At larger element spacing, more power is radiated by the wave's time of arrival at the photo-conductive loads. Additionally, the loads are less active when the wave arrives. Consequently, the antenna behaves closer to a unloaded infinite leaky-wave (LW) slot.

The embedded impedance is plotted in Fig.4.10 for two excitation delays and $\Delta_x = 100 \mu m$. For the simultaneous excitation, the wave arrives at the loads when they are less active. As a result, the reflections are small and the structure approximates the infinite LW slot with no loads. On the other hand, when the excitation delay approaches the time of arrival, the loads are no longer *transparent*. Thus, the elements interfere constructively at $0.5f_0$ and destructively at f_0 . These constructive and destructive interferences corresponds to impedance maximas and minimas respectively.

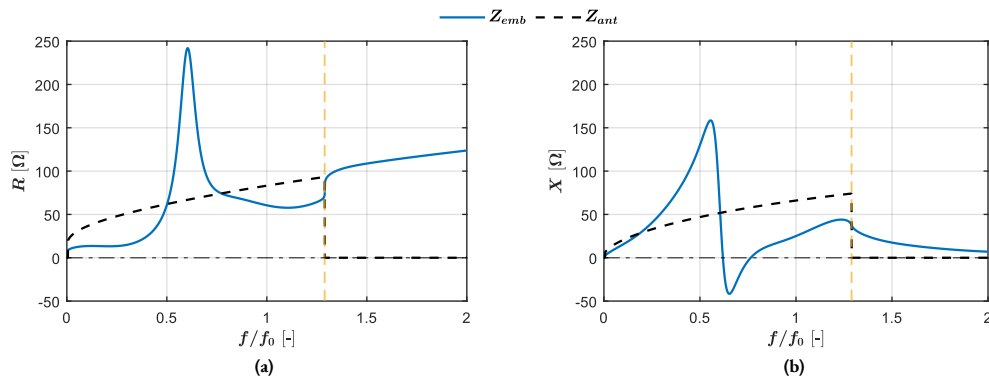


Figure 4.8: Embedded impedance for $\Delta_x = 25 \mu m$ and $\Delta_\tau = 0 ps$ of the photo-conductive antenna loaded by two unbiased photo-conductive loads (the dashed black line is the impedance of unloaded antenna, and the yellow dashed line is the narrow-slot approximation maximum frequency); in (a) the resistance, and in (b) reactance.

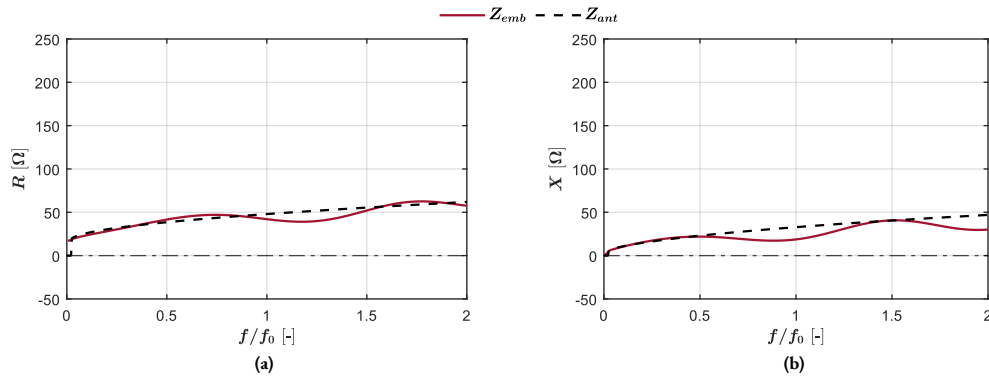


Figure 4.9: Embedded impedance for $\Delta_x = 100 \mu m$ and $\Delta_\tau = 0 ps$ of the photo-conductive antenna loaded by two unbiased photo-conductive loads (the dashed black line is the impedance of unloaded antenna); in (a) the resistance, and in (b) reactance.

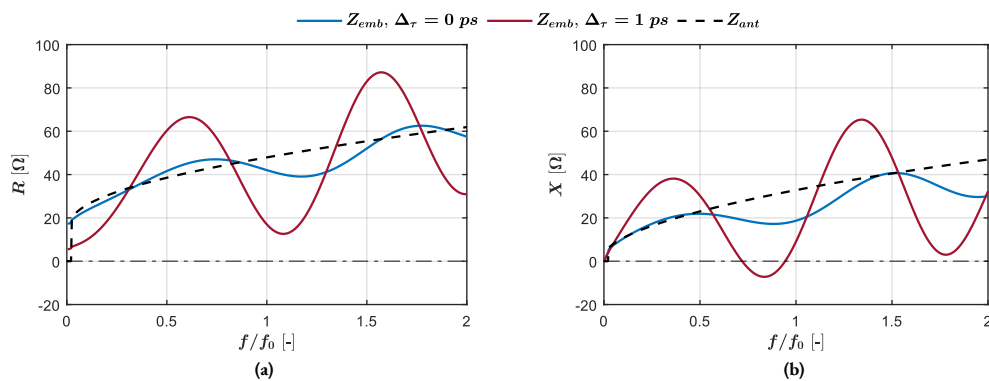


Figure 4.10: Embedded impedance for different Δ_τ and $\Delta_x = 100 \mu m$ of the photo-conductive antenna loaded by two unbiased photo-conductive loads (the dashed black line is the impedance of unloaded antenna); in (a) the resistance, and in (b) reactance.

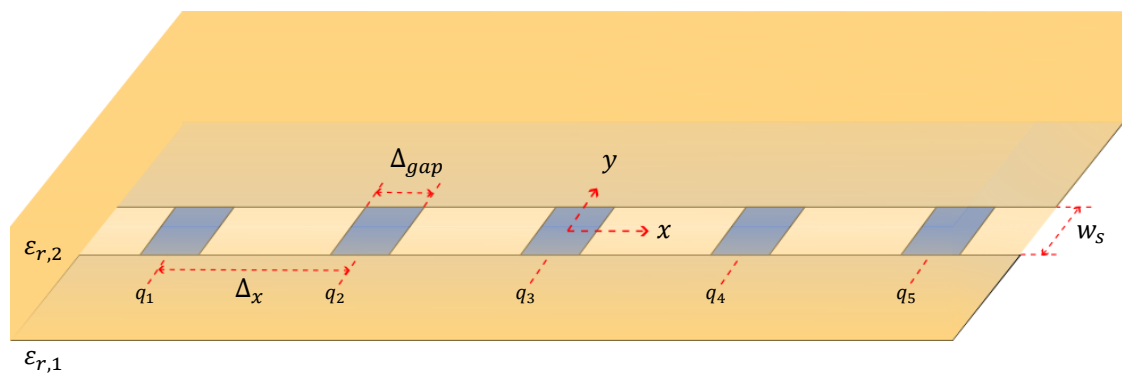


Figure 4.11: 5-element 1D photo-conductive connected array between two homogeneous dielectrics.

4.3. Magnetic Currents

As previously defined in Eq.4.1, the total excitation is the superposition of all individual feed excitations. Therefore, the total *spectral* longitudinal magnetic current is

$$V(k_x) = I_e(k_x) \frac{\text{sinc}(k_x \frac{\Delta_{gap}}{2})}{D(k_x)}, \quad (4.9)$$

while the transverse component $M_t(k_y)$ remains the previously discussed edge-singular function in the spatial domain corresponding to a zero-order Bessel function in the spectral domain. Therefore, the spatial longitudinal magnetic current becomes

$$v_x = \frac{1}{2\pi} \int_{-\infty}^{\infty} I_e(k_x) \frac{\text{sinc}(\frac{\Delta_{gap}}{2} k_x)}{D(k_x)} e^{-jk_x x} dk_x. \quad (4.10)$$

The longitudinal magnetic currents are studied for simultaneously and progressively excited 5-element 1D PCCA shown in Fig.4.11.

4.3.1. Simultaneous Excitation

The magnetic currents are plotted in Fig.4.12 for simultaneous feed excitation. The x -coordinate is normalized to the effective wavelength of the investigated frequency. For $f = 0.2f_0$ in Fig.4.12(a), the distance between the edge elements is small with significant magnetic currents after the edge elements. Thus, the dominant radiation mechanism is expected to be the LW mode. In Fig.4.12(b), the edge-to-edge distance is no longer small. There is concentration of magnetic currents at the origin, and after the edge elements. Consequently, the space and LW modes are both dominant radiation mechanism. Finally, for $f = f_0$ in Fig.4.12(c), the wave components from each feed interfere destructively resulting in lower radiated power.

4.3.2. Progressive Excitation

In [21], a distributed excitation of photo-conductive feeds is proposed, in which the feeds are successively excited as the wave arrives. These structures result in high losses due to the high mutual coupling as seen in Chapter.4.2.2. However, they provide a method to reinforce the LW beam in the direction of excitation. With this point in mind, the excitation delay is defined as

$$\Delta\tau = \tau_{e.,q+1} - \tau_{e.,q}. \quad (4.11)$$

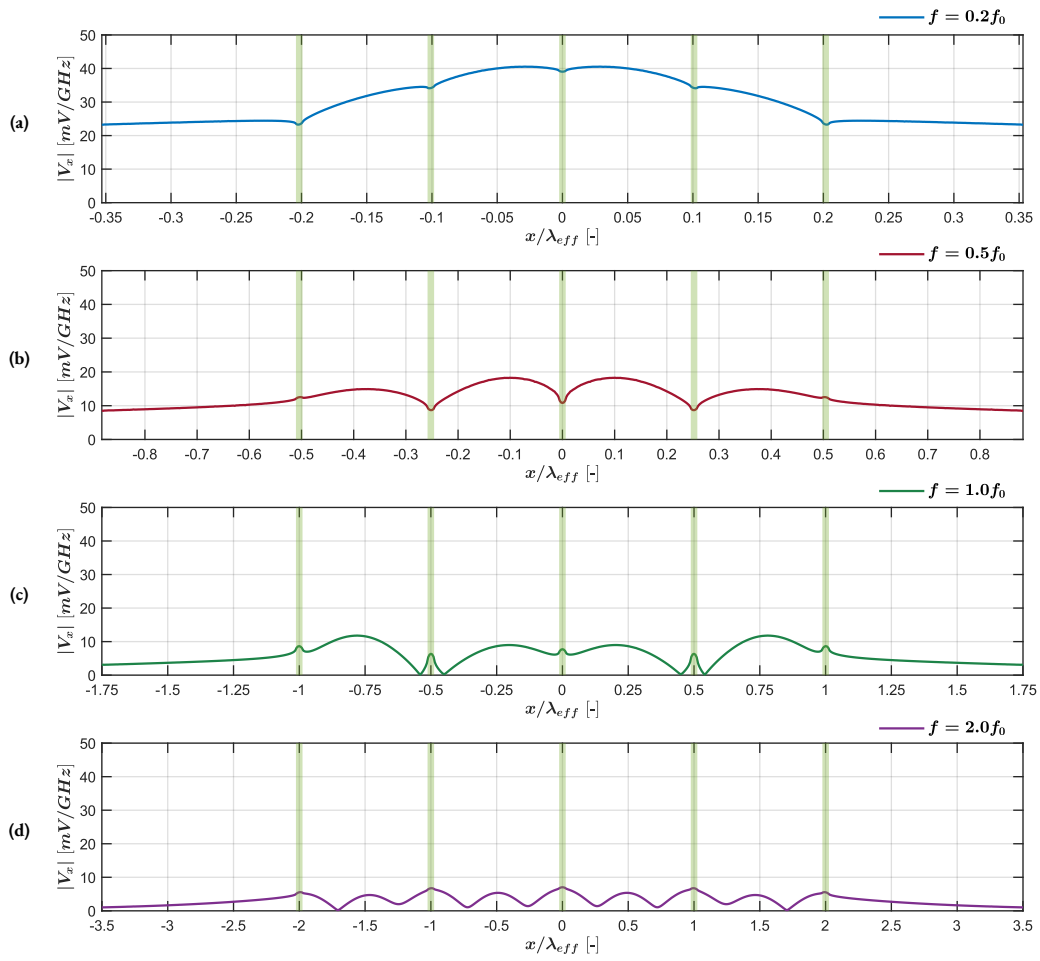


Figure 4.12: Longitudinal magnetic currents of the 5-element simultaneously excited array with element spacing $\Delta_x = 100 \mu m$; in (a) $f = 0.2f_0$, in (b) $f = 0.5f_0$, in (c) $f = f_0$, and in (d) $f = 2f_0$.

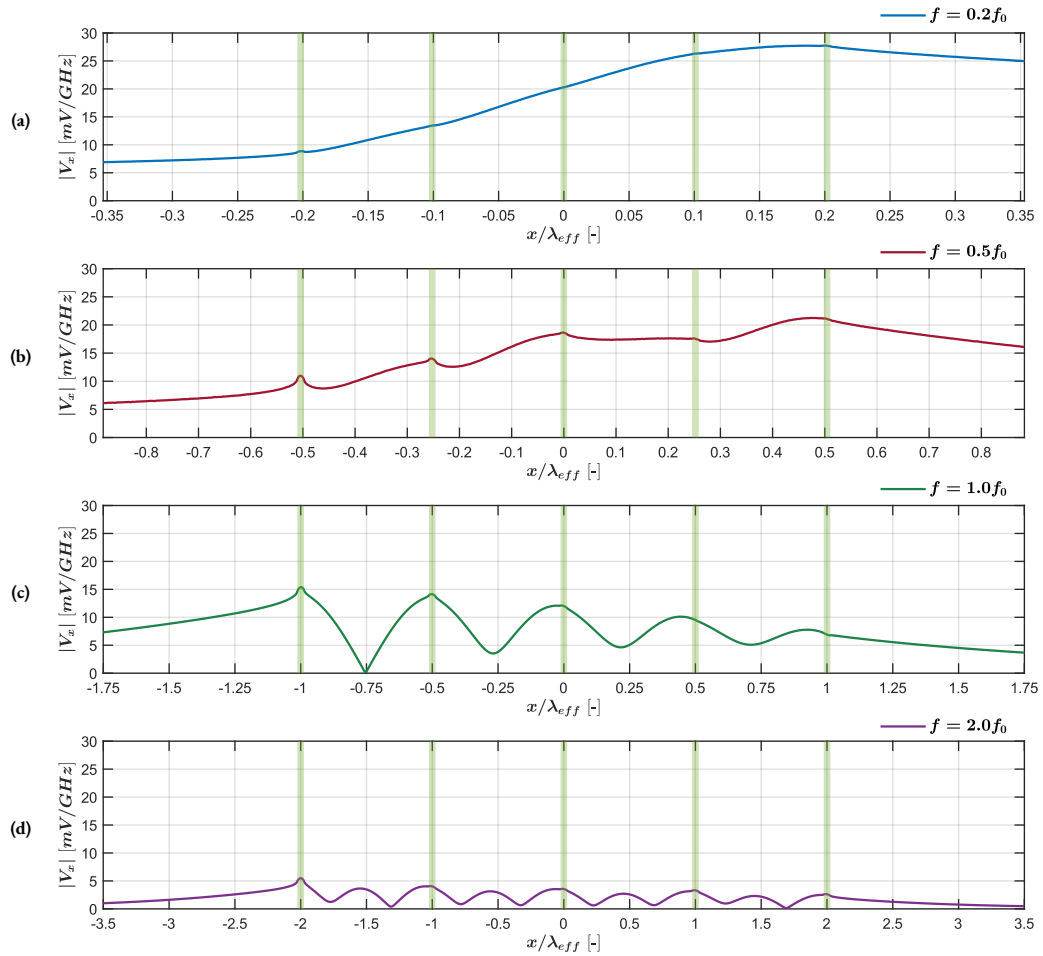


Figure 4.13: Longitudinal magnetic currents of the 5-element progressively excited array with element spacing $\Delta_x = 100 \mu m$; in (a) $f = 0.2f_0$, in (b) $f = 0.5f_0$, in (c) $f = f_0$, and in (d) $f = 2f_0$.

The magnetic currents of the 5 element progressively excited array are plotted in Fig.4.13. Evidently, below $f \leq 0.5f_0$, the wave adds constructively at the feeds reinforcing the magnetic currents in the direction of successive excitation. On the other hand, destructive interference appears for $f = f_0$. Consequently, the magnetic currents in the successive excitation direction are lower than in the opposite direction.

4.4. Far-Field

Similarly to the infinite LW slot analysis, the far-field is evaluated with Eq.3.13 - spectral convolution of $\tilde{\mathbf{G}}^{\text{EM}}(k_x, k_y)$ and $\vec{M}(k_x, k_y) = V(k_x)M_t(k_y)\hat{x}$ at the stationary phase point. In contrast to the infinite slot where the main mode is the LW, in connected arrays the space wave (SW) is expected to be dominant [28].

The far-fields of the 5-element (shown in Fig.4.11) and a 10-element 1D PCCA are compared. All feeds are excited by an optical pulse with $\tilde{P}_{opt,q} = \tilde{P}_{opt} = 50 \text{ mW}$, and are biased with $V_{b,q} = V_b = 30 \text{ V}$ for $\forall q$. The element spacing is $\Delta_x = 100 \mu\text{m}$. Thus, the cut-off frequency is $f_0 \simeq 594 \text{ GHz}$.

4.4.1. Grating Lobes

The array is a periodic structure. As such, more than one maxima beam can occur in either dielectric when the element spacing is larger than the wavelength (in this dielectric). The secondary (other than the main) maxima beams are known as grating lobes [29][10][31]. This behavior is enforced by the Poisson summation and is analogous to aliasing in the DFT - spectrum folding when the sampling period is less than twice the bandwidth. Therefore, grating lobes in the i medium are expected after

$$f_{GL} = \frac{c_0}{\Delta_x \sqrt{\epsilon_{r,i}}}. \quad (4.12)$$

For an element spacing $\Delta_x = 100 \mu\text{m}$, the grating lobe frequency in the higher density medium is $f_{GL} \simeq 876 \text{ GHz}$.

4.4.2. Simultaneous Excitation

The electric far-field in the higher permittivity $i = 2$ medium is plotted in Fig.4.14 for simultaneously excited feeds. First, the 10-element array has higher gain and around 3 dB more directivity than the 5-element. Second, grating lobes are observed for $f \geq f_{GL}$ in Fig.4.14(d-e). However, secondary maximas are also observed in Fig.4.14(b-c). These beams are not grating lobes, but are associated to the LW mode. In fact, the LW arises due to the slot propagating wave after the edge elements seen in Fig.4.12. Finally, at low frequencies and for small arrays, the far-field approximates the one radiated by an infinite LW slot as observed in Fig.4.14(a). This behavior is caused by the small edge-to-edge element distance (in terms of the wavelength). In essence, the wave sees the feeds as one element resulting in a dominant LW mode.

4.4.3. Progressive Excitation

The far-field is plotted in Fig.4.15 for progressively excited feeds. Evidently, the LW beam in the direction of successive excitation is reinforced for frequency below $f = 0.2f_0$ and $f = 0.5f_0$ as seen in Fig.4.15(a-b). The beam in the opposite direction is decreased due to destructive interference. However, at $f = f_0$, destructive addition occurs at each successive feed. Therefore, the beam in the successive excitation direction is no longer constructively reinforced as observed in Fig.4.15(c). In fact, the beam in the opposite direction has negligibly higher magnitude. Finally, similarly to the simultaneously excited array, grating lobes are observed in Fig.4.15(d-e). The two LW beams have comparatively the same magnitude in Fig.4.15(e) due to the same mechanism as for $f = f_0$ and periodicity f_0 .

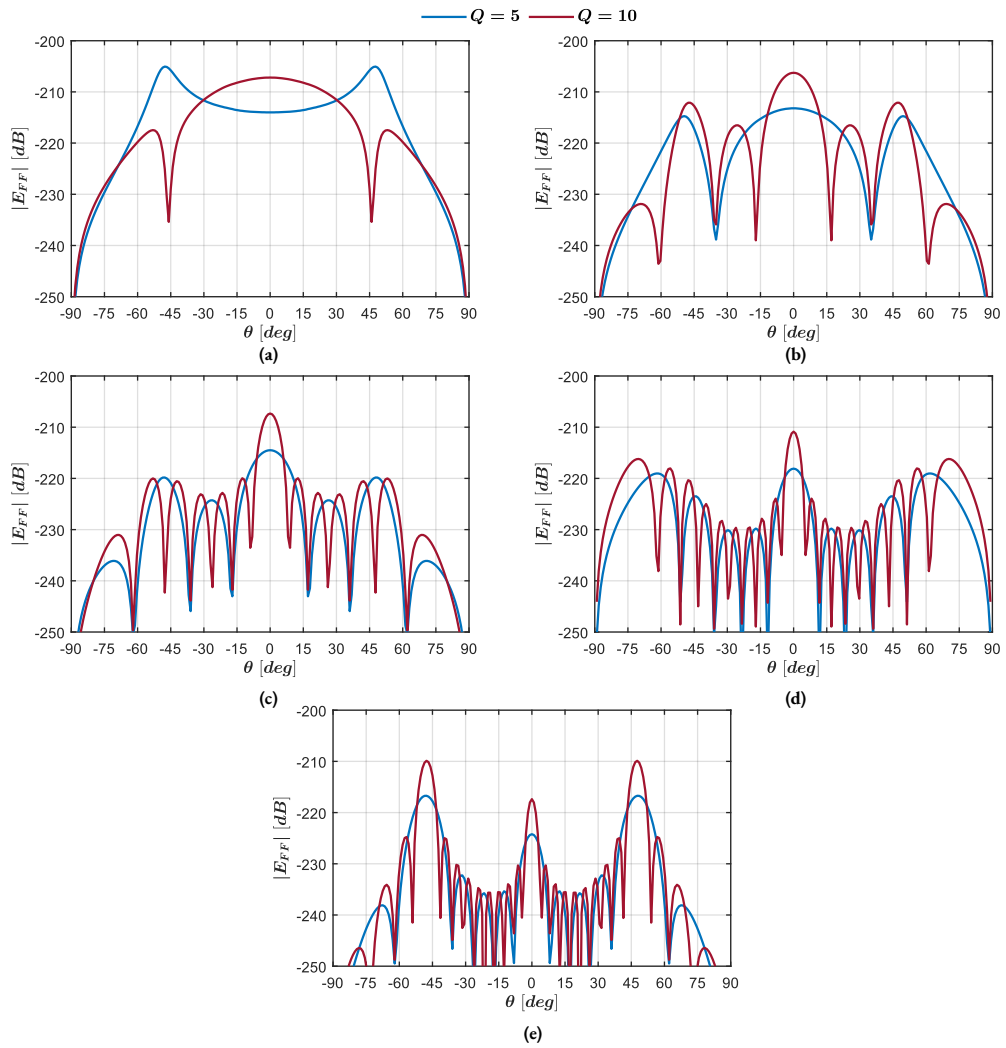


Figure 4.14: Electric far-field of 5 and 10 element simultaneously excited arrays with element spacing $\Delta_x = 100 \mu\text{m}$; in (a) $f = 0.2f_0$, in (b) $f = 0.5f_0$, in (c) $f = f_0$, in (d) $f = 1.5f_0$, and in (e) $f = 2f_0$.

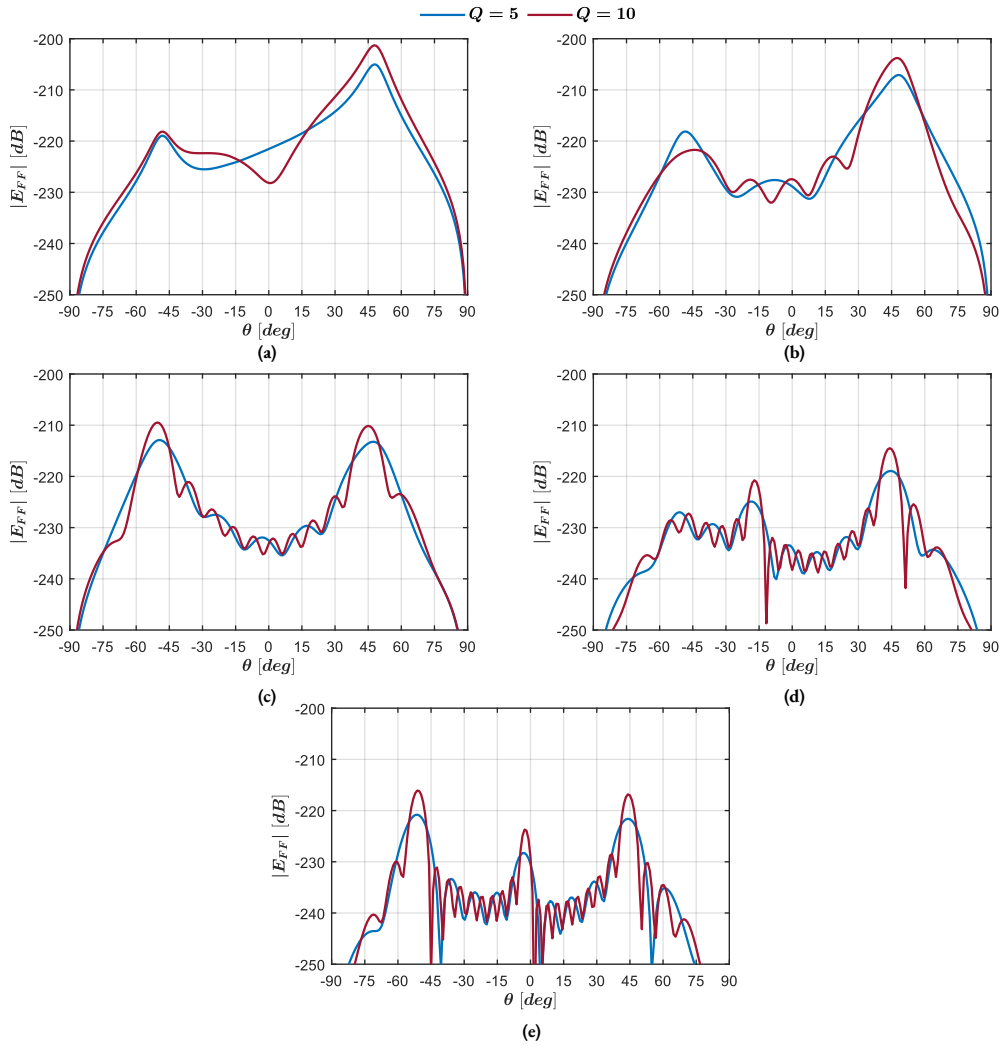


Figure 4.15: Electric far-field of 5 and 10 element progressively excited arrays with element spacing $\Delta_x = 100 \mu m$; in (a) $f = 0.2f_0$, in (b) $f = 0.5f_0$, in (c) $f = f_0$, in (d) $f = 1.5f_0$, and in (e) $f = 2f_0$.

4.5. Active Impedance

The active impedance is analogous to the embedded in the mutual coupling study. In other words, the impedance seen from feed q is defined as active

$$Z_{act,q} = \frac{V_q}{I_q}. \quad (4.13)$$

The active impedance of the 5-element simultaneously excited array is plotted in Fig.4.16. The frequency is normalized to f_0 . First, the symmetric feeds with respect to the origin have the same impedance, i.e. the impedance at the edge element $q = 1$ equals the one at the other edge element $q = 5$, and at element $q = 2$ to $q = 4$.

Second, drops (or minimas) in the impedance are observed (marked with magenta). These drops correspond to less radiated power [29][10]. The number of minimas corresponds to the number of unique distances between feeds. For example, the central feed interacts with elements located at $100 \mu m$ and $200 \mu m$, thus 2 minimas are expected and observed. On the other hand, the edge feeds interact with elements at 4 different distance, thus 4 minimas are observed. The drops coinciding to larger distances are smaller in magnitude, because elements at larger distance are less coupled. Further, these drops should correspond to multiples of the cut-off frequency f_0 . However, in large array structures, the interactions between the feeds' wave components is more complex; as a result, the impedance drops shift. In fact, for a 3-element structure, the minimas are approximately at f_0 as seen in Fig.4.10.

Third, in the internal feeds, some of the minimas correspond to negative impedance. Essentially, at these frequencies more power is induced (at the feed) than supplied (to the slot). However, the total power in the slot (at these frequencies) is still positive, i.e. no negative net balance. Thus, as expected, all of the power is supplied by the feeds. Finally, the active impedance is initially capacitive, then inductive. This behavior is similar to the one observed in [28].

4.6. Power Spectral Density

To validate the previous observations, the power spectral density (PSD) at the feeds is studied. To that end, the PSD at feed q is

$$P_q = \frac{1}{2} \Re\{V_q I_q^*\}. \quad (4.14)$$

Therefore, the total radiated PSD (assuming no ground plane losses) is simply the sum of the feed PSDs

$$P = \sum_{q=1}^Q P_q. \quad (4.15)$$

The feed PSD of the 5-element simultaneously excited array is plotted in Fig.4.17. First, the symmetric feeds (with respect to the origin) have the same PSD. This behavior is similar to and expected from the active impedance results. Second, the active impedance minimas indeed correspond to drops in the radiated power. In addition, the negative active impedance correlates to induced power from the slot to the feed.

The total radiated PSD is plotted in Fig.4.18. The total power net balance is positive satisfying the energy conservation - power is solely supplied by the feeds. As a final remark, the array works well below $0.5f_0$, but has a significant decrease in performance above this frequency.

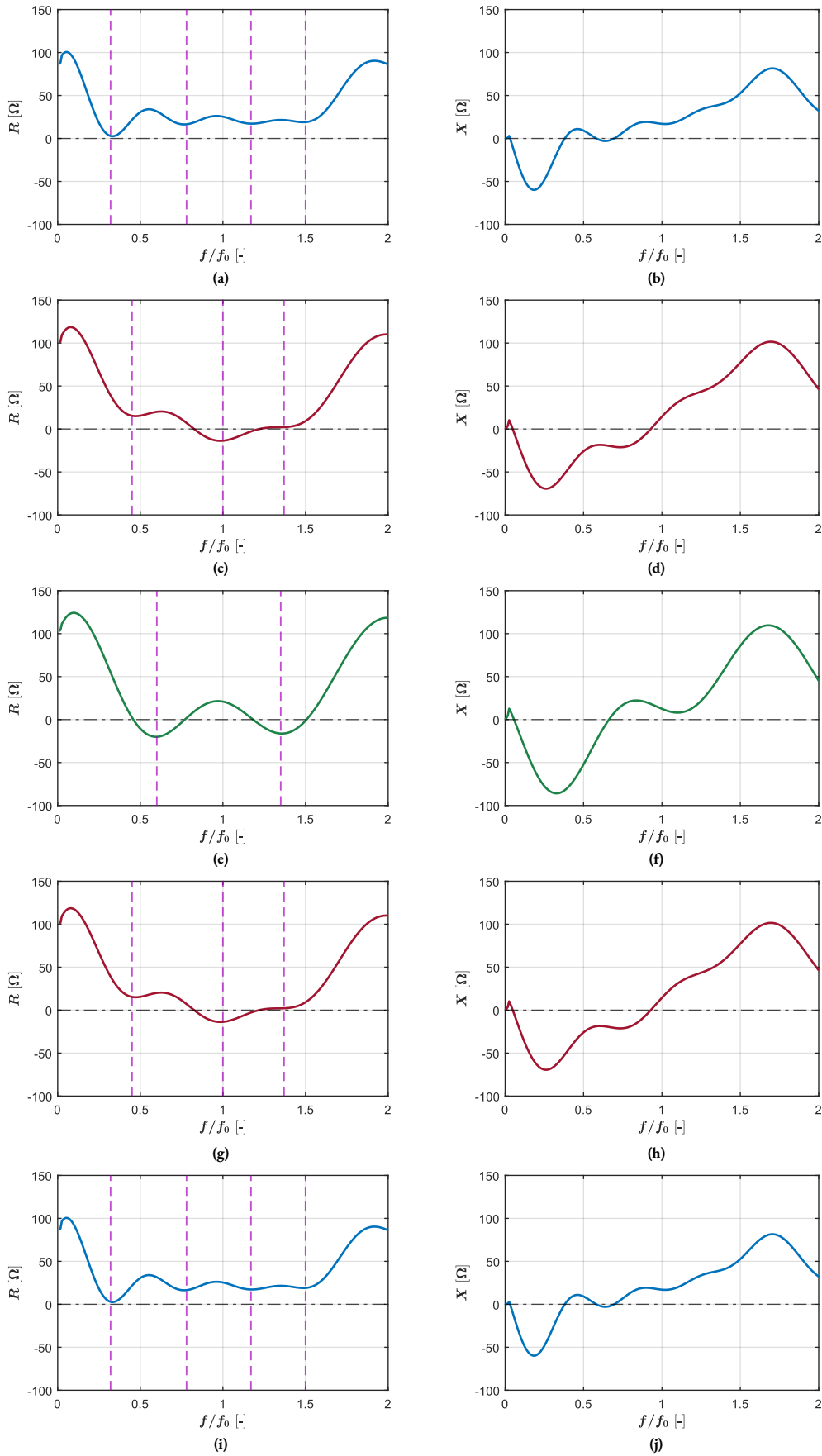


Figure 4.16: Active impedance of the 5-element simultaneously excited array (drops in the resistance are marked with dashed magenta lines); in (a-b) the resistance and reactance of edge element $q = 1$, in (c-d) of element $q = 2$, in (e-f) of center element $q = 3$, in (g-h) of element $q = 4$, and in (i-j) of edge element $q = 5$.

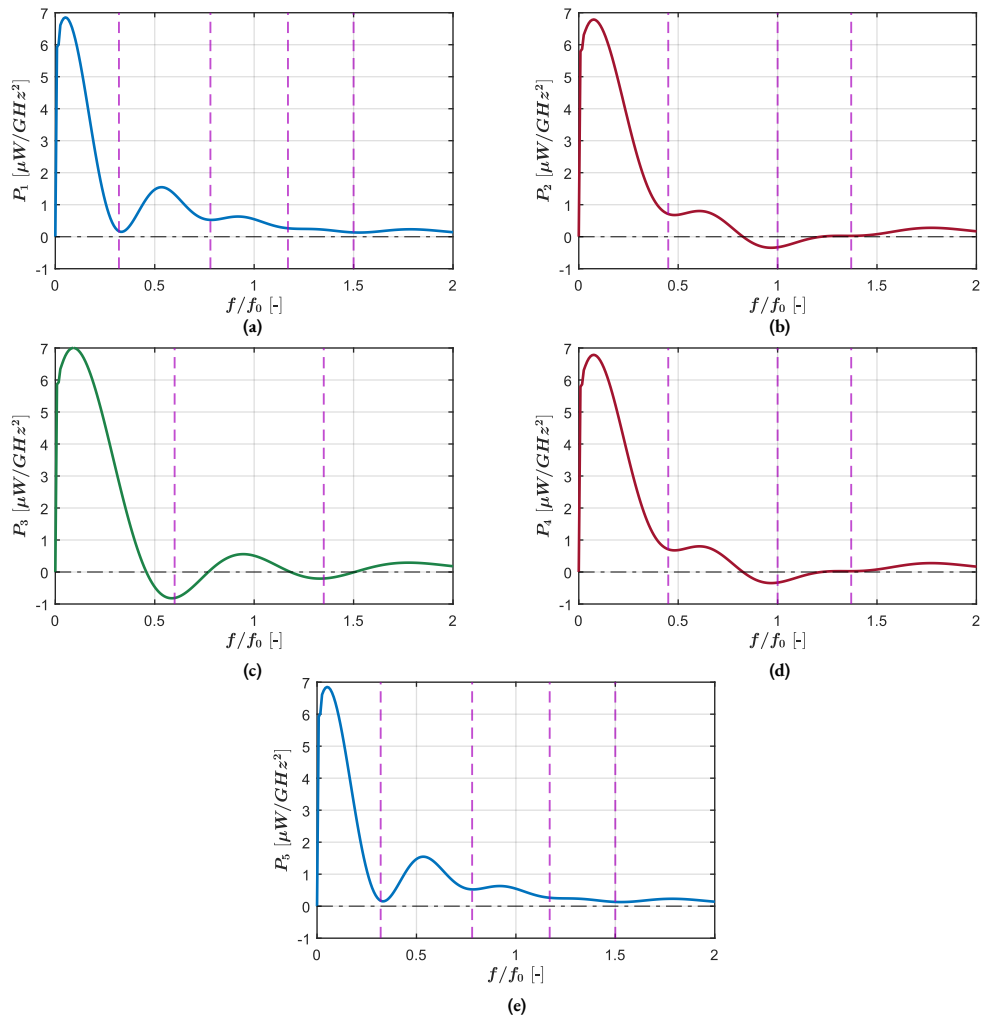


Figure 4.17: Power spectral density of the 5-element simultaneously excited array (drops in the power are marked with dashed magenta lines); in (a) at edge element $q = 1$, in (b) at element $q = 2$, in (c) at center element $q = 3$, in (d) at element $q = 4$, and in (e) at edge element $q = 5$.

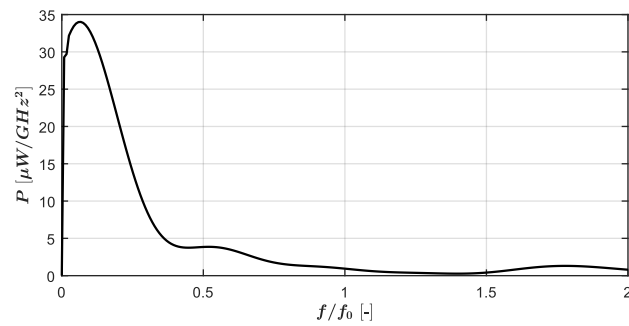


Figure 4.18: Total power spectral density of the 5-element simultaneously excited array.

Chapter 5.

Conclusion

To design a more dispersive and efficient photo-conductive antennas (PCAs), an equivalent circuit tool is required. In the past, a frequency-domain circuit was proposed, but it does not represent well the PCA behavior over the whole spectrum. This inability arises from the non-linear differential equation governing the current's time evolution. Time-domain circuits were also proposed, but they required a posteriori parameter calibration making them unsuitable for use during design. Fortunately, a new time-domain Norton equivalent circuit that does not require parameter calibration was proposed recently. Needless to say, the circuit requires knowledge of the antenna impedance impulse response. Unfortunately, there is no time-domain analytical expression for the impulse response of the studied antenna structures - the infinite leaky-wave (LW) slot and 1D connected array. Consequently, spectral analysis is used to determine the antenna impedance in the frequency-domain. The impedance impulse response is then recovered with the inverse Fourier transform (IFT). The time-domain response is used in a time-step algorithm to evaluate the voltage and current across the photo-conductive feed. This algorithm is derived through numerical methods, more specifically by representing the voltage and current as sum of rectangular basis functions. Although this time-step procedure was proposed previously, its properties were never studied. Moreover, the algorithm was never used in the analysis of the infinite LW slot and 1D connected array.

The thesis provides a derivation of a time-step algorithm using directly the antenna impedance impulse response. This algorithm showed poor performance. The performance issue is proved to be caused by the Gibbs oscillations arising from the frequency-domain impedance discontinuity at the narrow-slot approximation limit. The performance is significantly improved by using a weight function to decrease these discontinuities. A brief study showed that the best performing weight function is the one proposed in previous work - squared antenna admittance. Moreover, detailed characterization of the weight time-step algorithm is conducted. In fact, during the span of this work, an additional numerical error in the algorithm's outputs was discovered. The observed error is smaller in antennas with smaller feeds. Its source is identified as the DC singularity in the antenna admittance. Error minimization is achieved by truncating the weight function from DC to a minimum evaluated frequency. Increasing the minimum frequency decreases the voltage and power error. On the other hand, the energy error is decreased until a certain point. After this point, the time-domain impulse responses are altered significantly re-introducing error. Unfortunately, analytical expression for the minimum frequency is not derived due to the non-linearities. Next, the error analysis is extended to 1D connected arrays, in which the self and mutual-impedance are multiplied with the same weight function. Unfortunately, the spectral content distribution of the mutual impedance limits the error minimization. In other words, the numerical error cannot be sufficiently minimized in large arrays.

As a next step, a comprehensive analysis of the infinite LW slot is performed. At its start, a novel time-domain energy balance equation is derived using a switched capacitor formalism for the photo-conductive feed. This new equation is verified by comparing the far-field and time-domain energy. Further, a comparison between the fully dispersive approximation and the newly enabled dispersive analysis is conducted. The comparison shows that the dispersive approximation overestimates the radiated power at low frequencies and in the spectrum's tail. Next, procedures to evaluate the magnetic currents and far-fields in frequency and time-domain are discussed. Using these procedures, the radiated energy, efficiency, and bandwidth of the PCA are characterized with respect to the absorbed optical power, bias voltage, laser's full width at half maximum (FWHM), and recombination time. The results show that the optical power should be chosen at the saturation point and bias close to the photo-conductor's breakdown voltage to maximize the

radiated power and antenna efficiency. Additionally, higher recombination times move the power to lower frequencies. For FWHM much shorter than the recombination time, increasing the FWHM only reduces the power in the spectrum's tail due to increasing internal to antenna load mismatch.

To complete the overall study, the 1D photo-conductive connected array (PCCA) is analyzed. Initially, the energy balance equation is extended to multiple feeds and verified as before. During this verification, it is shown that the radiated energy relation to the optical power and bias is the same as in the infinite LW slot. However, as expected, more power is radiated due to the higher number of feeds. This radiated power might not equal the number of feeds multiplied by the power of a single feed infinite slot due to mutual coupling. Therefore, the mutual coupling is investigated to provide improve the PCCA design. With this point in mind, closely spaced elements have high mutual coupling increasing the dissipated power and reducing efficiency. In addition, successively excited elements also have high mutual coupling. The embedded impedance confirms the previous mutual coupling observations. Next, the far-fields of simultaneously excited arrays show mostly a dominant space wave (SW) with a less dominant LW mode below the grating lobe frequency. However, for small arrays, at low frequencies the dominant mode is the LW due to the short edge-to-edge element distance in terms of the wavelength. Additionally, the LW beam reinforcing behavior of progressively excited arrays is verified. Finally, the active impedance and power spectral density are studied. The results show good performance below half cut-off frequency, but significantly reduced performance above.

All things considered, if more optical power is available than needed to saturate a single feed, the laser excitation should be divided to multiple feeds. Exciting the photo-conductor at the saturation point provides the best efficiency with respect to used optical power. Moreover, a bias voltage near the photo-conductor's breakdown voltage maximizes the radiated power. The cut-off frequency's half point should be chosen slightly above the required bandwidth. Ultimately, decreasing the element spacing increases the cut-off frequency, however, it also increases the mutual coupling and associated dissipation losses - a trade-off that should be considered. Larger recombination time increases the radiated power, but greatly reduces the bandwidth. The FWHM should be chosen as short as possible to improve the matching at the spectrum's tail. On the other hand, the spectrum's main part is not influence by the FWHM, if it is much shorter than the recombination time.

5.1. Future Work

The discovered numerical error is a significant limitation to the algorithm's performance and PCA analysis. Although the proposed error minimization procedure works well for the infinite LW slot, it is impeded by the mutual impedance in the PCCA analysis. Therefore, useful future research points concern improving the algorithm's performance, and include:

- detailed investigation on more weight functions. The brief study provided in this thesis investigates functions that do not alter the impedance phase, i.e. purely real functions. However, the squared admittance does contribute to a phase change, and overall works well. Consequently, it is worth investigating the performance of not purely real weights.
- investigation on different weights for the self and mutual impedance. The spectral content distribution of the mutual impedance limits the algorithm's performance when the same weight is used. Thus, it is useful to investigate the feasibility and performance of an algorithm with different self and mutual weights.
- separating large feeds to smaller components. The error significantly decreases in feeds with smaller length. Although it might be undesirable to use smaller feeds in the design, this advantage can still be used in the design phase. Hence, it is beneficial to investigate the feasibility and performance when a large feed is described as the superposition of many smaller feeds next to each other.
- simulating the impedance using a full-wave simulator. The used analytical expression is limited to the maximum frequency at which the quasi-TEM mode is dominant. Using a full-wave simulator, the contributions of all modes

are considered. Although it is unfeasible to simulate the impedance over all frequencies, it might be simulated until the Nyquist frequency. In this case, it is expected that there will be no discontinuity. Yet, it must be mentioned that the higher frequencies folded onto the spectrum will not be included.

- deriving analytical expression for higher order modes. Similarly, the impedance at higher frequencies can also be estimated by deriving an analytical solution for the higher order modes.
- analytical expression for the antenna impulse response. The strength of the algorithm comes from a good knowledge of the time-domain antenna impulse response. Consequently, it is useful to derive a time-domain analytical solution for the response.

A detailed analysis of the photo-conductive infinite slot is provided. However, this study can be complemented by:

- extending the analysis to air cavity enhanced structures. In reality, PCAs are enhanced through a LW air cavity. Thus, it is useful to expand the analysis to include these structures.
- extending the analysis to a PCA with a lens. Similarly as the air cavity, PCAs are used with lenses to improve the directivity. Hence, it is also useful to expand the analysis to include a lens.
- comparing the analysis results to measurements. To verify the validity and performance of this analysis with respect to the constant impedance approximation, the estimated radiated power should be compared to measurements.

For 1D connected arrays, studies on the radiated power, mutual coupling, far-fields, and array performance are performed. This analysis can be further extended by:

- including air cavity and lens. Similarly to the infinite LW slot, PCCAs are enhanced using air cavity and lens. Thus, it is useful to characterize arrays with these structures.
- comparing it to measurements. The results should be compared to measurements, in order to verify the accuracy of the established analysis.
- investigation on the recombination time's influence on the mutual coupling. Longer recombination times should result in higher mutual coupling due to the longer time-domain current response. Therefore, it is beneficial to investigate its influence on the mutual coupling.
- considering 2D structures. As a groundwork, 1D array is studied. However, in reality, PCCAs are designed as 2D structures. Hence, the analysis should be expanded to 2D arrays.

Chapter A.

Discretized FT, IFT, & Convolution

A general Fourier transform (FT) pair discretized with rectangular basis functions in both domains is defined as

$$x(t) = \sum_{n=-\infty}^{\infty} x_n \text{rect}_{\Delta_t}(t - t_n), \quad (\text{A.1a})$$

$$X(f) = \sum_{k=-\infty}^{\infty} X_k \text{rect}_{\Delta_f}(f - f_k). \quad (\text{A.1b})$$

A.1. Fourier Transform

Substituting the time-domain representation in the Fourier transform gives

$$X(f) = \int_{-\infty}^{\infty} x(t) e^{-j2\pi ft} dt = \int_{-\infty}^{\infty} \sum_{n=-\infty}^{\infty} x_n \text{rect}_{\Delta_t}(t - t_n) e^{-j2\pi ft} dt. \quad (\text{A.2})$$

The n -th basis function is constant and bounded to $t_n - \Delta_t/2 \leq t \leq t_n + \Delta_t/2$, thus

$$X(f) = \sum_{n=-\infty}^{\infty} x_n \int_{t_n - \Delta_t/2}^{t_n + \Delta_t/2} e^{-j2\pi ft} dt = \sum_{n=-\infty}^{\infty} x_n e^{-j2\pi f t_n} \Delta_t. \quad (\text{A.3})$$

Both domains are discretized, and hence are periodic - the opposite domain is periodic due to Poisson summation. That is to say, the frequency-domain is periodic because the function is discrete in time, and vice versa. Therefore, both domains have periodicity of N -samples (the domains have equal number of samples), as such

$$X_k = \Delta_t \sum_{n=0}^{N-1} x_n e^{-j2\pi f_k t_n}. \quad (\text{A.4})$$

The frequency and time samples are $f_k = k/N\Delta_t$ and $t_n = t_0 + n\Delta_t$ respectively, therefore

$$X_k = \Delta_t \sum_{n=0}^{N-1} x_n e^{-j2\pi \frac{k}{N\Delta_t} (t_0 + n\Delta_t)} = \Delta_t e^{-j2\pi f_k t_0} \sum_{n=0}^{N-1} x_n e^{-j2\pi \frac{k}{N} n}, \quad (\text{A.5})$$

where the discrete Fourier transform is recognized

$$X_k = \Delta_t e^{-j2\pi f_k t_0} \text{DFT}\{x\}. \quad (\text{A.6})$$

A.2. Inverse Fourier Transform

Substituting the frequency-domain representation in the inverse Fourier transform gives

$$x(t) = \int_{-\infty}^{\infty} X(f)e^{j2\pi ft} df = \int_{-\infty}^{\infty} \sum_{k=-\infty}^{\infty} X_k \text{rect}_{\Delta_f}(f - f_k) e^{j2\pi ft} df. \quad (\text{A.7})$$

Again, the k -th basis function is constant and bounded to $f_k - \Delta_f/2 \leq f \leq f_k + \Delta_f/2$

$$x(t) = \sum_{k=-\infty}^{\infty} X_k \int_{f_k - \Delta_f/2}^{f_k + \Delta_f/2} e^{j2\pi f_k t} df = \sum_{k=-\infty}^{\infty} X_k e^{j2\pi f_k t} \Delta_f. \quad (\text{A.8})$$

Considering the periodicity of both domains, the inverse Fourier transform is represented as

$$x_n = \Delta_f \sum_{k=-0}^{N-1} X_k e^{j2\pi f_k t_n}. \quad (\text{A.9})$$

The frequency and time samples are $f_k = k/N\Delta_t$ and $t_n = t_0 + n\Delta_t$ respectively, therefore

$$x_n = \Delta_f \sum_{k=-0}^{N-1} X_k e^{j2\pi \frac{k}{N\Delta_t}(t_0 + n\Delta_t)} = \Delta_f \sum_{k=-0}^{N-1} X_k e^{j2\pi f_k t_0} e^{j2\pi \frac{k}{N} n}. \quad (\text{A.10})$$

The frequency-step is $\Delta_f = 1/N\Delta_t$, consequently

$$x_n = \frac{1}{N\Delta_t} \sum_{k=-0}^{N-1} X_k e^{j2\pi f_k t_0} e^{j2\pi \frac{k}{N} n} = \frac{1}{\Delta_t} \text{IDFT}\{X_k e^{j2\pi f_k t_0}\}, \quad (\text{A.11})$$

where the inverse discrete Fourier transform is recognized.

A.3. Convolution

Substituting the time-domain representation in the continuous time convolution

$$(x * h)(t) = \int_{-\infty}^{\infty} x(t')h(t - t')dt' = \int_{-\infty}^{\infty} \sum_{n=-\infty}^{\infty} x_n \text{rect}_{\Delta_t}(t' - t_n)h(t - t')dt' \quad (\text{A.12})$$

Similarly to before, the n -th basis function is constant and bounded to $t_n - \Delta_t/2 \leq t \leq t_n + \Delta_t/2$, while the convolution is evaluated at time $t = t_m$

$$(x * h)(t_m) = \sum_{n=-\infty}^{\infty} x_n \int_{t_n - \Delta_t/2}^{t_n + \Delta_t/2} \text{rect}_{\Delta_t}(t' - t_n)h(t_m - t')dt' = \sum_{n=-\infty}^{\infty} x_n h(t_m - t_n) \Delta_t. \quad (\text{A.13})$$

Therefore, the discrete-time convolution is

$$(x * h)(t_m) = \Delta_t \sum_{n=-\infty}^{\infty} x_n h_{m-n}. \quad (\text{A.14})$$

Chapter B.

Derivations of Time-Step Algorithms

The update rule for the antenna load current's time evolution is the same for every algorithm. As such, it is useful to derive it first. The time evolution is

$$i(t) = A \frac{q_e^2}{m_e} \frac{\Delta_{gap} w_z}{w_s} \int_{-\infty}^t e^{-\frac{1}{2} \left(\frac{t'' - \tau_e}{\sigma_t} \right)^2} e^{-\frac{t-t''}{\tau_{rec}}} \int_{t''}^t v_{gap}(t') e^{-\frac{t-t'}{\tau_s}} dt' dt'' \quad (\text{B.1})$$

as a response to an optical excitation at time τ_e . The parameter A is the distribution amplitude of the electron density (released electrons number) in a unit of volume during one laser pulse

$$A = \frac{\tilde{P}_{opt}}{h f_c} \frac{T}{\sqrt{2\pi\sigma_t^2}} \frac{1}{\Delta_{gap} w_s w_z} \quad (\text{B.2})$$

with a unit of $1/m^3 s$. The time-discretized current is

$$i_n = A \frac{q_e^2}{m_e} \frac{\Delta_{gap} w_z}{w_s} \Delta_t^2 \sum_{m=N_i}^n e^{-\frac{1}{2} \left(\frac{t_m - \tau_e}{\sigma_t} \right)^2} e^{-\frac{t_n - t_m}{\tau_{rec}}} \sum_{q=m}^n v_{gap,(q)} e^{-\frac{t_n - t_m}{\tau_s}}, \quad (\text{B.3})$$

in which the double sum property

$$\sum_{m=N_i}^n a_m \sum_{q=m}^n b_q = \sum_{m=N_i}^{n-1} a_m \sum_{q=m}^{n-1} b_q + b_n \sum_{m=N_i}^n a_m \quad (\text{B.4})$$

is applied. Therefore, after performing trivial algebraic steps, the current can be written in terms of the previous time index current as

$$i_n = e^{-\frac{\Delta_t}{\tau_{rec}}} e^{-\frac{\Delta_t}{\tau_s}} i_{n-1} + v_{gap,(n)} \Delta_t G_{pcm,(n)}, \quad (\text{B.5})$$

where the property $t_n = t_{n-1} + \Delta_t$ is used, and $G_{pcm,(n)}$ is the conductance at time t_n of the photo-conductive material

$$G_{pcm,(n)} = A \frac{q_e^2}{m_e} \frac{\Delta_{gap} w_z}{w_s} \Delta_t \sum_{m=N_i}^n e^{-\frac{1}{2} \left(\frac{t_m - \tau_e}{\sigma_t} \right)^2} e^{-\frac{t_n - t_m}{\tau_{rec}}}. \quad (\text{B.6})$$

Writing the gap voltage in terms of the bias and transient voltages results in the update rule for the current across the photo-conductive feed

$$i_n = e^{-\frac{\Delta_t}{\tau_{rec}}} e^{-\frac{\Delta_t}{\tau_s}} i_{n-1} + (V_b - v_n) \Delta_t G_{pcm,(n)}. \quad (\text{B.7})$$

For the first non-zero index, the update rule is

$$i_{N_i} = (V_b - v_{N_i}) \Delta_t G_{pcm,(N_i)}. \quad (\text{B.8})$$

B.1. Fully Dispersive Time-Step Algorithm

For a fully dispersive antenna, the voltage current relation is

$$v(t) = \int_{-\infty}^{\infty} i(t') R_{ant} \delta(t - t') dt' = R_{ant} i(t), \quad (\text{B.9})$$

For a discretized domain this relation is represented as

$$v_n = R_{ant} i_n. \quad (\text{B.10})$$

Substituting Eq.B.7 gives

$$v_n = e^{-\frac{\Delta t}{\tau_{rec}}} e^{-\frac{\Delta t}{\tau_s}} R_{ant} i_{n-1} + V_b R_{ant} \Delta t G_{pcm,(n)} - v_n R_{ant} \Delta t G_{pcm,(n)}. \quad (\text{B.11})$$

Therefore, the voltage update rule is

$$v_n = \frac{e^{-\frac{\Delta t}{\tau_{rec}}} e^{-\frac{\Delta t}{\tau_s}} i_{n-1} + \Delta t V_b G_{pcm,(n)}}{1/R_{ant} + \Delta t G_{pcm,(n)}}. \quad (\text{B.12})$$

The initial conditions are

$$v_{N_i} = \frac{\Delta t V_b G_{pcm,(N_i)}}{1/R_{ant} + \Delta t G_{pcm,(N_i)}}. \quad (\text{B.13})$$

B.2. Impedance Time-Step Algorithm

The time-domain voltage is given by the convolution of the antenna impedance impulse response and current

$$v(t) = (z_{ant} * i)(t) = \int_{-\infty}^{\infty} i(t') z_{ant}(t - t') dt'. \quad (\text{B.14})$$

Therefore the discretized-time relation is

$$v_n = \Delta t \sum_{m=-\infty}^{\infty} i_m z_{ant,(n-m)}, \quad (\text{B.15})$$

where n denotes the sample at time step t_n . Since the antenna is a causal system, and assuming the current is negligible before time step t_{N_i}

$$z_{ant,(n<0)} = 0 \text{ } \Omega/s, \quad (\text{B.16a})$$

$$i_{n<N_i} = 0 \text{ } A. \quad (\text{B.16b})$$

Applying these properties, simplifies the convolution to

$$v_n = \Delta t \sum_{m=N_i}^n z_{ant,(n-m)} i_m = \Delta t z_{ant,(0)} i_n + \Delta t \sum_{m=N_i}^{n-1} z_{ant,(n-m)} i_m. \quad (\text{B.17})$$

Finally, substituting Eq.B.7 in Eq.B.17 gives

$$v_n = e^{-\frac{\Delta t}{\tau_{rec}}} e^{-\frac{\Delta t}{\tau_s}} \Delta t z_{ant,(0)} i_{n-1} + (V_b - v_n) \Delta t^2 z_{ant,(0)} G_{pcm,(n)} + \Delta t \sum_{m=N_i}^{n-1} z_{ant,(n-m)} i_m. \quad (\text{B.18})$$

After performing trivial algebraic steps, the voltage update rule is derived as

$$v_n = \frac{e^{-\frac{\Delta t}{\tau_{rec}}} e^{-\frac{\Delta t}{\tau_s}} \Delta t z_{ant,(0)} i_{n-1} + V_b \Delta t^2 z_{ant,(0)} G_{pcm,(n)} + \Delta t C_n}{1 + \Delta t^2 z_{ant,(0)} G_{pcm,(n)}}, \quad (\text{B.19})$$

where

$$C_n = \sum_{m=N_i}^{n-1} z_{ant,(n-m)} i_m \quad (\text{B.20})$$

describes the memory effects of the antenna. For the first non-zero index, the update rule is

$$v_{N_i} = \frac{V_b \Delta t^2 z_{ant,(0)} G_{pcm,(N_i)}}{1 + \Delta t^2 z_{ant,(0)} G_{pcm,(N_i)}}, \quad (\text{B.21})$$

B.3. Admittance Time-Step Algorithm

The time-domain current is given by the convolution of the antenna admittance impulse response and voltage

$$i(t) = (y_{ant} * v)(t) = \int_{-\infty}^{\infty} v(t') y_{ant}(t - t') dt'. \quad (\text{B.22})$$

Therefore the discretized-time relation is

$$i_n = \Delta t \sum_{m=-\infty}^{\infty} v_m y_{ant,(n-m)}. \quad (\text{B.23})$$

Applying causality and zero initial conditions, the current becomes

$$i_n = \Delta t \sum_{m=N_i}^n v_m y_{ant,(n-m)} = \Delta t y_{ant,(0)} v_n + \Delta t \sum_{m=N_i}^{n-1} v_m y_{ant,(n-m)}. \quad (\text{B.24})$$

Substituting Eq.B.7, the relation is then

$$e^{-\frac{\Delta t}{\tau_{rec}}} e^{-\frac{\Delta t}{\tau_s}} i_{n-1} + (V_b - v_n) \Delta t G_{pcm,(n)} = \Delta t y_{ant,(0)} v_n + \Delta t \sum_{m=N_i}^{n-1} v_m y_{ant,(n-m)}. \quad (\text{B.25})$$

By rearranging this equation, the update rule is derived as

$$v_n = \frac{e^{-\frac{\Delta t}{\tau_{rec}}} e^{-\frac{\Delta t}{\tau_s}} i_{n-1} + \Delta t V_b G_{pcm,(n)} - \Delta t C_n}{\Delta t y_{ant,(0)} + \Delta t G_{pcm,(n)}}, \quad (\text{B.26})$$

with a first non-zero index

$$v_{N_i} = \frac{V_b}{y_{ant,(0)} / G_{pcm,(N_i)} + 1}. \quad (\text{B.27})$$

B.4. Weight Time-Step Algorithm

The voltage-current relation for an algorithm with weight function is given by

$$(w * v)(t) = (h * i)(t). \quad (\text{B.28})$$

When time-discretized, and with applied causality and zero initial conditions, the relation becomes

$$\Delta_t w_0 v_n + \Delta_t \sum_{m=N_i}^{n-1} w_{n-m} v_m = \Delta_t h_0 i_n + \Delta_t \sum_{m=N_i}^{n-1} h_{n-m} i_m. \quad (\text{B.29})$$

Rearranging the equation gives

$$w_0 v_n = h_0 i_n + C_n, \quad (\text{B.30})$$

where

$$C_n = \sum_{m=N_i}^{n-1} (h_{n-m} i_m - w_{n-m} v_m) \quad (\text{B.31})$$

describes the memory effects. Substituting Eq.B.7 in Eq.B.30 gives

$$w_0 v_n = h_0 e^{-\frac{\Delta_t}{\tau_{rec}}} e^{-\frac{\Delta_t}{\tau_s}} i_{n-1} + \Delta_t h_0 V_b G_{pcm,(n)} - \Delta_t h_0 v_n G_{pcm,(n)} + C_n. \quad (\text{B.32})$$

Therefore, the update rule is

$$v_n = \frac{e^{-\frac{\Delta_t}{\tau_{rec}}} e^{-\frac{\Delta_t}{\tau_s}} h_0 i_{n-1} + \Delta_t h_0 V_b G_{pcm,(n)} + C_n}{w_0 + \Delta_t h_0 G_{pcm,(n)}}, \quad (\text{B.33})$$

with a first non-zero index

$$v_{N_i} = \frac{\Delta_t h_0 V_b G_{pcm,(N_i)}}{w_0 + \Delta_t h_0 G_{pcm,(N_i)}}. \quad (\text{B.34})$$

B.5. Weight Algorithm for Connected Array

Extending the weight time-step algorithm to multiple feeds is taxing but trivial. The main consideration is that the relation is a matrix equation describing the interactions between the feeds. The memory effects should take these interaction into account, thus at feed q , they are described by

$$C_{q,(n)} = \sum_{m=N_i}^{n-1} (-w_{n-m} v_{q,(m)} + \sum_{p=1}^Q h_{qp,(n-m)} i_{p,(m)}). \quad (\text{B.35})$$

It can be shown that the update rule is a matrix equation

$$\mathbf{v}_n = (\mathbf{w}_0 + \Delta_t \mathbf{h}_0 \mathbf{G}_{pcm,(n)})^{-1} (e^{-\frac{\Delta_t}{\tau_{rec}}} e^{-\frac{\Delta_t}{\tau_s}} \mathbf{h}_0 \mathbf{i}_{n-1} + \Delta_t \mathbf{h}_0 \mathbf{G}_{pcm,(n)} \mathbf{V}_b + \mathbf{C}_n), \quad (\text{B.36a})$$

$$\mathbf{i}_n = e^{-\frac{\Delta_t}{\tau_{rec}}} e^{-\frac{\Delta_t}{\tau_s}} \mathbf{i}_{n-1} + (\mathbf{V}_b - \mathbf{v}_n) \Delta_t \mathbf{G}_{pcm,(n)}. \quad (\text{B.36b})$$

For the first non-zero sample, the update rules are

$$\mathbf{v}_n = (\mathbf{w}_0 + \Delta_t \mathbf{h}_0 \mathbf{G}_{pcm,(n)})^{-1} \Delta_t \mathbf{h}_0 \mathbf{G}_{pcm,(n)} \mathbf{V}_b, \quad (\text{B.37a})$$

$$\mathbf{i}_n = (\mathbf{V}_b - \mathbf{v}_n) \Delta_t \mathbf{G}_{pcm,(n)}. \quad (\text{B.37b})$$

The voltage, current, and memory effect $Q \times 1$ vectors contain the respective quantities at sample n

$$\mathbf{v}_n = \begin{bmatrix} v_{1,(n)} \\ \vdots \\ v_{Q,(n)} \end{bmatrix}, \quad \mathbf{i}_n = \begin{bmatrix} i_{1,(n)} \\ \vdots \\ i_{Q,(n)} \end{bmatrix}, \quad \text{and} \quad \mathbf{C}_n = \begin{bmatrix} C_{1,(n)} \\ \vdots \\ C_{Q,(n)} \end{bmatrix}. \quad (\text{B.38})$$

The bias voltage is constant in time and its $Q \times 1$ vector is

$$\mathbf{V}_b = \begin{bmatrix} V_{b,1} \\ \vdots \\ V_{b,Q} \end{bmatrix}. \quad (\text{B.39})$$

The photo-conductive conductance might be different at each feed depending on the excitation time, and its $Q \times Q$ matrix at sample n is diagonal (the conductance is feed specific)

$$\mathbf{G}_{pcm,(n)} = \begin{bmatrix} G_{pcm,(n)}^1 & 0 & \dots & 0 \\ 0 & G_{pcm,(n)}^2 & \dots & 0 \\ \vdots & & \ddots & \vdots \\ 0 & 0 & \dots & G_{pcm,(n)}^Q \end{bmatrix}. \quad (\text{B.40})$$

The placeholder function matrix is a $Q \times Q$ Toeplitz

$$\mathbf{h}_n = \begin{bmatrix} h_{11,(n)} & h_{12,(n)} & \dots & h_{1Q,(n)} \\ h_{21,(n)} & h_{22,(n)} & \dots & h_{2Q,(n)} \\ \vdots & & \ddots & \vdots \\ h_{Q1,(n)} & h_{Q2,(n)} & \dots & h_{QQ,(n)} \end{bmatrix}. \quad (\text{B.41})$$

Only the placeholder matrix at the first index $n = 0$ is required for the algorithm. Finally, in an algorithm using the same weight for the self and mutual impedance, the weight matrix is

$$\mathbf{w}_n = w_n \mathbf{I}, \quad (\text{B.42})$$

where \mathbf{I} is $Q \times Q$ identity matrix.

Chapter C.

Study of Weight Functions

The weight functions are chosen purely real and positive, as such, the phase of the placeholder function has the same phase as the antenna impedance

$$H = |Z_{ant}|e^{j\angle Z_{ant}}|W|e^{j0} = |Z_{ant}W|e^{j\angle Z_{ant}}. \tag{C.1}$$

C.1. Inverse Frequency

The first studied function is the inverse frequency

$$W = \frac{1}{f}. \tag{C.2}$$

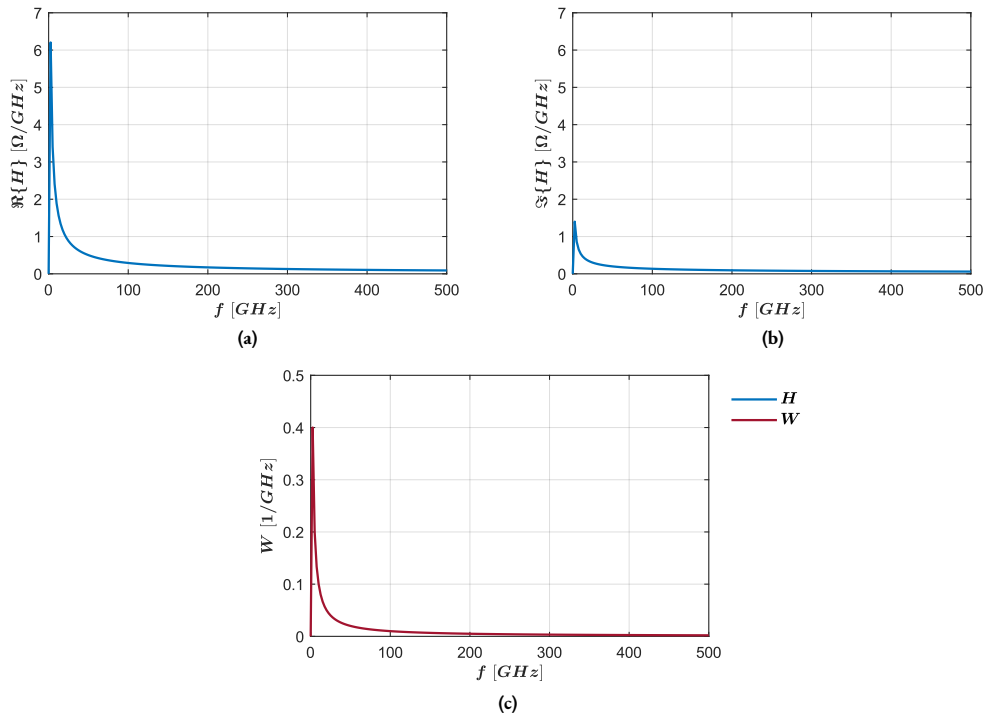


Figure C.1: Frequency-domain of inverse frequency weight and placeholder function; in (a) real part of placeholder function, in (b) imaginary part of placeholder function, and in (c) weight function.

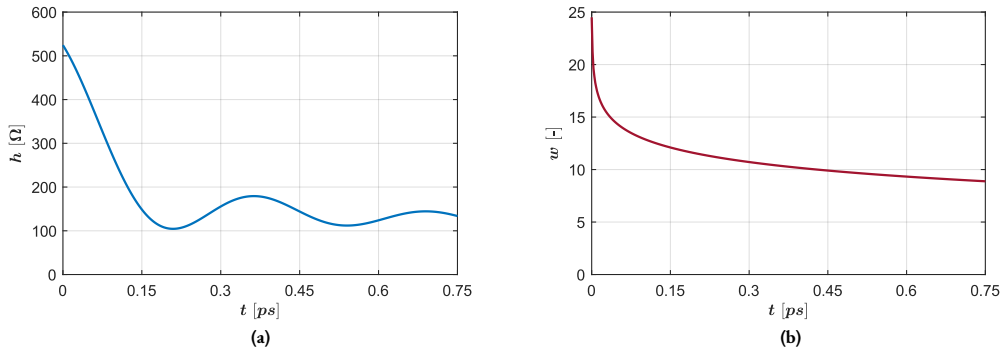


Figure C.2: Time-domain impulse responses (using inverse frequency); in (a) placeholder, in (b) weight.

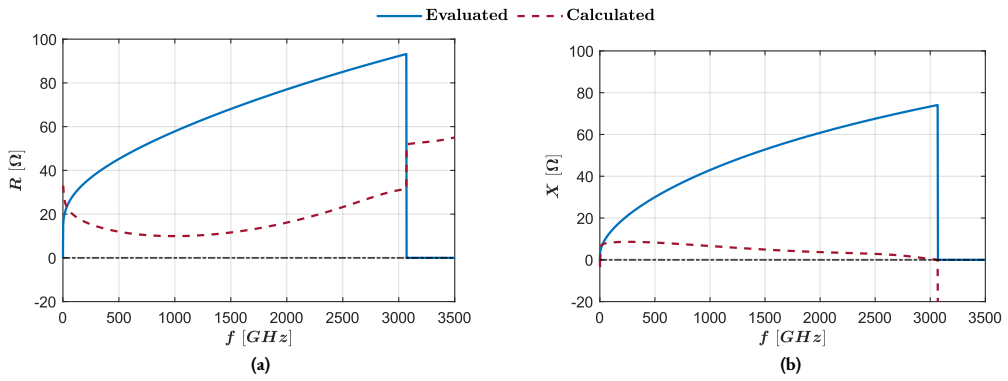


Figure C.3: Impedance comparison (using inverse frequency); in (a) the resistance, in (b) reactance.

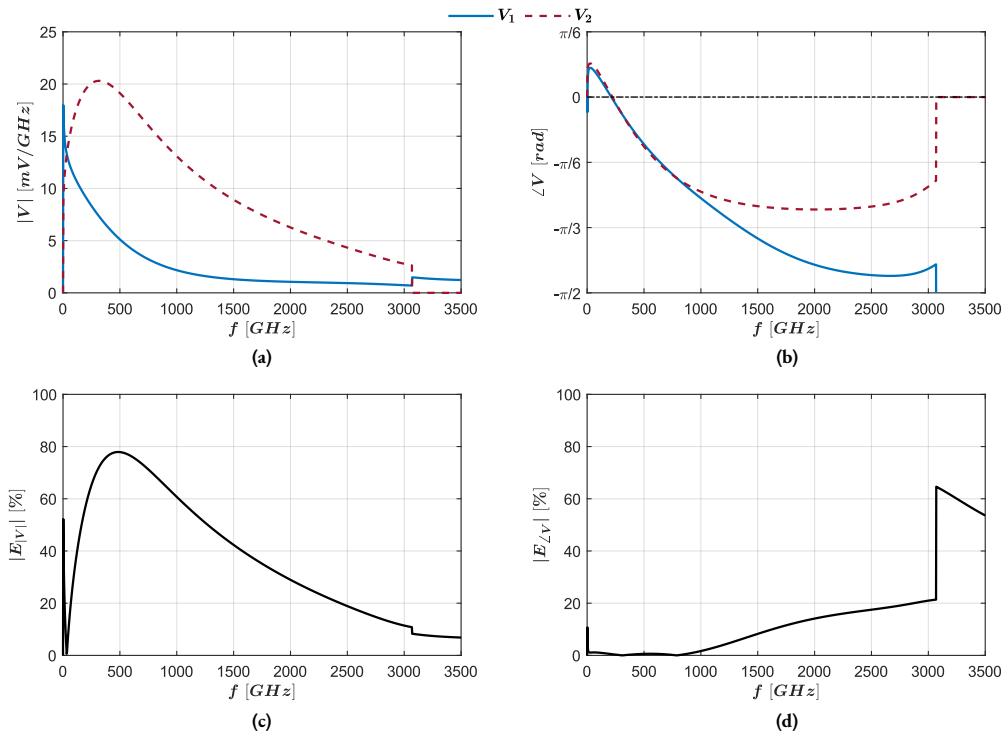


Figure C.4: Voltage error (using inverse frequency); in (a) voltage magnitude comparison, in (b) phase comparison, in (c) the voltage magnitude error, and in (d) phase error.

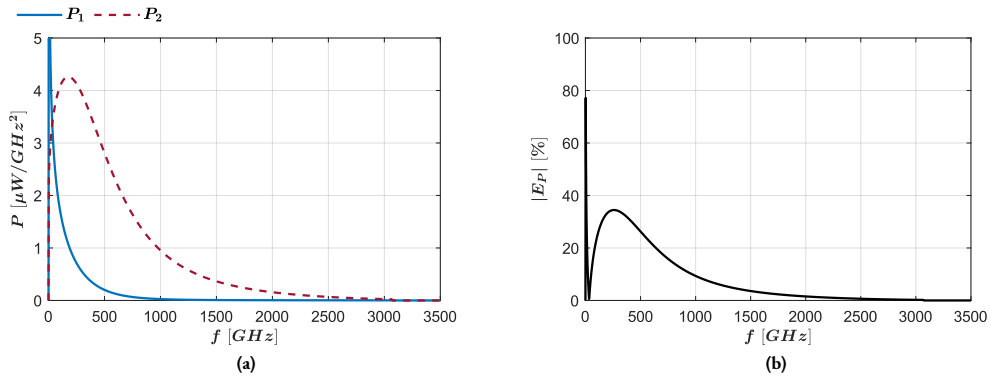


Figure C.5: Power error (using inverse frequency); in (a) active power spectral density comparison, in (b) the error.

C.2. Triangular

The second investigated function is the triangular

$$W = \max\left(1 - \frac{f}{f_{max}}, 0\right), \tag{C.3}$$

with f_{max} equal to the maximum frequency at which the quasi-TEM mode is dominant.

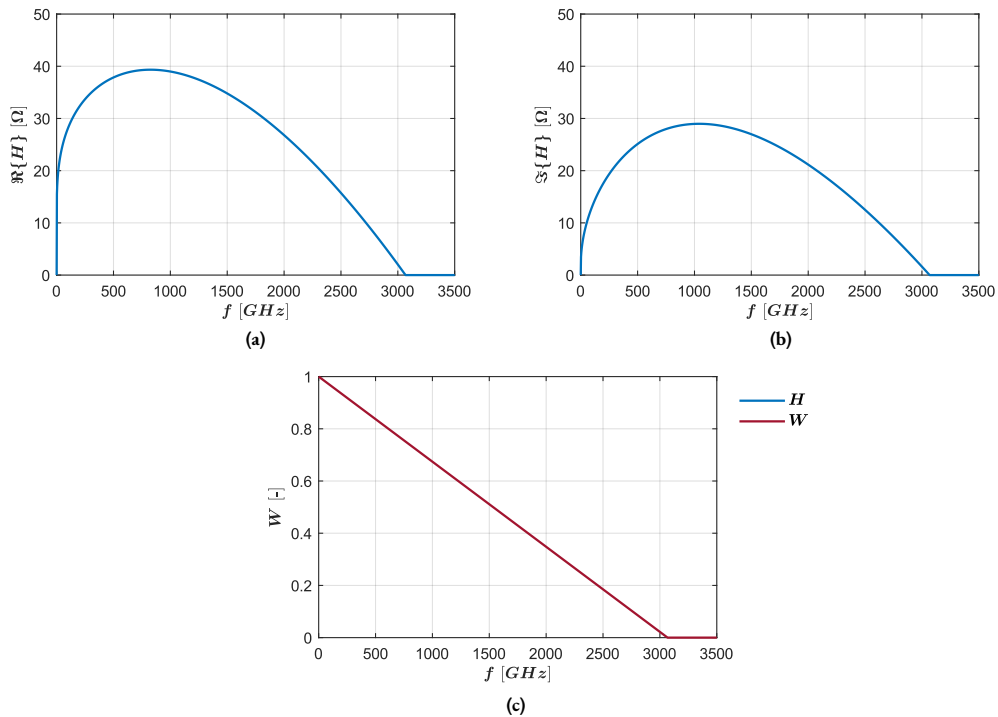


Figure C.6: Frequency-domain of triangular weight and placeholder function; in (a) real part of placeholder function, in (b) imaginary part of placeholder function, and in (c) weight function.

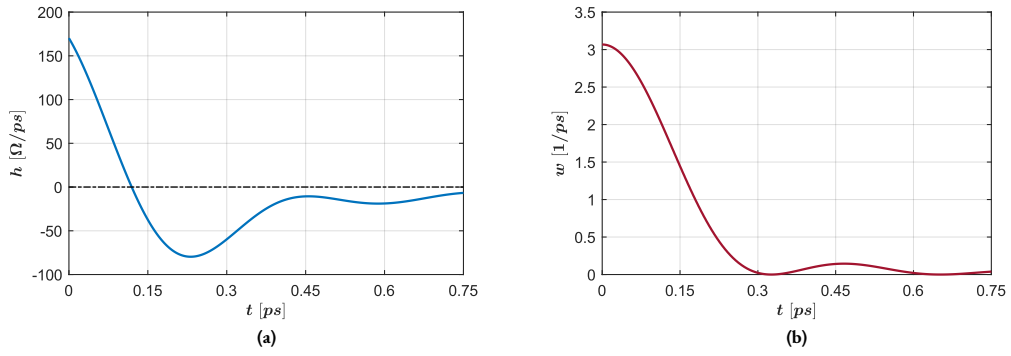


Figure C.7: Time-domain impulse responses (using triangular function); in (a) placeholder, in (b) weight.

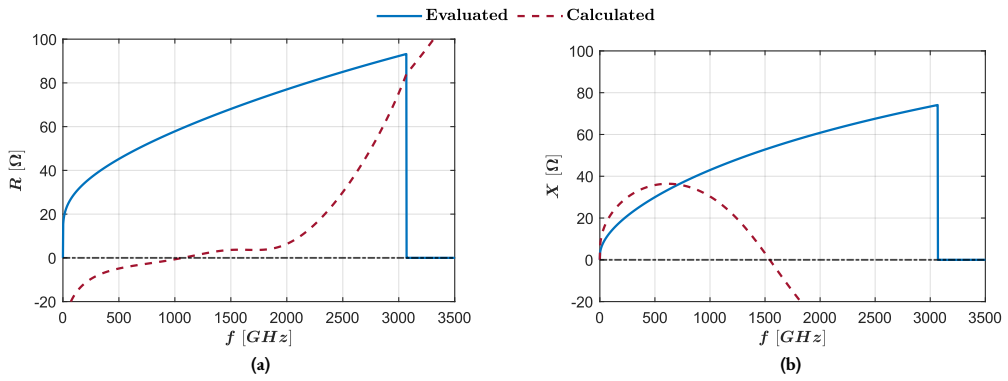


Figure C.8: Impedance comparison (using triangular function); in (a) the resistance, in (b) reactance.

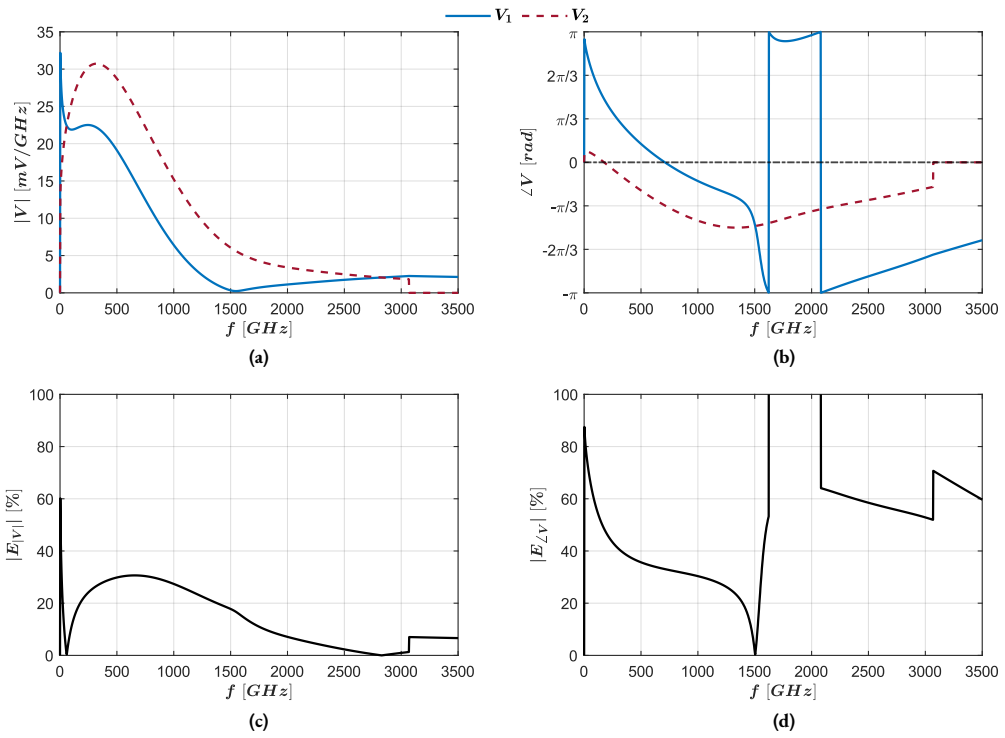


Figure C.9: Voltage error (using triangular function); in (a) voltage magnitude comparison, in (b) phase comparison, in (c) the voltage magnitude error, and in (d) phase error.

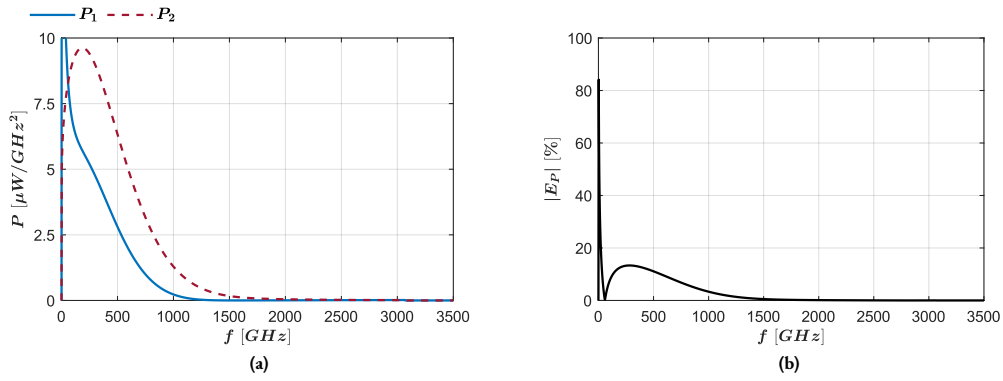


Figure C.ro: Power error (using triangular function); in (a) active power spectral density comparison, in (b) the error.

C.3. Inverse Exponential

Third, inverse exponential is investigated

$$W = e^{-\alpha f}, \tag{C.4}$$

where

$$\alpha = -\frac{\ln 0.01}{f_{max}} \tag{C.5}$$

is chosen such that to multiple the maximum frequency (at which the quasi-TEM mode is dominant) by 0.01.

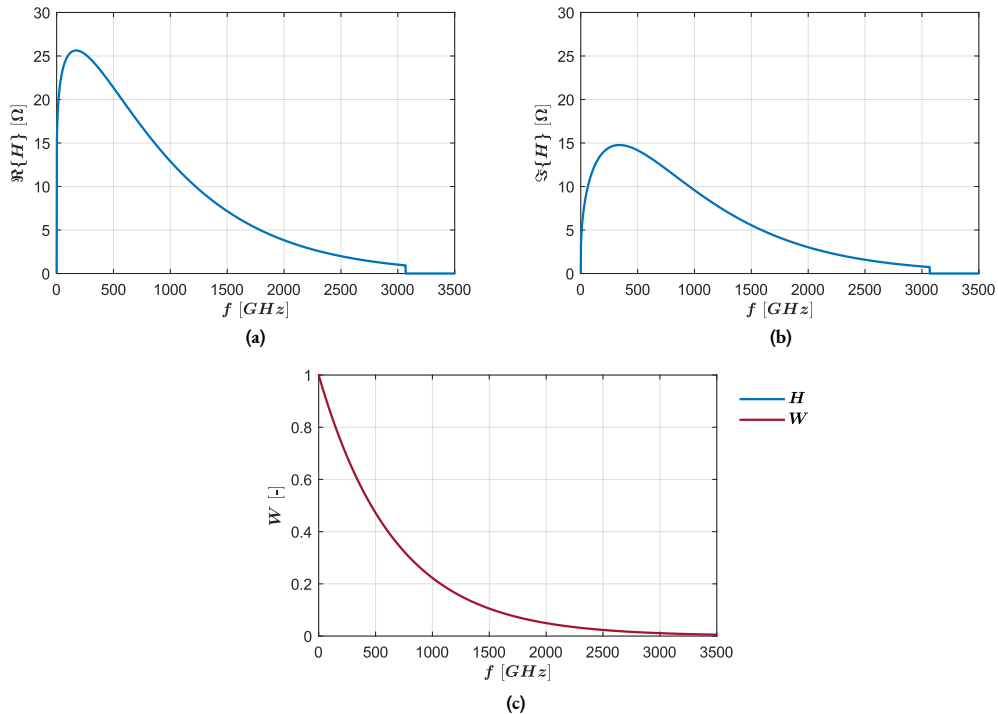


Figure C.ii: Frequency-domain of inverse exponential weight and placeholder function; in (a) real part of placeholder function, in (b) imaginary part of placeholder function, and in (c) weight function.

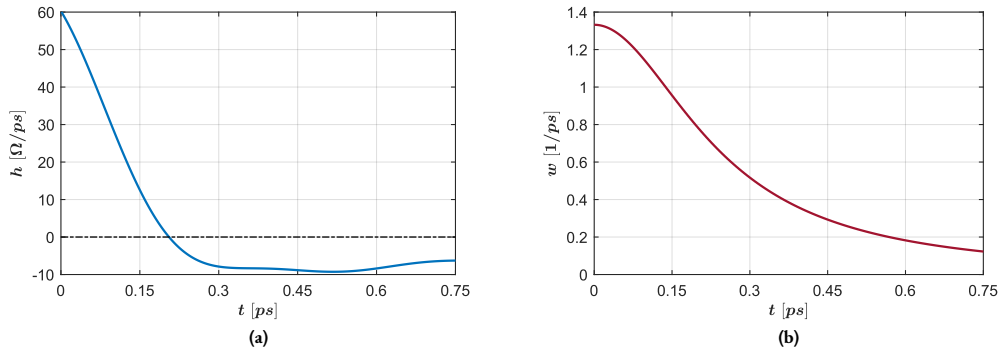


Figure C.12: Time-domain impulse responses (using inverse exponential); in (a) placeholder, in (b) weight.

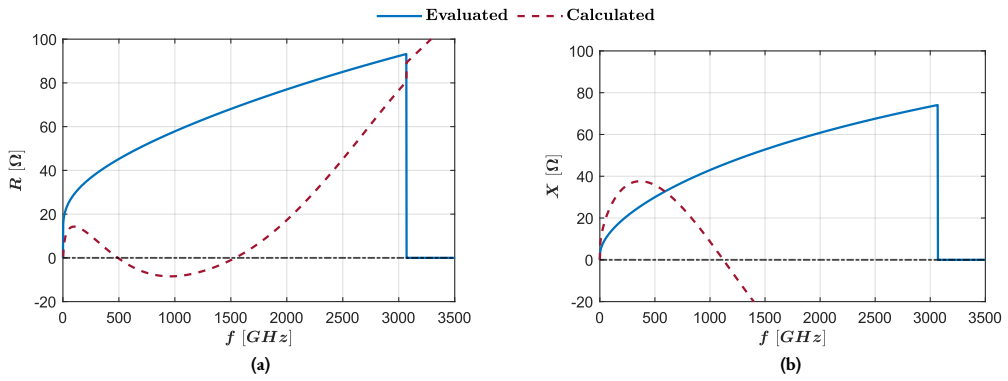


Figure C.13: Impedance comparison (using inverse exponential); in (a) the resistance, in (b) reactance.

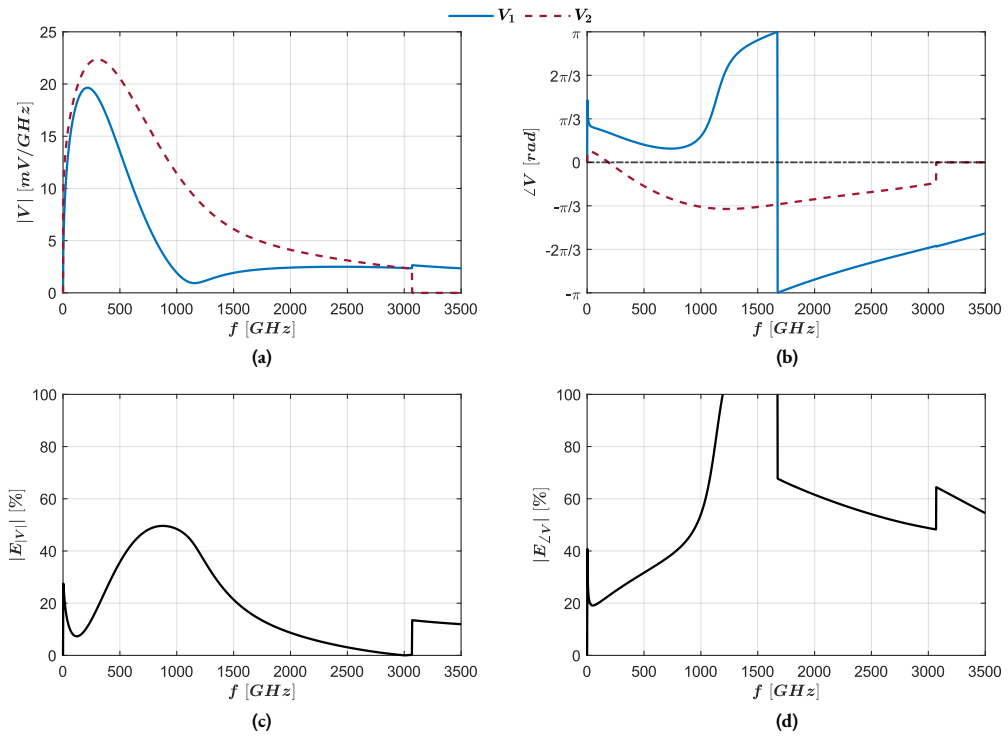


Figure C.14: Voltage error (using inverse exponential); in (a) voltage magnitude comparison, in (b) phase comparison, in (c) the voltage magnitude error, and in (d) phase error.

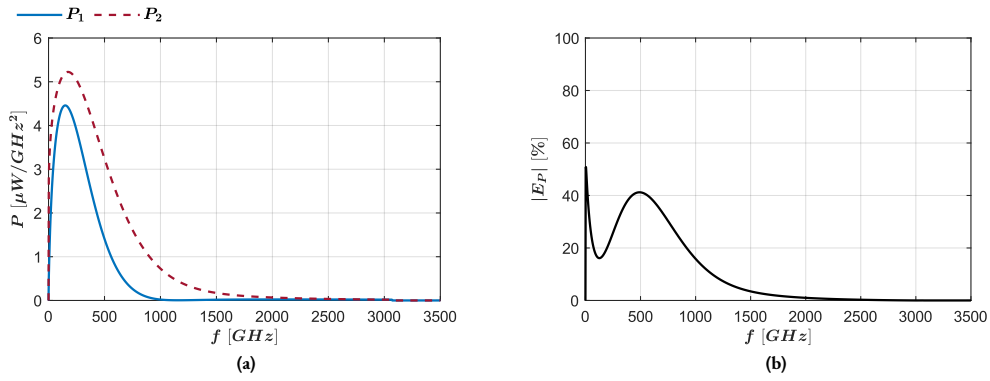


Figure C.15: Power error (using inverse exponential); in (a) active power spectral density comparison, in (b) the error.

C.4. Butterworth Filter Envelope

Finally, the performance of a Butterworth filter envelope is studied inverse exponential is investigated

$$W = \left| \prod_{k=1}^n \frac{1}{jf/f_c - e^{j\pi \frac{2k+n-1}{2n}}} \right|, \tag{C.6}$$

where the cut-off frequency $f_c = 1500 GHz$, and the filter order $n = 5$.

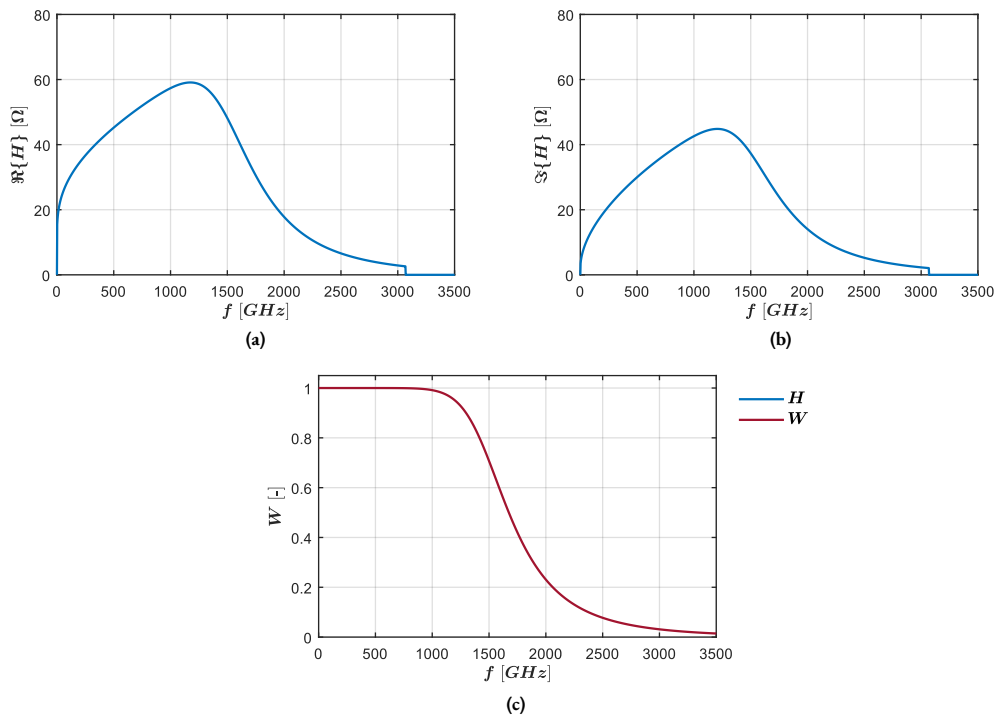


Figure C.16: Frequency-domain of Butterworth filter envelope weight and placeholder function; in (a) real part of placeholder function, in (b) imaginary part of placeholder function, and in (c) weight function.

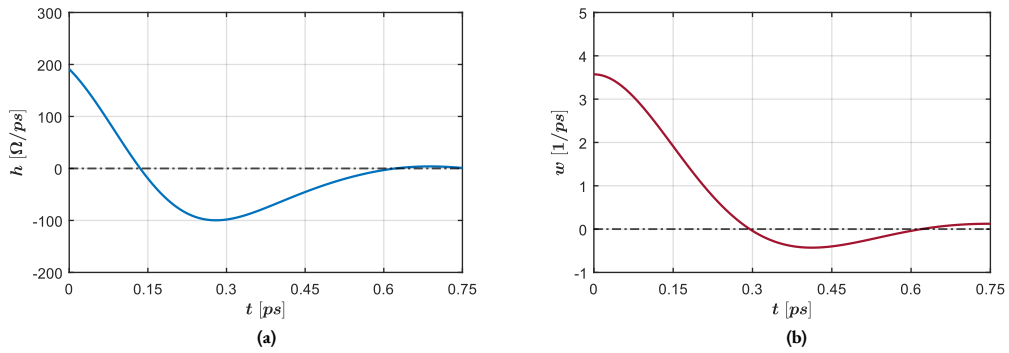


Figure C.17: Time-domain impulse responses (using Butterworth filter envelope); in (a) placeholder, in (b) weight.

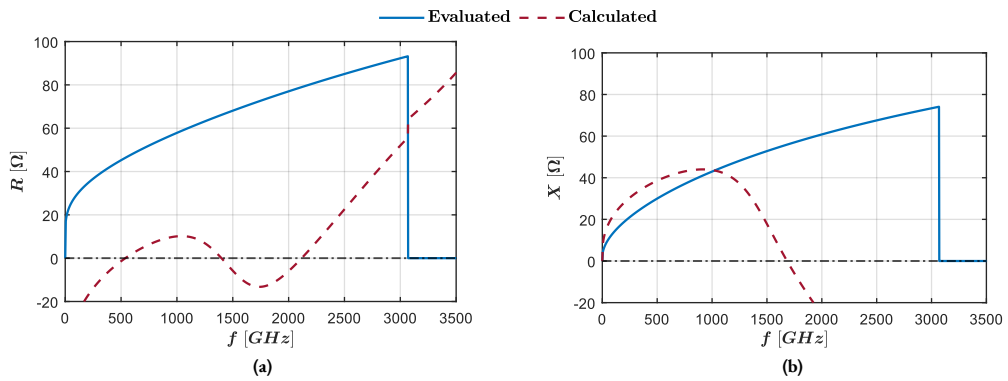


Figure C.18: Impedance comparison (using Butterworth filter envelope); in (a) the resistance, in (b) reactance.

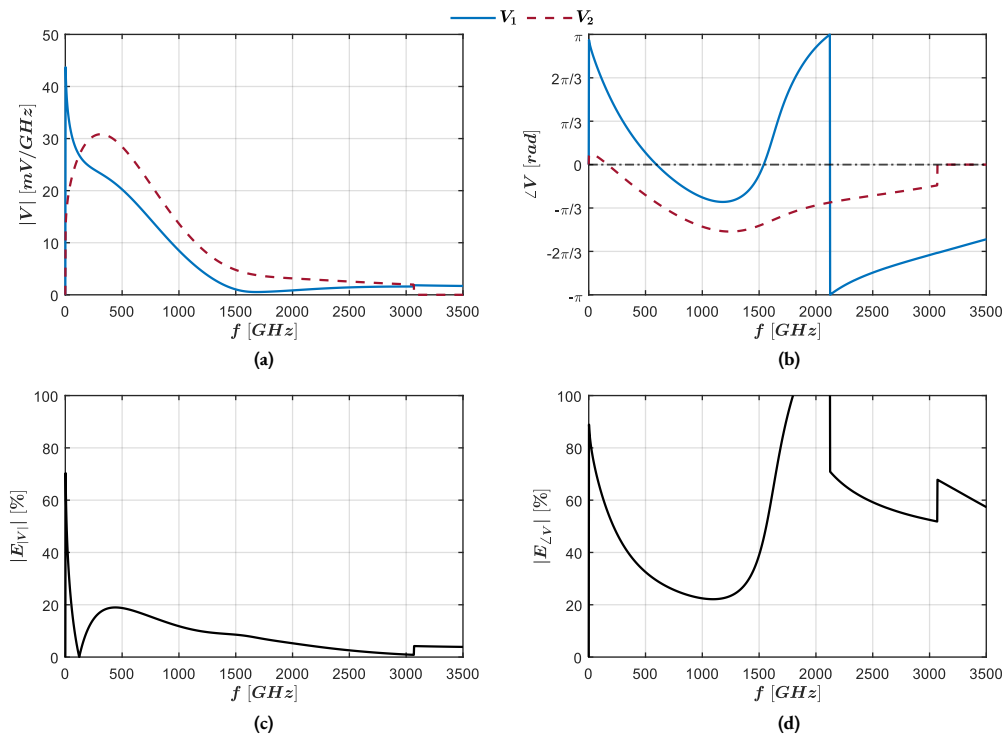


Figure C.19: Voltage error (using Butterworth filter envelope); in (a) voltage magnitude comparison, in (b) phase comparison, in (c) the voltage magnitude error, and in (d) phase error.

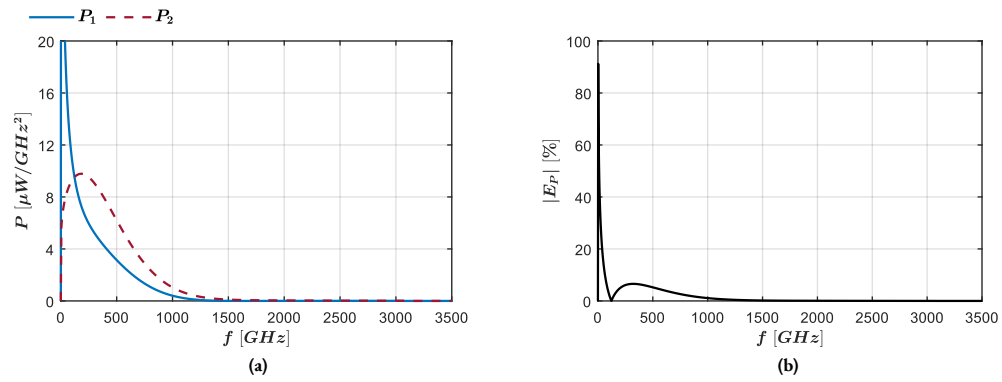


Figure C.20: Power error (using Butterworth filter envelope); in (a) active power spectral density comparison, in (b) the error.

Bibliography

- [1] Y. Peng, C. Shi, X. Wu, Y. Zhu, and S. Zhuang, "Terahertz biomedical application research," in *International Conference on Infrared, Millimeter, and Terahertz Waves, IRMMW-THz*, vol. 2021-August, 2021. DOI: 10.1109/IRMMW-THz50926.2021.9567277.
- [2] M. HANGYO, M. TANI, T. NAGASHIMA, H. KITAHARA, and H. SUMIKURA, "Spectroscopy and imaging by laser excited terahertz waves," *Plasma and Fusion Research*, vol. 2, 2007. DOI: 10.1585/pfr.2.s1020.
- [3] P. U. Jepsen, D. G. Cooke, and M. Koch, "Terahertz spectroscopy and imaging - modern techniques and applications," *Laser and Photonics Reviews*, vol. 5, 1 2011, ISSN: 18638880. DOI: 10.1002/lpor.201000011.
- [4] J. F. Federici, B. Schulkin, F. Huang, *et al.*, *Thz imaging and sensing for security applications - explosives, weapons and drugs*, 2005. DOI: 10.1088/0268-1242/20/7/018.
- [5] M. C. Kemp, P. F. Taday, B. E. Cole, J. A. Cluff, A. J. Fitzgerald, and W. R. Tribe, "Security applications of terahertz technology," in *Terahertz for Military and Security Applications*, vol. 5070, 2003. DOI: 10.1117/12.500491.
- [6] D. Saeedkia, *Handbook of Terahertz Technology for Imaging, Sensing and Communications*. 2013. DOI: 10.1533/9780857096494.
- [7] "Global terahertz technology market size, share & trends analysis report by end use, by type (imaging systems, communication systems, and spectroscopy systems), by application, by regional outlook and forecast, 2023 - 2030," KBV Research, Tech. Rep., Feb. 2024.
- [8] "Terahertz technology market forecasts to 2030 - global analysis by type (terahertz time domain spectroscopy, terahertz frequency domain spectroscopy, terahertz imaging and other types), component, application, end user and by geography," Statistics Market Research Consulting, Tech. Rep., Jan. 2025.
- [9] "Terahertz technology market worth \$3,003.1 million, globally, by 2030 - exclusive report by the insight partners," The Insight Partners, Tech. Rep., Sep. 2024.
- [10] M. Huiskes, "Towards the design of an imaging setup using photoconductive antennas," M.S. thesis, Delft University of Technology, Oct. 2022.
- [11] A. Neto and S. Maci, "Green's function for an infinite slot printed between two homogeneous dielectrics - part i: Magnetic currents," *IEEE Transactions on Antennas and Propagation*, vol. 51, 7 2003, ISSN: 0018926X. DOI: 10.1109/TAP.2003.813625.
- [12] S. Maci and A. Neto, "Green's function of an infinite slot printed between two homogeneous dielectrics - part ii: Uniform asymptotic solution," *IEEE Transactions on Antennas and Propagation*, vol. 52, 3 2004, ISSN: 0018926X. DOI: 10.1109/TAP.2004.825500.
- [13] A. Neto and S. Maci, "Input impedance of slots printed between two dielectric media and fed by a small Δ -gap," *IEEE Antennas and Wireless Propagation Letters*, vol. 3, 1 2004, ISSN: 15361225. DOI: 10.1109/LAWP.2004.829993.
- [14] G. C. Loata, M. D. Thomson, T. Löffler, and H. G. Roskos, "Radiation field screening in photoconductive antennae studied via pulsed terahertz emission spectroscopy," *Applied Physics Letters*, vol. 91, 23 2007, ISSN: 00036951. DOI: 10.1063/1.2823590.

- [15] N. Khiabani, Y. Huang, Y. C. Shen, and S. J. Boyes, "Theoretical modeling of a photoconductive antenna in a terahertz pulsed system," *IEEE Transactions on Antennas and Propagation*, vol. 61, 4 2013, ISSN: 0018926X. DOI: 10.1109/TAP.2013.2239599.
- [16] A. Garufo, "Towards the engineering of pulsed photoconductive antennas," Ph.D. dissertation, Delft University of Technology, 2017. DOI: 10.4233/uuid:3850fd4d-9256-4925-88bb-9679da5f3aaf.
- [17] A. Garufo, G. Carluccio, N. Llombart, and A. Neto, "Norton equivalent circuit for pulsed photoconductive antennas-part i: Theoretical model," *IEEE Transactions on Antennas and Propagation*, vol. 66, 4 2018, ISSN: 0018926X. DOI: 10.1109/TAP.2018.2800524.
- [18] A. Garufo, G. Carluccio, J. R. Freeman, *et al.*, "Norton equivalent circuit for pulsed photoconductive antennas - part ii: Experimental validation," *IEEE Transactions on Antennas and Propagation*, vol. 66, 4 2018, ISSN: 0018926X. DOI: 10.1109/TAP.2018.2800704.
- [19] A. Neto, N. L. Juan, and A. Freni, "Time-domain modelling of pulsed photoconducting sources - part i: The norton equivalent circuit," *IEEE Transactions on Antennas and Propagation*, vol. 71, 3 2023, ISSN: 15582221. DOI: 10.1109/TAP.2022.3184517.
- [20] A. F. Bernardis, P. M. Sberna, J. Bueno, H. Zhang, N. Llombart, and A. Neto, "Time-domain modelling of pulsed photoconducting sources - part ii: Characterization of an It gas bow-tie antenna," *IEEE Transactions on Antennas and Propagation*, vol. 71, 3 2023, ISSN: 15582221. DOI: 10.1109/TAP.2023.3236763.
- [21] L. F. E. Beijnen, "Distributed excitations of pulsed photo-conductive sources: The time domain analysis," M.S. thesis, Delft University of Technology, Nov. 2023.
- [22] M. Stumpf, J. Gu, and I. E. Lager, "Time-domain electromagnetic leaky waves," *IEEE Transactions on Antennas and Propagation*, vol. 71, 4 2023, ISSN: 15582221. DOI: 10.1109/TAP.2023.3249358.
- [23] M. Stumpf, G. Antonini, and I. E. Lager, "Pulsed electromagnetic excitation of a narrow slot between two dielectric halfspaces," *IEEE Transactions on Antennas and Propagation*, vol. 72, 1 2024, ISSN: 15582221. DOI: 10.1109/TAP.2022.3226341.
- [24] A. Garufo, P. M. Sberna, G. Carluccio, *et al.*, "A connected array of coherent photoconductive pulsed sources to generate mw average power in the submillimeter wavelength band," *IEEE Transactions on Terahertz Science and Technology*, vol. 9, 3 2019, ISSN: 2156342X. DOI: 10.1109/TTHZ.2019.2896791.
- [25] J. Bueno, M. Huiskes, H. Zhang, P. M. Sberna, N. Llombart, and A. Neto, "A leaky enhanced photo-conductive connected array for broadband generation of thz power," in *International Conference on Infrared, Millimeter, and Terahertz Waves, IRMMW-THz*, vol. 2022-August, 2022. DOI: 10.1109/IRMMW-THz50927.2022.9895896.
- [26] R. C. Dorf, *Introduction to Electric Circuits*, R. Koreto, Ed. John Wiley * Sons, Inc., 1989, pp. 166–174.
- [27] D. Lončarević, "Spectral analysis of the infinite slot leaky wave antenna & leaky wave antenna with multiple slots," M.S. thesis, Delft University of Technology, Jun. 2022.
- [28] A. Neto and J. J. Lee, "Ultrawide-band properties of long slot arrays," *IEEE Transactions on Antennas and Propagation*, vol. 54, 2 2006, ISSN: 15582221. DOI: 10.1109/TAP.2005.863140.
- [29] D. Cavallo, "Connected array antennas : Analysis and design," Ph.D. dissertation, Technische Universiteit Eindhoven, Nov. 2011. DOI: 10.6100/IR719461.
- [30] D. Cavallo, A. Neto, and G. Gerini, "Analytical description and design of printed dipole arrays for wideband wide-scan applications," *IEEE Transactions on Antennas and Propagation*, vol. 60, 12 2012, ISSN: 0018926X. DOI: 10.1109/TAP.2012.2209856.
- [31] A. B. Smolders, H. J. Visser, and U. Johannsen, *Modern Antennas and Microwave Circuits - A complete master-level course*. Jan. 2022.